



Universiteit
Leiden
The Netherlands

Some assembly required: the structural evolution and mass assembly of galaxies at $z < 5$

Hill, A.

Citation

Hill, A. (2018, April 18). *Some assembly required: the structural evolution and mass assembly of galaxies at $z < 5$* . Retrieved from <https://hdl.handle.net/1887/61630>

Version: Not Applicable (or Unknown)

License: [Licence agreement concerning inclusion of doctoral thesis in the Institutional Repository of the University of Leiden](#)

Downloaded from: <https://hdl.handle.net/1887/61630>

Note: To cite this publication please use the final published version (if applicable).

Cover Page



Universiteit Leiden



The following handle holds various files of this Leiden University dissertation:

<http://hdl.handle.net/1887/61630>

Author: Hill, A.

Title: Some assembly required: the structural evolution and mass assembly of galaxies at $z < 5$

Issue Date: 2018-04-18

SOME ASSEMBLY REQUIRED:
THE STRUCTURAL EVOLUTION AND MASS ASSEMBLY
OF GALAXIES AT $z < 5$

PROEFSCHRIFT

ter verkrijging van
de graad van Doctor aan de Universiteit Leiden,
op gezag van de Rector Magnificus Prof. mr. C. J. J. M. Stolker,
volgens besluit van het College voor Promoties
te verdedigen op woensdag 18 April 2018
klokke 15:00 uur

door
Allison Hill
geboren te Mississauga, Ontario, Canada
in 1989

Promotor: Prof. dr. M. Franx
Co-promotor: Dr. A. Muzzin (York University)

Promotiecommissie

Overige leden: Dr. K. Caputi (Groningen)
Prof. dr. P. van Dokkum (Yale)
Dr. A. van der Wel (Ghent)
Dr. J. Hodge
Prof. dr. J. Schaye
Prof. dr. P. van der Werff
Prof. dr. H. J. A. Röttgering

ISBN 978-94-028-1005-9

Cover designed and created by Mart van der Wiel.

To 11 year old me.
You did it!

“To study and not think is a waste. To think and not study is dangerous.”
-Confucius, *The Analects*

TABLE OF CONTENTS

1	Introduction	1
1.1	The Birth of Extra-Galactic Astronomy	2
1.2	Tracing Galaxy Evolution Using Integrated Properties	2
1.3	Progenitor Selection	4
1.4	The Structural Evolution of Galaxy Progenitors	6
1.5	Galaxy Ages and Assembly Times	6
1.6	This Thesis	8
	References	10
2	The Mass, Color, and Structural Evolution of Today’s Massive Galaxies Since $z \sim 5$	13
2.1	Introduction	14
2.2	Sample Selection	15
2.2.1	Number-density selection	15
2.2.2	The implied stellar mass growth of the progenitors of massive galaxies since $z \sim 5$	16
2.2.3	Data	18
2.3	Rest-Frame Color Evolution	20
2.4	Evolution in Far-Infrared Star Formation Rates	24
2.5	Analysis	25
2.5.1	Stacked Images	25
2.5.2	Sersic Profile Fitting	27
2.5.3	Evolution in r_e	29
2.5.4	Evolution in n	33
2.5.5	Mass Assembly	33
2.5.6	Comparisons with simulations	37
2.6	Discussions and Conclusions	39
2.6.1	Mass and size growth at $z < 2$	39
2.6.2	Mass and size growth at $z > 2$	41
2.7	Summary	42
2.8	Acknowledgments	43

TABLE OF CONTENTS

2.9	Appendix	44
2.9.1	The effects of a fixed cumulative number density selection on the stellar surface mass density profiles	44
	References	45
3	The Mass Growth and Stellar Ages of Galaxies: Observations versus Simulations	49
3.1	Introduction	50
3.2	Analysis	51
3.2.1	Measuring the assembly times	51
3.2.2	Measuring the stellar ages	51
3.2.3	Comparison to Simulations	54
3.3	Discussions and Conclusions	56
3.4	Summary	57
3.5	Acknowledgments	58
	References	58
4	The Evolution of Galaxy Flattening at $z < 4$ in CANDELS	61
4.1	Introduction	62
4.2	Sample Selection	63
4.3	Analysis	65
4.3.1	Correcting for Systematics	65
4.3.2	Trends with star-formation, M_* , z , r_e and n	66
4.3.3	Is n driving trends with q_{med} ?	70
4.4	Discussions and Conclusions	71
4.5	Summary	74
4.6	Acknowledgments	75
	References	75
5	A Stellar Velocity Dispersion for a Strongly-Lensed, Intermediate- Mass Quiescent Galaxy at $z = 2.8$	77
5.1	Introduction	78
5.2	Data	80
5.2.1	COSMOS 0050+4901	80
5.2.2	Rest-Frame UVJ Colors	80
5.2.3	Spectroscopic Data	82
5.2.4	Spectroscopic Reduction	83
5.3	Structural Properties and Stellar Populations	84
5.3.1	Redshift Determination	84
5.3.2	Stellar Population Properties	88
5.3.3	MIPS 24 μm Photometry	91
5.3.4	Stellar Velocity Dispersion	91
5.3.5	Mass Fundamental Plane	96
5.4	Discussion and Conclusions	97
5.5	Acknowledgments	100
	References	100

Nederlandse samenvatting	103
Publications	107
Curriculum Vitae	109
Acknowledgements	111

Chapter 1

INTRODUCTION

Understanding how galaxies grow and evolve is an important question whose relevance spans many sub-fields in astronomy and astrophysics. It is a massive undertaking, encompassing billions of years of time. Observationally one needs to explain how the minuscule initial density perturbations seen in the almost uniform microwave background radiation echoing from the big bang, grow into the complex, and diverse structure of galaxies we see in our own cosmic backyard. This work attempts to explain a little bit of what occurs in-between.

In this thesis, we use number density arguments to connect these galaxies to their low-redshift counterparts, and investigate when and where stellar mass is assembled. We also compare our results to state-of-the-art, cosmological simulations. By identifying in what way these galaxies change over time, we aim to inform the astrophysical processes which underly their evolution.

1.1 The Birth of Extra-Galactic Astronomy

At the time of writing, the field of extra-galactic astronomy is fast approaching its 100th year (or perhaps it has already elapsed - as with all things, it depends on how you count). Prior to the early 20th century, whether or not the stars, gas and dust that made up our Milky Way galaxy was the extent of our universe was an issue of considerable debate.

For over a thousand years, nebulae, or ‘clouds’ had been observed in the night sky. These nebulae turned out to be a diversity of objects including stellar nurseries, stellar remnants, and galaxies, with nebulae referring to an observational class of objects which appeared ‘fuzzy’ on the night sky. Several renowned figures from history including the astronomer William Herschel, and the philosopher Immanuel Kant had subscribed to the idea that some of these nebulae were not small clouds that were members of our ‘universe’, but instead were huge *island universes* existing outside our own.

However their extra-galactic nature remained hotly debated until Edwin Hubble surveyed variable Cepheid stars in two of these nebulae documented in the Messier catalogue, M31 and M33 (Hubble 1925). Using the tight period-luminosity relation known to this class of stars, he was able to prove conclusively that these ‘nebulae’ were much too distant to be a tiny component of our own galaxy, and instead were a massive arrangement of stars and gas, and galaxies in their own right. It was a paradigm shift on the scale of when Tycho Brahe’s observations of planetary motion confirmed the Copernican heliocentric model - the observable universe had just become a lot bigger, and our proximity to the centre of it was once again displaced.

Since Hubble’s first foray beyond the confines of our Galaxy, our understanding of the physical scale of the universe continues to expand; an expansion which is both literal, and figurative in nature. In 1929, Hubble noted a linear relationship between a galaxy’s distance to us and its recession speed, implying that the universe was getting bigger (Hubble 1929). The idea that the universe was expanding set the stage for a radical new view of cosmology, one in which our universe had a beginning from which to expand from. This cosmology invariably leads to a universe in which galaxies grow and evolve, which is a central tenant to the study of extra-galactic astronomy.

1.2 Tracing Galaxy Evolution Using Integrated Properties

In science, the best way to understand a physical, chemical, or biological process is to conduct an experiment in an environment where variables can be strictly controlled or accounted for to ferret out cause and effect. Results from experiment are noted, and used to develop and test theory. This is the heart of the scientific method. In astronomy and astrophysics, this is largely untenable. Astronomy is an observational science, with the time and physical scales involved practically infinite compared to the life-time and physical experience of the astronomer.

Fortunately, the invariability of the speed of light allows astronomers to effectively look back in time by observing galaxies at greater and greater distances. Although we cannot observe the billion year evolution of a single galaxy in even a thousand human lifetimes, we can look at how properties of galaxies change at different redshifts and infer evolution. The most famous example of this method is the measurement of the integrated star formation rate (SFR) of all galaxies at different epochs (Fig. 1.1). From Fig. 1.1, we are able to infer that galaxies were forming stars at a much higher rate than at the present day, and that this rate peaked ~ 10 billion years ago.

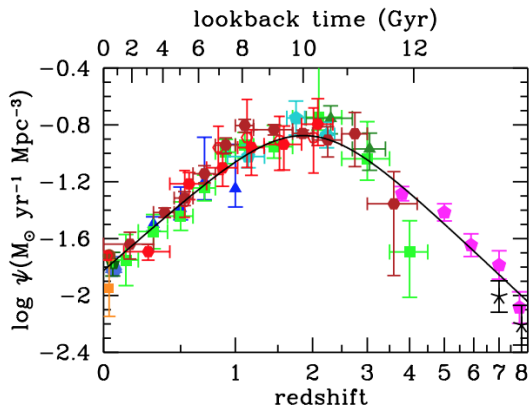


Figure 1.1 The cosmic star-formation rate density across cosmic time from Madau & Dickinson (2014). Here we see the peak of cosmic star formation occurred at $z \sim 2$, or ~ 10 Gyr ago. This tells us that galaxies were forming stars at a higher rate in the past and this has been on a steady decline continuing through the present day.

Although the cosmic star formation history is informative, it is an integrated property across all galaxies. It does not specify where star formation is concentrated, in which galaxies most of the stellar mass is assembled, how the structure or morphology of galaxies change, the merger rates of galaxies, or whether these properties depend on stellar mass, dark-matter halo mass, gas fractions or any number of dependencies which might better explain the physics of what is driving evolution.

One way to achieve more specificity is to measure how the galaxy census evolves with redshift. In extra-galactic astronomy, the galaxy stellar mass function (GSMF) provides the relative abundance of galaxies as a function of mass in the form of number densities (e.g., Moustakas et al. 2013; Ilbert et al. 2013; Muzzin et al. 2013b). By measuring the GSMF at different redshifts, the changes in relative abundances can be determined (Fig. 1.2).

The evolution in the GSMF from Fig. 1.2 already reveals some interesting trends. It appears that the number density of the most massive galaxies ($\sim 10^{12}M_{\odot}$)

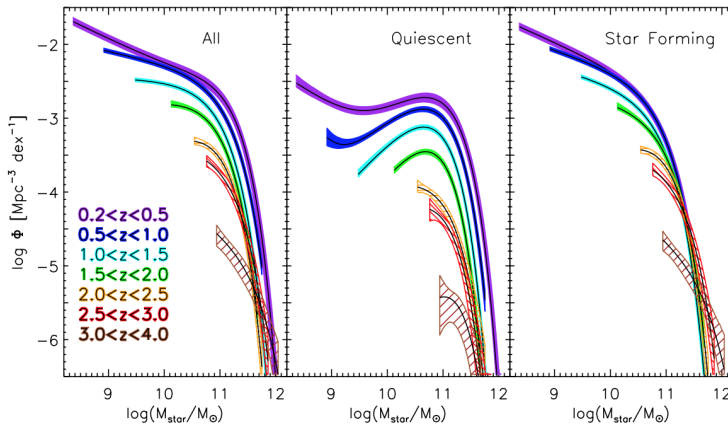


Figure 1.2 The evolution of the total (left), quiescent (centre) and star-forming (right) galaxy stellar mass functions from Muzzin et al. (2013b).

does not change significantly with redshift, suggesting these galaxies form at relatively early times. Muzzin et al. (2013b) also separated the GSMF based on galaxies which are quiescent (i.e. not actively forming stars or are forming them at insignificant rates), and those that are actively star-forming. We see the corollary in the center and right panels of Fig. 1.2 - there is a decrease in the number density of the most massive star-forming galaxies, with a corresponding increase in the number density of the most massive quiescent galaxies. This suggests that the most massive galaxies were actively forming stars at high redshift, and have since quenched.

Together, the conclusions drawn from Fig. 1.1 and Fig. 1.2 are significant, and already reveal salient truths about how galaxies evolve. However, the questions posed earlier still remain unanswered. The GSMF obfuscates much of the specific evolution and does not explain the underlying processes that drive evolution. For instance - why do the most massive galaxies quench at high redshifts? Do they exhaust their gas reservoirs? Does feedback play a role? Is the feedback driven by star-formation, or from quasars? In order to answer these questions, it is necessary to develop a method to connect progenitors to descendants.

1.3 Progenitor Selection

The most straight-forward way to look at galaxy evolution as a function of stellar mass is to choose a fixed stellar mass, and see how galaxy properties change as a function of redshift (we have already implicitly done this with the example of the evolution in the GSMF from Fig. 1.2 and the discussion in Sec. 1.2 when we examined the change in number density of galaxies with a stellar mass of $\sim 10^{12}M_{\odot}$). This method is useful in determining what galaxies at a fixed mass looked like in the past, however it does not show how any one particular class of

galaxy evolves.

If we were to infer an evolutionary link from fixed-mass analysis, we have implicitly assumed that in almost 10 billion years of cosmic time galaxies do not merge, and that they form no new stars. From Fig. 1.1 we already know that the assumption that galaxies do not form new stars is an unreasonable one, and it has been shown that galaxies do in fact merge, necessitating alternative methods to connect progenitor to descendant.

There are many methods which have been used to select progenitors and draw direct evolutionary connections in the literature; via fixed central velocity dispersion (e.g., Bezanson et al. 2012), the evolution of the SFR-stellar mass relation (e.g., Patel et al. 2013b), fixed central surface-mass density (e.g., van Dokkum et al. 2014; Williams et al. 2014) and more generally, number density arguments (e.g., Brammer et al. 2011; Papovich et al. 2011; van Dokkum et al. 2010, 2013; Muzzin et al. 2013a; Patel et al. 2013a; Marchesini et al. 2014; Ownsworth et al. 2014; Morishita et al. 2015). The required assumptions in some of the aforementioned methods are only applicable in specific regimes (i.e., massive elliptical galaxies, or field galaxies that have undergone no major merging). Since we wish to apply the method more generally, in this thesis we focus on number density selection arguments to choose progenitors.

The first example of using number density arguments to select progenitors was by van Dokkum et al. (2010), who used a constant number density to select the progenitors of today's massive ($\sim 10^{11.5} M_{\odot}$) galaxies out to $z = 2$. By using a constant number density, van Dokkum et al. (2010) assumed that galaxies maintain rank order across cosmic time, that is, the most massive galaxy at $z = 2$ is still the most massive galaxy at $z = 0$. This assumes that the two methods of mass growth, star formation, and merging, do not affect the number density across cosmic time. Mergers will certainly effect the number density, and the only way star formation will keep galaxies at the same rank order is if the specific star formation rate is independent of mass (which is not the case; Schreiber et al. 2015). One would expect the regime of validity of these assumptions to break down at flatter regions in the mass function (i.e., lower mass) as well as comparisons across large redshift ranges, where the errors associated with scatter in the mass accretion histories will begin to add up.

To account for the scatter in mass accretion histories, Behroozi et al. (2013) used abundance matching between galaxies and dark matter halos in simulations to convert *dark-matter* halo merger trees into *galaxy* merger trees. This correction allows one trace the *median* stellar mass evolution across cosmic time with the errors dominated primarily by the uncertainties in the observed stellar mass functions. This method has been shown in simulations to recover the median stellar mass evolution quite well, although it is unable to capture the diversity in galaxy progenitors of a given mass (Torrey et al. 2015; Clauwens et al. 2016; Wellons & Torrey 2017). As such, it is a statistical approach that is best suited for populations of galaxies, and is ideally suited for large surveys.

1.4 The Structural Evolution of Galaxy Progenitors

Using a constant number density selection, van Dokkum et al. (2010) investigated the structural and stellar mass evolution of the progenitors of today’s massive galaxies ($10^{11.4}$) out to $z = 2$. The authors traced the stellar-mass growth as well as the structural evolution using stacking analysis from galaxies in the NEW-FIRM survey, a NIR medium band survey designed to obtain accurate photometric redshifts from the rest-frame optical SED. From these stacks, surface brightness profiles were converted into surface mass density profiles to trace where mass was being accreted as a function of redshift. The most profound finding of this work was that the central regions in massive galaxies have undergone no appreciable mass evolution since $z = 2$, and all mass added has been in the outskirts, consistent with findings by other observationally driven studies (Hopkins et al. 2009; Bezanson et al. 2009). By comparing star-formation rates to the mass profile evolution, they conclude that star-formation was insufficient to explain the mass growth, and that minor mergers are the best candidate to explain the lack of self-similar growth between the interior regions and the outskirts; a viewpoint affirmed in subsequent studies (e.g., Hopkins et al. 2010; Trujillo et al. 2011; Newman et al. 2012; McLure et al. 2013; Hilz et al. 2013; Patel et al. 2013a). Sersic fits to the progenitor surface mass density profiles also show that the effective radius, and sersic index both decrease with increasing redshift, with a corresponding increase in the star-formation rate suggesting star-forming (and potentially disk) progenitors.

Using the abundance matching technique of Behroozi et al. (2013), Marchesini et al. (2014) re-visited the progenitors of massive galaxies. With a new selection, as well as the first data release of the deep, and wide (compared to surveys targeting similar redshift ranges, i.e. CANDELS) NIR UltraVISTA survey, Marchesini et al. (2014) targeted the more massive, and rarer ultra-massive galaxies ($M_* \sim 10^{11.8}$). In addition to the corrected cumulative number density selection, the authors also used a constant cumulative number density selection as a comparison between the two techniques. As expected, the mass evolution for an abundance matched number density selection is steeper than a constant cumulative number density. This means the progenitors are less massive than would have been selected in previous works, with the mass differences greater than the uncertainties in the mass functions at $z > 2$.

1.5 Galaxy Ages and Assembly Times

Arguably the most important ramification of the steeper mass evolution with redshift found using abundance matching (as opposed to a constant cumulative number density as discussed in the previous sections) is the effect this has on galaxy assembly times. If the progenitors at a given redshift are less massive than originally thought, this implies that massive galaxies assemble their mass more quickly at later times. This results in a different ages of assembly for massive galaxies.

Knowing when galaxies assemble their mass is necessary to fully understand

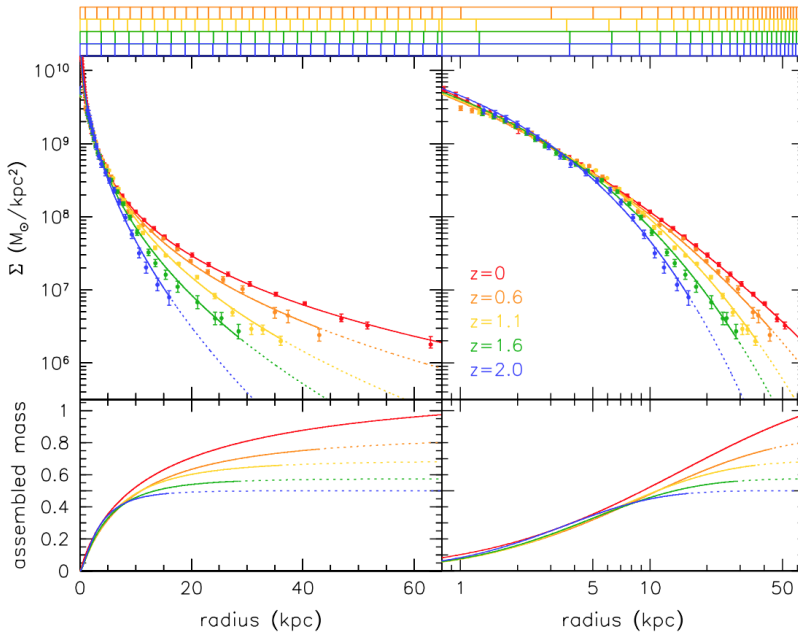


Figure 1.3 The stellar surface mass density profiles from van Dokkum et al. (2010) in linear (left) and log (right) units at redshifts spanning $0 < z < 2$. From this figure, it is evident that massive galaxies grow more substantially at larger radii since $z = 2$.

the mechanisms involved in galaxy growth and evolution. Equipped with a reliable progenitor selection, the assembly time scales of galaxies can be gleaned by simple inference from the stellar mass evolution over time. Although constant cumulative number density over-predicts the assembly age, a comparison of the stellar mass evolution of a diverse mass range of descendants in Muzzin et al. (2013b) implies that massive galaxies have an earlier mass assembly than less massive galaxies (Fig. 1.4), and less massive galaxies have more rapid recent assembly.

This notion of more massive galaxies assembling first is also verified in the galaxy ages. If we assume that galaxies only grow in mass through star formation (a poor assumption), then their assembly times will be equivalent to the measured ages of the stars within a particular galaxy, as the assembly time is simply the time at which the stars came into existence. Using optical spectroscopy, the ages of the galaxies can be measured through age sensitive spectral indices. This has been done extensively for local galaxies (e.g., Kauffmann et al. 2003; Gallazzi et al. 2005; Thomas et al. 2010), with the consensus that massive galaxies are host to older stellar populations than less massive galaxies, and that massive galaxies were the first to form (an idea consistent with what is seen in the mass functions discussed above).

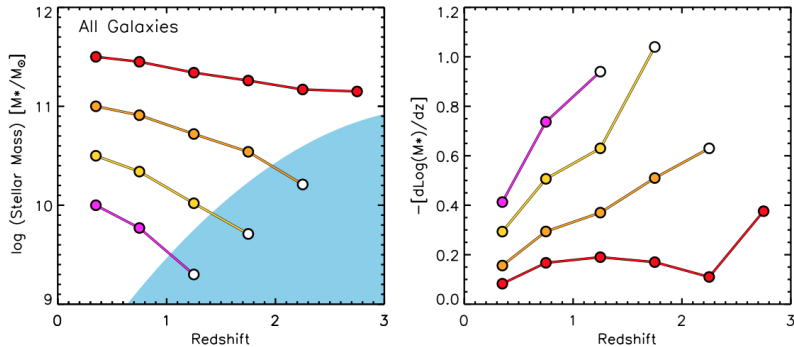


Figure 1.4 Left: the average stellar mass evolution of galaxies with progenitors chosen at a constant cumulative number density which shows that massive galaxies assembled the bulk of their stellar mass at earlier times than less massive galaxies. Right: the derivative of the stellar mass evolution from the left hand plot as a function of redshift. Here we see that less massive galaxies show more rapid recent assembly. (Fig. 14 from Muzzin et al. (2013b))

1.6 This Thesis

As much work as has been done, there remain some open questions which this thesis addresses. van Dokkum et al. (2010) found that the surface mass density profiles of massive galaxies remain essentially unchanged since $z = 2$, which begs the question, when do the interiors assemble, and what do the progenitors of massive galaxies look like at $z > 2$? Does the potential bias towards more massive progenitors in a fixed cumulative number density selection affect the median evolution in previous works? Does this bias also effect the inferred assembly times from Muzzin et al. (2013b)? We address these issues in Chapters 2 and 3.

The focus on the progenitors of $z = 0$ massive galaxies in the literature is partly out of accessibility. Massive galaxies are host to the oldest stars, and also tend to be more luminous making them ideal candidates to trace out to higher redshifts. They are also large, and can be resolved to within $1 r_e$ at higher- z than lower mass galaxies. As such there is currently a dearth of information regarding the evolution of galaxies with $M_* < 10^{11}$ at high- z $z > 2$. We attempt to bridge this divide in Chapters 3, 4 and 5.

Chapter 2

In this chapter, we used number density arguments to select the progenitors of today's massive galaxies in order to map their structural evolution out to $z = 5$. This work builds on the previous seminal work of van Dokkum et al. (2010) with an improved progenitor selection method, as well as the advantage of state-of-the-art NIR surveys which allow us to track progenitors out to higher redshift. We find the median progenitor stellar mass evolution to be steeper with redshift than selection using a fixed cumulative number density, however at $z < 2$, the stellar

masses are consistent within the uncertainties in the mass function. In accordance with previous trends, we find that the progenitors of massive galaxies have smaller effective radii, as well as smaller sersic indices. In contrast to previous findings, our progenitor selection shows stellar mass continues to be accreted at all radii at $z < 2$, although the build-up is more significant at larger radii. At $z > 4$, we see evidence of significant mass growth in the central regions, probing an era of significant mass growth. We also compare our findings to the EAGLE simulation and find similar assembly at small radii. This work appeared in Hill et al. (2017)

Chapter 3

We use the same progenitor selection and mass functions of the previous chapter to measure the main progenitor stellar mass growth of galaxies as a function of stellar mass at $z \sim 0.1$, and measured the assembly time, which we defined as the time at which half the total mass of the descendent was assembled. We compare this assembly time to the light-weighted stellar ages from a sample of low-redshift SDSS galaxies from the literature. Our findings suggest that massive galaxies form a higher proportion of their mass ex-situ than lower-mass galaxies. We compare our timescales to the EAGLE simulation, as well as the semi-analytic models of Henriques et al. (2015). We find the semi-analytic models perform better than EAGLE in reproducing the observed stellar mass versus assembly time and light-weighted stellar ages. This work appeared in Hill et al. (2017b).

Chapter 4

In this chapter, we investigate the median flattening through the axis ratio of galaxies at $z < 0.5$ in the CANDELS fields, and its relationship to parameters such as stellar mass, sersic index, and size. We find that at $z < 2$, quiescent galaxies are rounder than their star-forming counterparts, however at $z > 2$ the median apparent axis ratios are indistinguishable, suggesting the structure in star-forming and quiescent galaxies at high redshift are similar. We also find that in star-forming galaxies, at $z < 1$, the median axis ratio depends strongly on stellar mass, whereas quiescent galaxies do not show the same dependence. The strongest observable dependence for quiescent galaxies is sersic index. For star-forming galaxies, the size is the best predictor for flattening, with larger star-forming galaxies exhibiting smaller axis ratios. From our findings, we believe that the axis ratio is tracing the bulge-to-total galaxy mass ratio which would explain why smaller/more massive star-forming galaxies are rounder than their extended/less massive analogues, as well as why we do not observe strong mass and size dependencies in quiescent galaxies, as the majority of the quiescent population is not expected to have a strong disk complement. This work is to be submitted.

Chapter 5

In this chapter, we measure the stellar velocity dispersion for a strongly lensed, intermediate mass ($10^{5.9} M_{\odot}$) quiescent galaxy at $z = 2.8$. Because it is gravitationally lensed, we were able to obtain the equivalent of ~ 200 hr of exposure time from only 9.8 hr on source, providing a first detailed look at red galaxies of this mass at $z \sim 3$. This object had been found serendipitously in the UltraVISTA sur-

vey, with a measured photometric redshift of $z = 2.4$ (Muzzin et al. 2012). From the discrepancy in the spectroscopic and photometric redshifts, we highlight the importance of spectroscopy for redshift determination for red objects with prominent rest-frame optical breaks. From the spectrum, we measure a stellar velocity dispersion and are able to determine a dynamical mass which is a more direct method and avoids the pitfalls of estimating mass than through the SED, with the associated uncertainties in the initial mass function and effects of dust. We are also able to confirm quiescence through strong Balmer absorption and the absence of any emission lines, as well as establish that intermediate mass galaxies do quench at these redshifts. This work appeared in Hill et al. (2016).

References

- Behroozi, P. S., Marchesini, D., Wechsler, R. H., et al. 2013, *ApJL*, 777, L10
- Bezanson, R., van Dokkum, P., & Franx, M. 2012, *ApJ*, 760, 62
- Bezanson, R., van Dokkum, P. G., Tal, T., et al. 2009, *ApJ*, 697, 1290
- Brammer, G. B., Whitaker, K. E., van Dokkum, P. G., et al. 2011, *ApJ*, 739, 24
- Clauwens, B., Franx, M., & Schaye, J. 2016, *MNRAS*, 463, L1
- Henriques, B. M. B., White, S. D. M., Thomas, P. A., et al. 2015, *MNRAS*, 451, 2663
- Hill, A. R., Muzzin, A., Franx, M., & Marchesini, D. 2017b, *ApJL*, 849, L26
- Hill, A. R., Muzzin, A., Franx, M., et al. 2017a, *ApJ*, 837, 147
- Hill, A. R., Muzzin, A., Franx, M., & van de Sande, J. 2016, *ApJ*, 819, 74
- Hilz, M., Naab, T., & Ostriker, J. P. 2013, *MNRAS*, 429, 2924
- Hopkins, P. F., Bundy, K., Hernquist, L., Wuyts, S., & Cox, T. J. 2010, *MNRAS*, 401, 1099
- Hopkins, P. F., Cox, T. J., Younger, J. D., & Hernquist, L. 2009, *ApJ*, 691, 1168
- Hubble, E. P. 1925, *Popular Astronomy*, 33
- Hubble, E. P. 1929, *Proceedings of the National Academy of Science*, 15, 168
- Ilbert, O., McCracken, H. J., Le Fèvre, O., et al. 2013, *A&A*, 556, A55
- Madau, P., & Dickinson, M. 2014, *ARA&A*, 52, 415
- Marchesini, D., Muzzin, A., Stefanon, M., et al. 2014, *ApJ*, 794, 65
- McLure, R. J., Pearce, H. J., Dunlop, J. S., et al. 2013, *MNRAS*, 428, 1088
- Morishita, T., Ichikawa, T., Noguchi, M., et al. 2015, *ApJ*, 805, 34
- Moustakas, J., Coil, A. L., Aird, J., et al. 2013, *ApJ*, 767, 50
- Muzzin, A., Labbé, I., Franx, M., et al. 2012, *ApJ*, 761, 142
- Muzzin, A., Marchesini, D., Stefanon, M., et al. 2013a, *ApJS*, 206, 8
- . 2013b, *ApJ*, 777, 18
- Newman, A. B., Ellis, R. S., Bundy, K., & Treu, T. 2012, *ApJ*, 746, 162
- Owensworth, J. R., Conselice, C. J., Mortlock, A., et al. 2014, *MNRAS*, 445, 2198
- Papovich, C., Finkelstein, S. L., Ferguson, H. C., Lotz, J. M., & Giavalisco, M. 2011, *MNRAS*, 412, 1123
- Patel, S. G., van Dokkum, P. G., Franx, M., et al. 2013a, *ApJ*, 766, 15
- Patel, S. G., Fumagalli, M., Franx, M., et al. 2013b, *ApJ*, 778, 115

- Schreiber, C., Pannella, M., Elbaz, D., et al. 2015, *A&A*, 575, A74
Torrey, P., Wellons, S., Machado, F., et al. 2015, *MNRAS*, 454, 2770
Trujillo, I., Ferreras, I., & de La Rosa, I. G. 2011, *MNRAS*, 415, 3903
van Dokkum, P. G., Whitaker, K. E., Brammer, G., et al. 2010, *ApJ*, 709, 1018
van Dokkum, P. G., Leja, J., Nelson, E. J., et al. 2013, *ApJL*, 771, L35
van Dokkum, P. G., Bezanson, R., van der Wel, A., et al. 2014, *ApJ*, 791, 45
Williams, C. C., Giavalisco, M., Cassata, P., et al. 2014, *ApJ*, 780, 1
Wellons, S., & Torrey, P. 2017, *MNRAS*, 467, 3887

Chapter 2

THE MASS, COLOR, AND STRUCTURAL EVOLUTION OF TODAY'S MASSIVE GALAXIES SINCE $z \sim 5$

In this paper, we use stacking analysis to trace the mass-growth, colour evolution, and structural evolution of present-day massive galaxies ($\log(M_*/M_\odot) = 11.5$) out to $z = 5$. We utilize the exceptional depth and area of the latest UltraVISTA data release, combined with the depth and unparalleled seeing of CANDELS to gather a large, mass-selected sample of galaxies in the NIR (rest-frame optical to UV). Progenitors of present-day massive galaxies are identified via an evolving cumulative number density selection, which accounts for the effects of merging to correct for the systematic biases introduced using a fixed cumulative number density selection, and find progenitors grow in stellar mass by ≈ 1.5 dex since $z = 5$. Using stacking, we analyze the structural parameters of the progenitors and find that most of the stellar mass content in the central regions was in place by $z \sim 2$, and while galaxies continue to assemble mass at all radii, the outskirts experience the largest fractional increase in stellar mass. However, we find evidence of significant stellar mass build up at $r < 3$ kpc beyond $z > 4$ probing an era of significant mass assembly in the interiors of present day massive galaxies. We also compare mass assembly from progenitors in this study to the EAGLE simulation and find qualitatively similar assembly with z at $r < 3$ kpc. We identify $z \sim 1.5$ as a distinct epoch in the evolution of massive galaxies where progenitors transitioned from growing in mass and size primarily through in-situ star formation in disks to a period of efficient growth in r_e consistent with the minor merger scenario.

Allison R. Hill, Adam Muzzin, Marijn Franx, et al.
The Astrophysical Journal
Volume 837, Issue 2, pp. 147-164 (2017)

2.1 Introduction

The mass growth and structural evolution of today's most massive galaxies is an important tracer of galaxy assembly at early times. These systems are host to the oldest stars, suggesting they were the first galaxies to assemble. Because they are the oldest systems, their progenitors can theoretically be traced to higher redshifts than their low mass counterparts and can be studied from the onset of re-ionization to give a complete history of galactic evolution. Additionally, the most massive systems tend to be the most luminous, and they are the easiest to observe at high redshift with high fidelity. Massive galaxies also provide important constraints on the physics involved in cosmological simulations, as they impose upper limits on growth as well as the efficiency of various feedback mechanisms such as active galactic nuclei, mergers and supernovae.

Today's massive ($\log M_*/M_\odot \sim 11.5$) galaxies, to first order, are a uniform population. They are homogeneous in morphology and star formation, appearing spheroidal and have low specific star formation rates, and high quiescent fractions (e.g., Thomas et al. 2005; Gallazzi et al. 2005; Kuntschner et al. 2010; Thomas et al. 2010; Cappellari et al. 2011; Mortlock et al. 2013; Moustakas et al. 2013; Ilbert et al. 2013; Muzzin et al. 2013b; Davis et al. 2014; McDermid et al. 2015). In contrast to today's massive galaxies, massive galaxies at high redshift show increasing diversity (e.g., Franx et al. 2008; van Dokkum et al. 2011). With increasing redshift, massive galaxies become increasingly star forming (e.g., Papovich et al. 2006; Kriek et al. 2008; van Dokkum et al. 2010; Brammer et al. 2011; Bruce et al. 2012; Ilbert et al. 2013; Muzzin et al. 2013b; Patel et al. 2013a; Stefanon et al. 2013; Barro et al. 2014; Duncan et al. 2014; Marchesini et al. 2014; Toft et al. 2014; van Dokkum et al. 2015; Barro et al. 2016; Man et al. 2016; Tomczak et al. 2016), and the massive galaxies which are identified as quiescent at high redshift are structurally distinct from their low redshift counterparts as seen in their small effective radii (r_e) and more centrally concentrated stellar-mass density profiles (Daddi et al. 2005; Trujillo et al. 2006; Toft et al. 2007; Cimatti et al. 2008; van Dokkum et al. 2008; Damjanov et al. 2009; Newman et al. 2010; Szomoru et al. 2010; Williams et al. 2010; van de Sande et al. 2011; Bruce et al. 2012; Muzzin et al. 2012; Oser et al. 2012; Szomoru et al. 2012, 2013; McLure et al. 2013; van de Sande et al. 2013; Newman et al. 2015; Straatman et al. 2015; Hill et al. 2016).

Although the central regions of massive galaxies contain a higher fraction of the total mass at high redshift, their central stellar densities show remarkably little evolution between $z \approx 2 - 3$ and $z = 0$ (e.g., Bezanson et al. 2009; van Dokkum et al. 2010; Toft et al. 2012; van de Sande et al. 2013; Patel et al. 2013a; Belli et al. 2014a; van Dokkum et al. 2014; Williams et al. 2014; Whitaker et al. 2016) with the majority of stellar-mass build-up occurring in the outer regions (with galaxies growing in an 'inside-out' fashion). This mass assembly is thought to occur via minor, dissipation-less mergers; a scenario which is able to account for the size growth, while leaving the interior regions relatively undisturbed (e.g., Bezanson et al. 2009; Naab et al. 2009; Hopkins et al. 2010; Trujillo et al. 2011; Newman et al. 2012; Hilz et al. 2013; McLure et al. 2013). The aims of the present study are to determine whether these trends continue to high redshifts and to identify

the epoch when galaxies' central regions assemble their mass.

Obtaining a census of massive galaxies across a broad redshift range is technically challenging, as they have low number densities on the sky (Cole et al. 2001; Bell et al. 2003; Conselice et al. 2005; Marchesini et al. 2009; Bezanson et al. 2011; Caputi et al. 2011; Baldry et al. 2012; Ilbert et al. 2013; Muzzin et al. 2013b; Duncan et al. 2014; Tomczak et al. 2014; Caputi et al. 2015; Stefanon et al. 2015; Huertas-Company et al. 2016) and their rest-frame optical emission shifts into the near-infrared (NIR) at intermediate redshifts. To study the evolution of massive galaxies across cosmic time, as a population, necessitates deep and wide NIR surveys to both probe large volumes and obtain rest-frame optical emission to significant signal-to-noise (S/N).

In this study we use stacking analysis to obtain high-fidelity profiles of the progenitors of massive galaxies out to significant radii (at low z , $r > 60$ kpc). We take advantage of the unparalleled combination of depth and area in the third data release of the UltraVISTA survey (McCracken et al. 2012) to study the structural evolution of massive galaxies out to $z = 3.5$. Due to incompleteness in UltraVISTA at the highest redshifts considered in this study, we also use the deeper CANDELS F160W data from the 3DHST photometric catalogs (Brammer et al. 2012; Skelton et al. 2014; Momcheva et al. 2016) to extend the redshift coverage to $z = 5$. This is a significant gain in redshift over previous studies, and provides the most extensive redshift range over which the profiles of massive galaxies have been traced.

2.2 Sample Selection

2.2.1 Number-density selection

Linking the progenitors of present day galaxies to their high redshift counterparts is challenging, as the merger and star formation history (SFH) of any individual galaxy is not well constrained. One way to circumvent these issues is to assume that galaxies maintain rank-order across cosmic time (i.e., the most massive galaxies today will have been the most massive galaxies yesterday, cosmologically speaking). This assumption predicts a constant co-moving number-density with redshift, an outcome used by van Dokkum et al. (2010) to trace the mass and size growth of galaxies from $z = 2$ (corresponding to $n = 2 \times 10^{-4} \text{ Mpc}^{-3} \text{ dex}^{-1}$). Subsequent studies have used the same assumptions to select progenitors based on a constant *cumulative* number density (e.g., Bezanson et al. 2011; Brammer et al. 2011; Papovich et al. 2011; Fumagalli et al. 2012; van Dokkum et al. 2013; Patel et al. 2013a; Owsnworth et al. 2014; Morishita et al. 2015), which has the advantage over its non-cumulative counterpart of being single valued in mass.

The selection of progenitors and their descendants at a constant cumulative number density implicitly assumes that mergers and in-situ star-formation do not broadly effect rank-order, an assumption which has been shown to result in systematically biased progenitor selection (Behroozi et al. 2013; Leja et al. 2013; Torrey et al. 2015). To account for the affects of mergers on the progenitor mass, we utilize an evolving cumulative number density selection following the prescription of Behroozi et al. (2013), who use halo-abundance matching within a Λ CDM cos-

mology to connect progenitors and their descendants. It is important to note, that we have used the prescription to trace *progenitors* of low redshift massive galaxies, not the *descendants* of high redshift massive galaxies, of which the former yields a steeper evolution in cumulative number density due to the shape of the halo mass function, and scatter in mass accretion histories (see Behroozi et al. 2013; Leja et al. 2013).

2.2.2 The implied stellar mass growth of the progenitors of massive galaxies since $z \sim 5$

In Fig. 3.1 we show the integrated Schechter fits of the mass functions of Muzzin et al. (2013b) between $0.2 < z < 3.0$, and Grazian et al. (2015) between $3.5 < z < 5.5$. These mass functions are based on photometric redshifts determined via ground and space based NIR imaging from the UltraVISTA and CANDELS surveys respectively. In the left-panel of Fig. 3.1, we show our evolving cumulative number density selection based on the abundance matching of Behroozi et al. (2013). The masses implied from a fixed-cumulative number density selection are also shown to illustrate the effect of the bias when the effects of mergers are ignored in the selection. In the right-panel of Fig. 3.1 the implied progenitor masses from the left-panel are plotted for both the fixed and evolving cumulative number density selection, as a function of redshift. The error bars are the uncertainties from the mass functions, which take into account the uncertainties in the photometric redshifts, SFHs, and cosmic variance. The solid grey region represents the scatter in the number densities from the abundance matching of Behroozi et al. (2013), and the hatched regions illustrate an estimate of the mass completeness which is discussed in detail in Sec. 2.2.3.

Below $z = 2$, Fig. 3.1 shows that both constant and evolving cumulative number density selections yield progenitor masses which are consistent within the uncertainties in the mass-functions. However beyond $z = 2$, the bias in the fixed cumulative number density becomes significant, and over-predicts the median progenitor mass. Using the abundance matching technique, we see an overall increase in stellar mass of 1.5 dex since $z \sim 5$. Our fractional mass growth out to $z = 3$ is consistent within the uncertainties with Marchesini et al. (2014) who use the same abundance matching selection for ultra-massive $\log(M_*/M_\odot) \sim 11.8$ descendants, and with Ownsworth et al. (2014), who use a constant cumulative number density selection which is corrected for major mergers to trace progenitors. Using their correction, they find $75 \pm 9\%$ of the descendant mass is assembled after $z = 3$, which is consistent with $\sim 80\%$ which we find in the current study.

We note that in Fig. 3.1 we have selected a progenitor mass for a redshift bin between $3.0 < z < 3.5$ (orange point), even though we have indicated no mass-function for this redshift. The mass-function from Muzzin et al. (2013b) for this redshift range proved to be unreliable for the mass considered due to incompleteness from UltraVISTA DR1 (the source catalog used in generating the mass functions). However, with the deeper exposures from the third data release (DR3) of UltraVISTA, we are complete to the progenitor masses considered out to $z = 3.5$. To calculate the expected progenitor mass between $3.0 < z < 3.5$, we

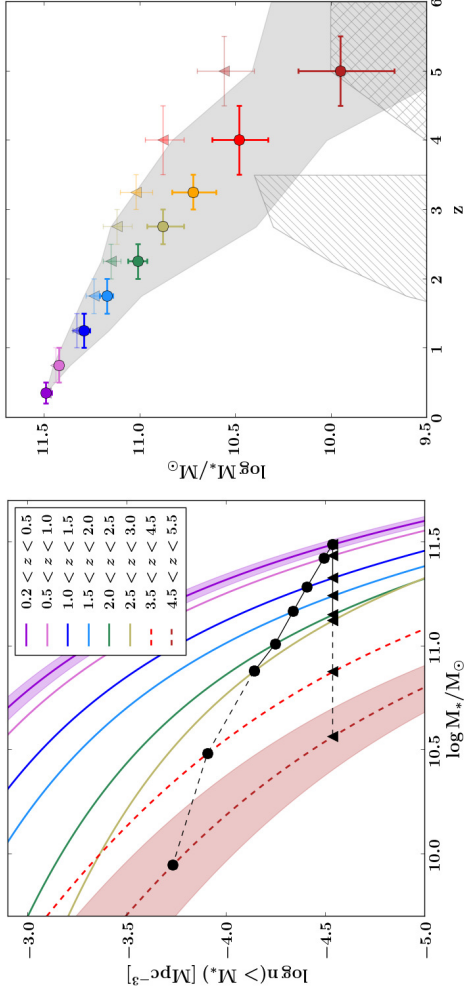


Figure 2.1 *Left*: Integrated mass functions as a function of stellar mass for different z ranges. Solid and dashed lines indicate the mass functions of Muzzin et al. (2013b) and Grazian et al. (2015), respectively, with colour illustrating the redshift. Uncertainties in the mass functions resulting from uncertainties in the photo- z 's, SFH and cosmic variance are shown for the highest- and lowest- z (for clarity). Black circles indicate the cumulative number density selection of Behroozi et al. (2013), with black triangles showing a fixed-cumulative number density selection for comparative purposes. *Right*: The mass evolution of the progenitors of a $\log(M/M_\odot) = 11.5$ galaxy at $z=0.35$. As in the left panel, the circles and triangles show an evolving and fixed cumulative number density selection. The difference between the circles and the triangles illustrate the bias, especially at $z > 2$, resulting from a fixed number density selection. The error-bars in the y-axis and the triangles illustrate the bias, resulting from the mass function. The error-bars in the x-axis represent the redshift range considered. The solid grey-regions indicate the $1 - \sigma$ range from Behroozi et al. (2013), and the hatched regions represent our estimated mass completeness limits which are discussed in Sec. 2.2.3.

linearly interpolated the mass between adjacent redshift bins. We also observe a trend of the uncertainties in the mass function monotonically increasing from low to high redshift. Thus, we similarly linearly interpolated the uncertainties to estimate the uncertainty in mass for $3.0 < z < 3.5$ due to uncertainties in photo- z , SFH and cosmic variance. We also use the uncertainties in the progenitor mass selection as the upper and lower mass bounds for the galaxies that contribute to the resulting stack, thus we select a larger range of masses at higher redshift, than at lower redshift.

It has been shown that the Behroozi et al. (2013) prescription for selecting progenitors performs well in terms of recovering the *average* stellar mass of the progenitors of present-day high-mass galaxies, however this method fails in capturing the diversity in mass of all progenitors as implied by simulations (e.g., Torrey et al. 2015; Clauwens et al. 2016; Wellons & Torrey 2016), which also predict that the scatter in progenitor masses tends to increase with redshift. Given this large scatter, there is no guarantee that the evolution of other galaxy properties, such as size, will follow from the Behroozi et al. (2013) selection. However, in an upcoming paper (Clauwens et al., in prep) we will show that for the property of interest in our study (i.e. the average radial build-up of stellar mass for the progenitors of massive galaxies), the Behroozi et al. (2013) selection yields average agreement with progenitors within the EAGLE simulation.

2.2.3 Data

UltraVISTA

In order to study the evolution of the average properties of massive galaxies, it was necessary to utilize both wide field ground-based, and deep space-based imaging for our stacking analysis. Massive galaxies ($\log(M_*/M_\odot) \sim 11$) are exceedingly rare objects, with low number densities ($\sim 10^{-5} \text{ Mpc}^{-3}$) on the sky (e.g., Cole et al. 2001; Bell et al. 2003; Baldry et al. 2012; Muzzin et al. 2013b; Ilbert et al. 2013; Tomczak et al. 2014; Caputi et al. 2015; Stefanon et al. 2015), and require wide-field surveys to characterize a significant population. To that end, we utilize the NIR imaging from the DR3 of the UltraVISTA survey (McCracken et al. 2012) for our stacking analysis.

The DR3 UltraVISTA catalog (Muzzin et al., in prep) is a K-selected, multi-band catalog constructed from the UltraVISTA survey. Briefly, the survey covers the COSMOS field with a total area of 1.7 deg^2 , with deep imaging in the Y, J, H and K_s bands. The survey also contains ultra-deep stripes with longer exposures which cover a 0.75 deg^2 area, and also includes imaging in the VISTA NB118 NIR filter (Milvang-Jensen et al. 2013). The newest data release is constructed with the same techniques as the DR1 30-band catalog (Muzzin et al. 2013a), with the inclusion of new and higher-quality data to determine photo- z 's, and stellar population parameters. The DR3 survey depths in the ultra-deep stripes are ~ 1.4 magnitudes deeper than DR1 (with 5σ limiting magnitudes in the ultra-deep regions of 25.7, 25.4, 25.1, and 24.9 in Y, J, H and K_s).

Several other datasets have also been added since the first data release including 5 CFHTLS filters, $u^*g'r'i'z'$, as well as 2 new Subaru narrow bands (NB711,

NB816). Most importantly for this analysis we also include the latest data from SPLASH (Capak et al. 2012) and SMUVS (PI Caputi; Ashby et al., in prep). These are post-cryo *Spitzer*-IRAC observations that improve the [3.6] and [4.5] depth from 23.9 to 25.3. Overall this is a 38-band catalog (compared to 30 in Muzzin et al. 2013a), and the substantial increase in depth in the Y, J, H, K_s , [3.6] and [4.5] bands make it a powerful dataset for studying massive galaxies at intermediate and high redshifts.

In the right panel of Fig. 3.1 we have indicated our estimated mass completeness limits with the filled hatched regions. To estimate our mass completeness at $z < 4$, we used the limits on the mass functions from Muzzin et al. (2013b) (which were derived using UltraVISTA DR1), and adjusted the mass limit according to the gain in K-band depth (the K-band limit is 1.5 magnitudes deeper between DR1 and DR3) assuming a constant mass-to-light ratio. Since galaxy mass-to-light ratios decrease with redshift (e.g. van de Sande et al. 2015), this likely represents a conservative estimate of the limiting mass at high redshifts.

CANDELS

As UltraVISTA DR3 is only mass complete for our selection out to $z = 3.5$, we use the reddest band available from CANDELS in order to explore redshifts unobtainable through UltraVISTA. We select galaxies using the photometric data products from the 3DHST survey (Brammer et al. 2012; Skelton et al. 2014) from all 5 CANDELS fields. As an estimate of our mass completeness in CANDELS, we adopt the limiting mass derived from the 75% magnitude completeness limit ($F160W = 25.9$) in the shallower pointings in the GOODS-S and UDS fields as described in Grazian et al. (2015). They estimated their mass completeness using the technique of Fontana et al. (2004), which assumes the distribution of mass-to-light ratios immediately above the magnitude limit holds at slightly lower fluxes, and compute the fraction of objects lost due to large mass-to-light ratios. The estimated completeness for CANDELS is indicated in the right panel of Fig. 3.1 as the grey cross-hatched region.

Although the aforementioned estimates of mass completeness take into account galaxies with varied mass-to-light ratios, it is worth stressing inherent uncertainties when determining mass limits at high redshift. At $z > 3.5$, we increasingly rely on photometric redshifts, as high-fidelity spectroscopic redshifts are fewer in number (Grazian et al. 2015). In addition, sub-mm galaxies (SMGs) likely account for at least a fraction of the progenitors of massive galaxies at high redshift (e.g., Toft et al. 2014), and they have been shown to have high optical extinction (e.g., Swinbank et al. 2010; Couto et al. 2016). As the progenitors selected at $z > 3.5$ of this study tend to be less massive than a typical SMG, we do not expect that they will form a significant fraction of the sample. However, we cannot rule out a tail of less, but still obscured sources to lower masses in the distribution of SMGs. This would have the effect of biasing our high redshift progenitor selection to bluer, less-obscured sources.

Table 4.1 provides a summary of the number of galaxies in the given redshift range, at the implied mass as determined from our evolving cumulative number

Table 2.1. Number of galaxies in each redshift range by catalog

z -range	<i>UVISTA</i>	<i>3DHST</i>
$0.2 < z < 0.5$	16	0
$0.5 < z < 1.0$	56	5
$1.0 < z < 1.5$	96	22
$1.5 < z < 2.0$	166	31
$2.0 < z < 2.5$	276	79
$2.5 < z < 3.0$	466	104
$3.0 < z < 3.5$	160	69
$3.5 < z < 4.5$...	110
$4.5 < z < 5.5$...	154*

*We are incomplete in mass for this point

Note. — Above are the number of galaxies found within the mass ranges outlined in Fig. 3.1.

density selection (see Sec. 2.2.1) from both the UltraVISTA and 3DHST catalogs. In order to boost the number of galaxies in UltraVISTA, we have used galaxies from both the deep (DR1) and ultra-deep (DR3) catalog out to $2.0 < z < 2.5$ where we are complete in mass for the shallower catalog (DR1). For the $3.0 < z < 3.5$ bin, we have only utilized the DR3 catalog, as we are incomplete in DR1. As evident from Table 4.1, UltraVISTA has a larger population of massive galaxies at low redshift, while there are 0 galaxies in all 5 CANDELS fields which are massive ($\log(M_*/M_\odot) \sim 11.5$) at $z = 0.35$, and only 5 galaxies in the next highest redshift bin. However CANDELS is crucial to continue the progenitor selection beyond $z > 3.5$ as we are mass incomplete in this region with UltraVISTA. Additionally, as galaxies had smaller r_e at high redshift (see discussion in Sec. 5.1 and references therein), the space-based seeing of CANDELS is necessary to properly map the density profiles at these epochs. Thus we utilize both data sets in our analysis.

2.3 Rest-Frame Color Evolution

Cumulative number density selection is a method which selects solely on stellar mass, and is therefore blind to other galaxy properties such as levels of star-formation activity. A simple, but effective way to establish star-forming activity in a population of galaxies is to observe where they are located in rest-frame $U - V$ and $V - J$ color space, commonly referred to as a UVJ -diagram. First proposed by Labbé et al. (2005), it is observed that galaxies exhibit a bi-modality in rest-frame UVJ colour space which is correlated with the level of obscured and unobscured star formation. Actively star-forming and quiescent galaxies separate into a ‘blue’ and ‘red’ sequence in the UVJ -diagram (e.g., Williams et al. 2009, 2010; Whitaker et al. 2011; Fumagalli et al. 2014; Yano et al. 2016).

In Fig. 5.2, we plot the rest-frame $U - V$ and $V - J$ colours for all redshift bins to

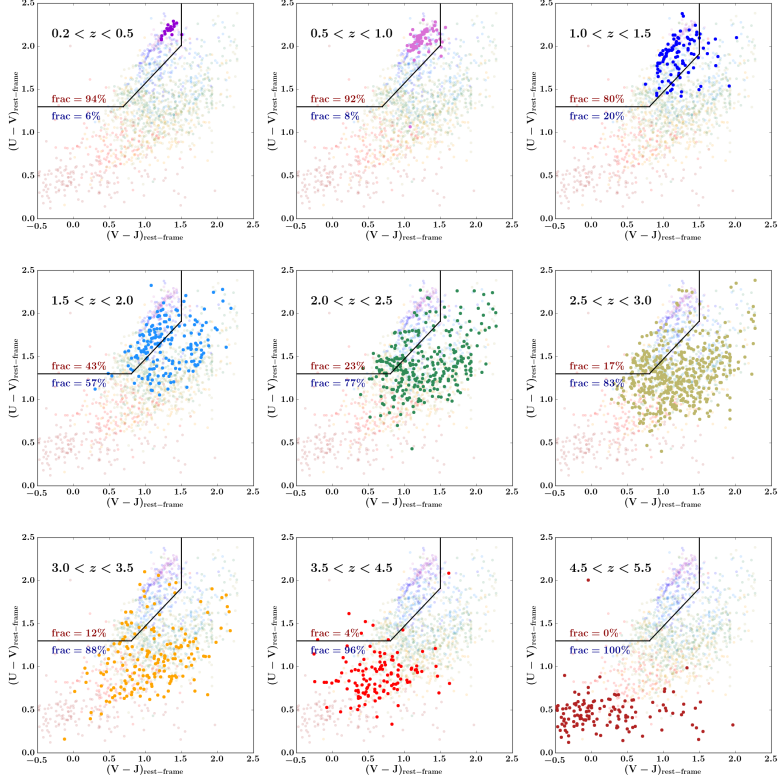


Figure 2.2 Rest-frame UVJ diagrams separated according to redshift bin, for all galaxies used in the stacked images. The redshift increases from top-left to bottom-right. Each panel highlights the galaxies which are both in the redshift, and mass ranges considered in Fig. 3.1, as well as the full sample re-plotted, but washed out to illustrate how each bin relates to the over-all sample. The star-forming/quiescent division from (Muzzin et al. 2013b) in UVJ colour is over-plotted in black. The first seven panels contain galaxies drawn from the UltraVISTA DR3 catalog, and the 8th and 9th panels are from CANDELS-3DHST. There is a clear progression in colour evolution from one redshift bin to the other as galaxies start out in the lower-left region of the diagram, and progress along the star-forming sequence before ending at the tip of the red-sequence. It is important to note that in the highest- z panel we are incomplete in mass and are likely biased towards bluer galaxies.

provide a diagnostic of star-formation activity within each stack. Each of the nine panels represents a different redshift range, with galaxy masses selected according to their expected evolving cumulative number density (see Fig. 3.1). The first seven panels are galaxies from UltraVISTA DR3, and the last two panels contain galaxies from the 3DHST photometric catalog. It is important to note that we are mass incomplete for the $4.5 < z < 5.5$ bin (see Fig. 3.1). However we have chosen to include it as part of our analysis, with the caveat that we are likely biased towards bluer galaxies. Overlaid in each panel are the colour selections used by Muzzin et al. (2013b) to separate quiescent and star forming sequences.

As one progresses in redshift, it becomes apparent from Fig. 5.2 that the number of galaxies selected dramatically increases. This is a result of two competing effects. The first, is that the size of our mass range becomes progressively larger with redshift, as seen in the error bars on the right-panel of Fig. 3.1. By selecting in a wider mass range, we will inevitably select more galaxies. The second effect is that as the number densities of progenitors increases with redshift, we are progressing towards the lower mass end of the mass-functions (Ilbert et al. 2013; Muzzin et al. 2013b; Grazian et al. 2015). Thirdly, at low redshift, the probed co-moving volume is also smaller than at high redshift. The combined effect is to have our lowest redshift, and least populated stack contain only 16 galaxies, whereas our most populated stack at $2.5 < z < 3.0$ contains 276 objects (Table 4.1).

The most prominent trend in Fig. 5.2 comes in the colour evolution of the progenitors across redshift. They begin very blue in both $U - V$ and $V - J$ in the lower-left of the star-forming sequence and progress red-ward along the star-forming sequence to the upper-right until $2.5 < z < 3.0$ before reddening in $V - J$ and joining the quiescent sequence. Assuming our number density selection is valid, this represents a true evolution in UVJ colour.

Fig. 2.3 show the average UVJ colour evolution for each redshift bin, separated into star-forming and quiescent progenitors, and highlights explicitly the trends observed in Fig. 5.2. In this figure, we see most of the early ($z > 3$) colour evolution is driven by the star-forming progenitors. At $z < 3$, star-forming progenitors are beginning to quench in large numbers and the two tracks are broadly parallel until $z < 1$ where the quiescent progenitor fractions are high, and UVJ colour evolution is driven by the quiescent progenitors. This seems to indicate that massive galaxies begin their existence as star forming galaxies, which progress along the blue sequence (via aging of the stellar populations, and increase in stellar mass through star formation), before quenching and joining the red sequence.

The progression in the UVJ -diagram between $0.2 < z < 3.0$ is qualitatively similar to Marchesini et al. (2014) who tracked the progenitors of local ultra-massive ($\log(M_*/M_\odot) \sim 11.8$) galaxies, with the main difference being that this study contain galaxies which are bluer than those of Marchesini et al. (2014). The origin of this difference is rooted in the fact that we select progenitors for a lower local mass galaxy ($\log(M_*/M_\odot) \sim 11.5$). Our galaxies in the higher- z bins are also bluer than the sample of Ownsworth et al. (2016), who select progenitors of massive galaxies based on fixed-cumulative number density. As previously discussed, a fixed cumulative number density selection will yield progenitors which are systematically more massive and thus, redder in $U - V$ and $V - J$ colours, and the inconsistencies in

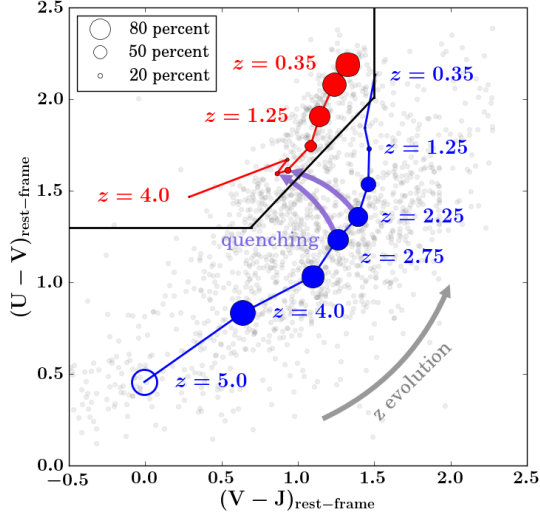


Figure 2.3 Above is the average rest-frame UVJ colour evolution for the progenitors of the quiescent (red symbols) and star-forming (blue symbols) progenitors. The entire sample is plotted in small grey symbols to best illustrate the scatter. The size of the red and blue symbols indicates the quiescent/star-forming fraction (e.g., a large red circle correspond to a high quiescent fraction, and a small blue circle corresponds to a low star-forming fraction). The redshift evolution proceeds from bottom-left to top-right. Purple arrows indicate the direction of quiescence and are labelled for points which bracket a quiescent fraction of 20%. The $z = 5$ point is plotted as an open circle to remind the reader that we are incomplete in that redshift bin, and are likely biased to bluer galaxies.

galaxy properties between the samples is likely attributed to differences in stellar mass.

The progression of galaxies between different redshift bins within Fig. 5.2 and Fig. 2.3 already provides clues as to the structure of the galaxies within them. Numerous studies find that galaxies in the quiescent region of the UVJ -diagram tend to have higher n and smaller r_e (e.g., Williams et al. 2010; Patel et al. 2012; Yano et al. 2016). However, those analyses were for galaxies at fixed masses and did not connect progenitor to descendent, and therefore do not make a direct evolutionary link. In the next section we examine the size and structural evolution of the galaxies selected using the cumulative number density method.

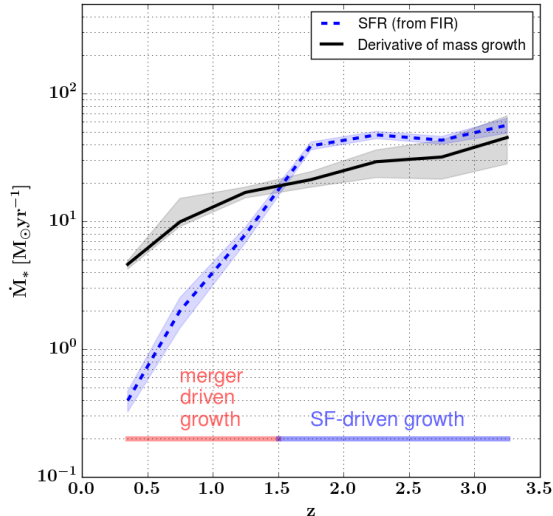


Figure 2.4 The *FIR* implied star formation rates (dashed blue line), compared to the derivative of the mass-redshift evolution (solid black line), with their associated uncertainties (shaded regions). The implied mass assembly from star formation is higher than the derivative of the mass evolution, at $z > 1.5$, and lower at $z < 1.5$. At low redshifts, we see the star formation rates drop precipitously, and that mass assembly cannot be proceeding via in-situ star formation, and growth is likely merger driven.

2.4 Evolution in Far-Infrared Star Formation Rates

In Fig. 5.2 and Fig. 2.3, we see evidence that the evolution of massive galaxies can be broadly separated into two epochs. At $z > 1.5$, galaxies have colours which are consistent with growth mainly through in-situ star formation. At $z < 1.5$, galaxy colours are consistent with quenched systems, with mergers becoming the dominant mechanism for growth. We can estimate this epoch more directly by comparing star formation rates to the mass assembly implied from the evolving cumulative number density selection.

Fig. 2.4 shows the SFR plotted against the derivative of the progenitor mass growth from the right panel of Fig. 3.1. The SFRs are calculated from far-infrared (FIR) luminosities, which are derived from stacks which include *Spitzer* 24 μm , and *Herschel* PACS and SPIRE bands. For each UltraVISTA stack, FIR stacks were generated in the same manner as described in Schreiber et al. (2015). From Fig. 4, of Schreiber et al. (2015), we see that we do not have sufficient numbers of galaxies at $z > 3.5$ with the CANDELS data to expect a FIR detection. Thus we only calculate SFRs out to $z = 3.5$. The FIR luminosities were converted to SFRs

via the relation from Kennicutt (1998), with a factor of 1.6 correction to convert between the Salpeter IMF used in Kennicutt (1998), to the Chabrier IMF used for the DR3 catalog.

In order to more directly compare the net stellar mass growth as implied from the abundance matching technique to the stellar mass growth from star formation, a 50% conversion factor has been applied to the SFR to account for stellar mass which is lost in outflows from stellar winds (see van Dokkum et al. 2008, 2010). From Fig. 2.4, we see that SF is able to account for all of the stellar mass growth at $z > 1.5$, with little to no contribution from mergers. In contrast, the SFR at $z < 1.5$ are insufficient to explain the mass growth, suggesting stellar mass is accreted via mergers.

Between $1.5 < z < 2.5$, the stellar mass growth predicted from star formation is greater than what is found from the abundance matching techniques by $0.1 - 0.2$ dex. This discrepancy is also seen in model and observation comparisons (see Somerville & Davé 2015; Madau & Dickinson 2014), with potential for the FIR SFRs to be over estimated during this epoch (see Madau & Dickinson 2014 and discussion therein). In spite of this, the FIR SFR support the notion that massive galaxies grow via star-formation until $z \sim 1.5$, where merger driven growth dominates, consistent with the rest-frame *UVJ* colours, and what is found in the literature (see Sec. 5.1 and references therein).

2.5 Analysis

2.5.1 Stacked Images

For galaxies at $z < 3.5$, images were stacked using $48'' \times 48''$ cutouts taken from the UltraVISTA mosaics, which contain both deep and ultra-deep stripes. For each cut-out, SEDs were generated using the ancillary data available in the UltraVISTA and CANDELS source catalogs. These SEDs were used to flag potential active galactic nuclei (AGN), which were removed from the resultant stack. The individual cut-outs were also visually inspected to remove objects which were identified as doubles, or triples (i.e., were not separated by SExtractor; Bertin & Arnouts 1996) or in close proximity to saturated stars to maintain image fidelity. In total, $< 4\%$ of the entire sample was discarded.

Cutouts were centered using coordinates taken from the UltraVISTA DR1 (only deep stripes) and DR3 (only ultra-deep stripes) catalogs, with cubic spline interpolation performed for sub-pixel shifting. For galaxies at $z > 3.5$, images were stacked using $24'' \times 24''$ cutouts, taken from the 5 CANDELS fields (AEGIS, COSMOS, GOODS-S, GOODS-N and the UDS), with images centred using the coordinates from the 3DHST photometric catalogs (Brammer et al. 2012; Skelton et al. 2014) with sub-pixel shifting also performed using cubic spline interpolation.

From these cutouts, bad-pixel masks were also constructed using SExtractor segmentation maps. These bad-pixel masks were also used to construct a weight-map for the final stack, by summing the bad-pixel masks (in a similar manner to van Dokkum et al. 2010).

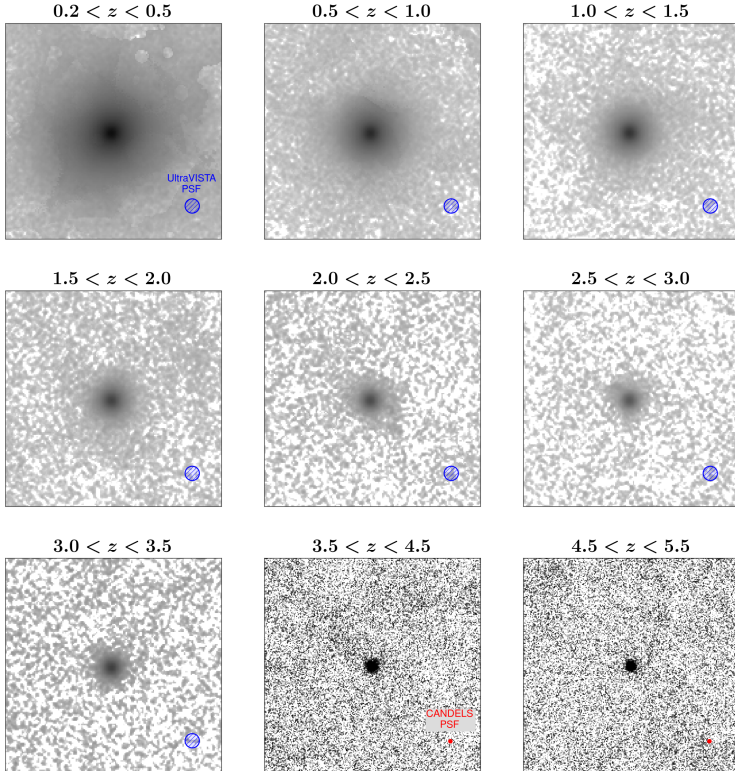


Figure 2.5 Sample stacked images for each redshift bin. The first seven panels contain stacks from the UltraVISTA data, with each panel containing a stack from the band which is closest to the rest-frame $0.5\mu\text{m}$. The Y -band is chosen for stacks at $z < 1$, the J -band at stacks $1 < z < 2$, the H -band at $2 < z < 3$, the Ks -band at $3.0 < z < 3.5$. The UltraVISTA stacks are all displayed at the same colour scale to high-light differences in background and S/N. The last two panels are $F160W$ stacks, and are plotted at the same scale to each other, although different from the UltraVISTA images for clarity, as the background is much higher in the higher- z bins. Overlaid on each panel is a circle which represents the size of the PSF of the data which contributed to the stack, with the ground-based data having a significantly larger PSF than the HST data.

For the UltraVISTA stacks, the ultra-deep and deep cutouts were weighted differently in the final stack as the ultra-deep stripes have an exposure time a factor $\sim 10\times$ greater than the deep stripes. The images are weighted by the expected S/N gain, based on the exposure time (i.e. an image with a factor of ~ 10 more exposure time, will result in a S/N gain of ~ 3). The exact exposures varied between the Y, J, H and Ks bands, with the relative weights between the deep and ultra-deep also changing slightly.

The cutouts were normalized to the sum of the flux contained in the central $1.5'' \times 1.5''$ (corresponding to 10×10 pixel for UltraVISTA images and 25×25 pixel for CANDELS images). A weighted sum was performed on the masked cutouts, with the cutouts contained in the ultra-deep stripes given a heavier weight than those in the deep stripes. This summed image was divided by the weight-map to provide the final stack.

For the UltraVISTA stacks, PSFs were generated similarly to the stacked-galaxy images. Stars within a magnitude range were chosen such that the stars had sufficiently high S/N without being saturated (≈ 16.5 Ks-band magnitude). The stars were treated in the same manner as the stacks of the galaxies (i.e. normalized and averaged). To account for variations in the PSF across the mosaic, 12 different PSFs for each band were generated corresponding to 12 different regions of the mosaic ultra-deep stripes, and 9 for the deep stripes. A final PSF for the relevant band was generated from a weighted average of the 12/9 PSFs, with the weights corresponding to the number of galaxies from each field that went into the making of the stack. Thus, each stack has a uniquely generated PSF.

For the CANDELS F160W stacks, PSFs for each of the 5 fields were taken from the 3DHST-CANDELS data release (Grogin et al. 2011; Koekemoer et al. 2011; Skelton et al. 2014). In a similar manner to the UltraVISTA stacks, the PSF for the relevant band was generated from a weighted average of the PSF from each field, with the weights corresponding to the number of galaxies from each field that contributed to the final stack, thus each F160W stack similarly has a uniquely generated PSF.

Fig. 2.5 displays the results from the stacking analysis. Each panel contains a $24 \times 24''$ display of one of the UltraVISTA bands (either Y,J,H, or Ks), except the last two panels which are stacks of the CANDELS F160W data. The UltraVISTA stacks are all displayed at the same colour scale to highlight the differences in background, which increases with increasing z . The F160W stacks were plotted at a different colour scale for clarity, as the background is much higher.

In addition to the stacks in Fig. 2.5, 100 bootstrapped images were also generated for each stack to constrain uncertainties in the structural parameters determination (see Sec. 2.5.2). Each bootstrapped image also comes with its own unique PSF that reflects the proportion of galaxies from various fields in the same manner as the original stacked images.

2.5.2 Sersic Profile Fitting

Sersic fitting (Sersic 1968) of the stacked and bootstrapped images was performed using GALFIT (Peng et al. 2010), with the only constraints imposed on the fits

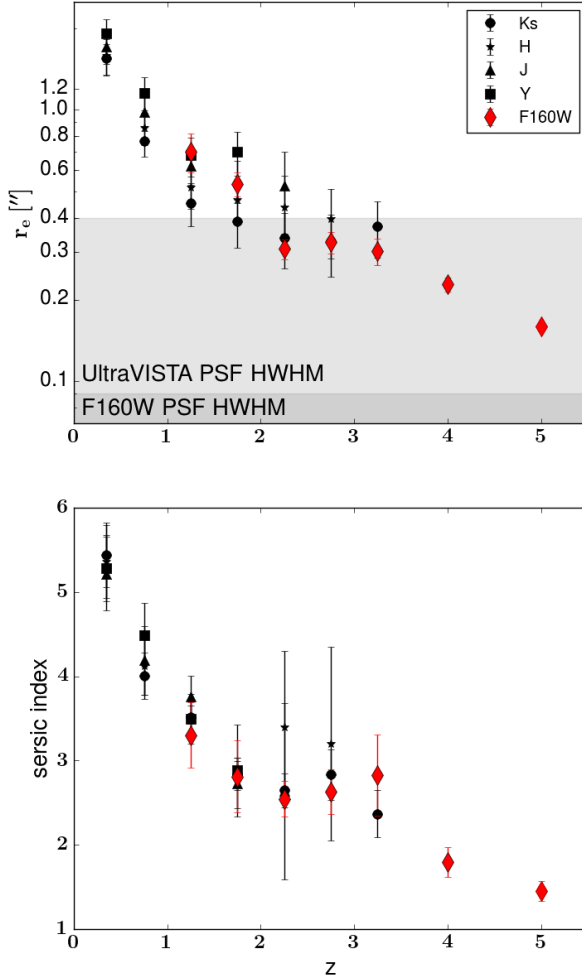


Figure 2.6 *Top*: Best-fit effective radius in units of arc seconds as a function of z for all bands. Points originating from UltraVISTA are plotted in black, with different symbols corresponding to the specific bands as indicated in the legend. HST *F160W* are indicated by red diamonds. The seeing HWHM for both UltraVISTA and HST are displayed in light and dark grey respectively. *Bottom*: Similar to the top, but with n as a function of z . In both panels we see a progression to smaller values with z . In both panels, the $z = 5$ point is plotted as an open symbol to remind the reader that we are mass-incomplete at that redshift.

being to restrict the value of the Sersic indices to between $1 < n < 6$. Fig. 2.6 shows the best fit r_e and n for each band, and each redshift bin, with the uncertainty derived from the 1σ distribution of the bootstrapped fits. The UltraVISTA derived values are in black, with each symbol corresponding to a different band. The F160W values are indicated with red diamonds, with the last symbol plotted unfilled to mark where we are incomplete. The HWHM of the UltraVISTA and CANDELS PSFs are indicated on the top panel in light-grey and dark-grey regions respectively. As seen from the top panel of Fig. 2.6, we resolve the stacked images to within an effective radius for UltraVISTA below $z = 2$, and the r_e is fully resolved for CANDELS in all redshift bins. Additionally, for the redshift bins for which we have stacks for CANDELS and UltraVISTA, the derived sizes and Sersic indices are roughly consistent with one another, suggesting our ground-based structural parameters are reliable.

Absent from Fig. 2.6 are best-fit values for r_e and n below $z = 1$ for the F160W band. In these redshift bins, at the mass ranges considered, there were no galaxies present in the catalogue to contribute to a stack (see Table 4.1). Similarly, best-fit values for the UltraVISTA bands are not present for all redshift bins with the Y, J, H and Ks dropping out at $z = 2, 2.5, 3$ and 3.5 respectively, due to insufficient signal-to-noise in the resultant stack (and that we are incomplete in UltraVISTA at $z > 3.5$).

2.5.3 Evolution in r_e

Due to the progression of redshift between the stacks, the r_e and n are measured at varying rest-frame wavelengths. In order to measure as closely as possible the same rest-frame wavelength, we have measured how r_e and n change with wavelength. In the left panel of Fig. 2.7 we have plotted r_e as a function of rest-frame wavelength. Different colours correspond to different redshift bins, and different symbols demarcate the observed band (with the same symbol convention as in Fig. 2.6). The desired rest-frame wavelength of $0.5 \mu\text{m}$ was chosen to minimize extrapolation, as well as still be red-ward of the optical-break.

At $z < 3$, we have measurements in multiple bands, and find the effective radii decrease with increasing rest-frame wavelength which is consistent with results from previous studies (e.g., Cassata et al. 2011; Kelvin et al. 2012; van der Wel et al. 2014; Lange et al. 2015). However between $2 < z < 3$, the uncertainties are consistent with little to no evolution in r_e with rest-frame wavelength. When considering the evolving properties of the progenitors with redshift, this result is also consistent with the literature. van der Wel et al. (2014) who measured the sizes of galaxies from CANDELS at $0 < z < 3$, found the size-gradient with rest-frame wavelength was steepest for galaxies at high-mass, and low-redshift, and flatter for low-mass galaxies. As the progenitors decrease in mass with redshift, we expect a flattening of this gradient. The difference in size-gradients is also seen in local populations. Kelvin et al. (2012) found size-gradients to be flatter for late-type galaxies in the GAMA survey. Because we only have measurements in one band for $z > 3.5$, and we are dominated by late-type galaxies at high redshift, we have not extrapolated r_e between $3.5 < z < 5.5$ and assume the measurement is

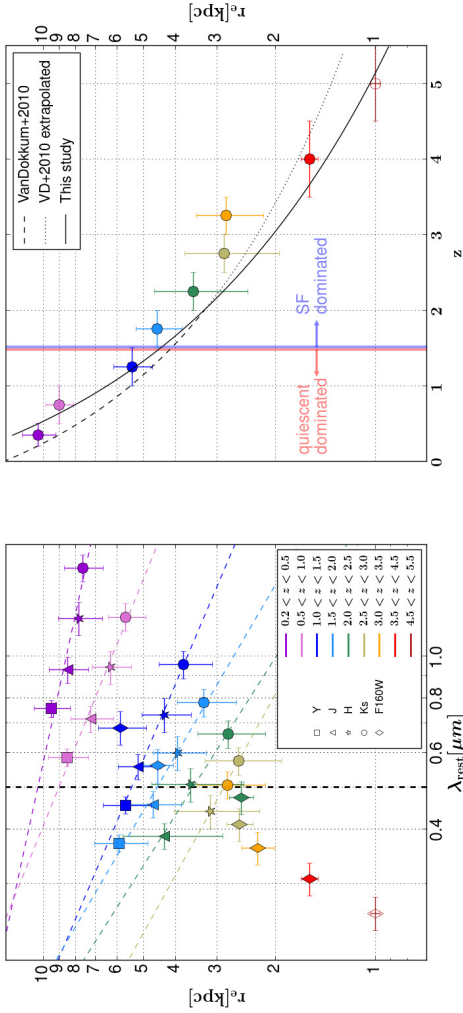


Figure 2.7 *Left*: The effective radius plotted against the rest-frame wavelength for the stacks in all bands measured. Different shaped symbols correspond to the observed band with the same symbol convention as Fig. 2.6. Each color corresponds to a different redshift range, with the color convention the same as Fig. 3.1, including plotting the $4.5 < z < 5.5$ symbol as open-faced to remind the reader that we are mass incomplete for that z -bin. Dashed coloured lines are linear best fits to the data, with the bold, black, vertical dashed line marking the rest-frame $0.5 \mu\text{m}$ point, which the data at $z < 3$ are extrapolated/interpolated to, so as to compare the same rest-frame sizes. z -ranges with only one measurement are not extrapolated for reasons discussed in Sec. 2.5.3. *Right*: The size evolution of the progenitors of massive galaxies since $z \sim 5$. Colored circles are the extrapolated/interpolated point at $z < 3$, or the ‘raw’ measurements at $z > 3$. Over plotted are the size- z relation of van Dokkum et al. (2010), as well as the size relation derived for this study.

representative of the r_e at $0.5 \mu\text{m}$. This is assuming that the size-gradient will be flat for low-mass, late-type galaxies at high redshift.

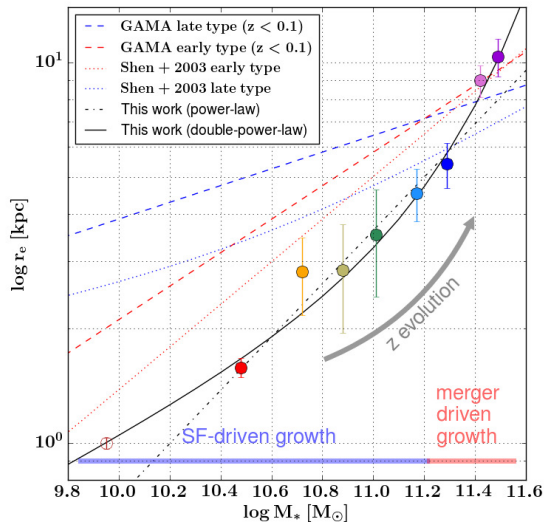


Figure 2.8 The implied mass-size evolution of the progenitors of massive galaxies. Circles are measurements from the stacks from the present study, with each point representing a different redshift. The r_e plotted above are the same values taken from the right-panel of Fig. 2.7. Symbol color plotting convention is the same as Fig. 3.1, with the lowest- z points corresponding to the most massive galaxies, and monotonically decreasing to the highest- z . We have plotted the highest- z point as an open face symbol to remind the reader we are mass incomplete for that z -bin. Plotted above are the g -band local mass-size relations for late (dashed blue line) and early type (dashed red line) galaxies from the *GAMA* survey (Lange et al. 2015), as well as the mass-size relations from Shen et al. (2003). For the lowest 2 z bins (i.e. $z < 1$), our galaxies fall precisely on the local mass-size relation for early type galaxies, but are systematically below the relations at higher z . Also plotted above are the best fit single and double power-law relations to our data.

In the right panel of Fig. 2.7, we have plotted r_e at $0.5 \mu\text{m}$ as a function of redshift. It is clear from both panels of Fig. 2.7 that the r_e decreases out to $z = 5$ which is consistent with previous results using a diverse set of methods to select progenitors (e.g., van Dokkum et al. 2010; Williams et al. 2010; Damjanov et al. 2011; Mosleh et al. 2011; Oser et al. 2012; Barro et al. 2013; Patel et al. 2013a; Straatman et al. 2015; Owsnorth et al. 2016). In spite of the different choice of progenitor selection, below $z = 2$ our measurements fall broadly on the same relation found by van Dokkum et al. (2010) (our values are systematically larger, but this is likely a reflection of our slightly higher mass selection). This result is

not surprising, and the consistency is reflected in the right panel of Fig. 3.1, where at $z < 2$, the mass of the progenitors chosen using a fixed vs. evolving cumulative number density are within the uncertainties in both the mass function and the semi-analytic models. Although we measure a slightly steeper relation than van Dokkum et al. (2010), it is surprising how well the relation is extrapolated at $z > 2$ given that we are selecting galaxies which are distinct in mass from the fixed-cumulative number density selection.

In Fig. 2.8 we investigate the evolution of the mass-size plane. We have taken the values of r_e from the right panel of Fig. 2.7, and plotted them against their respective progenitor masses, with the highest mass associated with the lowest redshift bin. For comparison purposes, we have over-plotted the mass-size relations from Shen et al. (2003) and Lange et al. (2015) for both early and late type galaxies. For Lange et al. (2015), who investigate the mass-size relations as a function of rest-frame wavelength, we use their g -band relations which corresponds most closely to a rest-frame wavelength of $0.5 \mu\text{m}$. The measured r_e from our stacking analysis fall on the SDSS and GAMA mass-size relations for early-type galaxies at $z < 0.1$. However for all other redshift bins, our galaxies fall below the local-mass size relation, consistent with van Dokkum et al. (2010). Also plotted in Fig. 2.8 are simple single (dash-dot line) and double (solid line) power-law fits of the form

$$r_e = aM_*^b \quad (2.1)$$

$$r_e = \gamma M_*^\alpha \left(1 + \frac{M_*}{M_0}\right)^{\alpha-\beta} \quad (2.2)$$

From Fig. 2.8, we see that the double power-law is a more appropriate fit for our data, with the parameters $\gamma = 2.9 \times 10^{-4}$, $\alpha = 0.35$, $\beta = 2.1 \times 10^3$ and $\log(M_0/M_\odot) = 14.77$. Continuing with the plotting convention in previous figures, our $4.5 < z < 5.5$ point has been plotted as an open-face symbol to highlight incompleteness issues within that bin. It is interesting to note that this point has not been included in any of the power-law fits, and the fact that it falls on on the extrapolation of the double power-law is not designed.

The evolution in the mass-size relation in Fig. 2.8 can be broadly separated into two phases. At $z > 1.5$, the mass-size evolution is relatively linear (in log-log space), with most points falling along a single power-law. At $z < 1.5$, the size growth becomes more efficient, and no longer follows the same single power law as before. This is broadly consistent with patterns we have seen in Fig. 2.3 and Fig. 2.7 i.e., that star-formation and mergers are dominating mass and size growth at different epochs, with this changeover occurring at $z \sim 1 - 2$. Before this time, mass was primarily added via star formation, which has been shown to be ineffective at altering the structure of massive galaxies (Ownsworth et al. 2012). At these redshifts, we see a marked increase in the quiescent fraction of the progenitors. As star formation is no longer an available pathway to mass growth, the growth is dominated by minor mergers, which efficiently increases the r_e (see Sec. 5.1 and references therein).

2.5.4 Evolution in n

Fig. 2.10 is analogous to Fig. 2.7, except we investigate how the Sersic index n changes with rest-frame wavelength in place of r_e . From the left panel of Fig. 2.10 we see little to no evolution in n with wavelength at any redshift. We have therefore taken an average n weighted by the bootstrapped uncertainty in each band to measure a representative n for each redshift bin. At $z > 3$ where we only have one measurement for each stack, the measurement was considered representative. The resulting values are plotted in the right panel of Fig. 2.10.

Fig. 2.10 shows a clear downward trend of n with redshift, consistent with previous findings out $z = 2$ (e.g., van Dokkum et al. 2010). This trend is also expected given the evolution in the quiescent fraction. Actively star forming galaxies tend to have lower n /are more centrally concentrated than their quiescent counterparts (e.g., Lee et al. 2013; Freeman 1970; Lange et al. 2015; Mortlock et al. 2015), thus at $z > 1$ the decrease in n is likely driven by morphological changes between each redshift bin which we also see reflected in the evolution of the mass-size relations (Fig. 2.8). van Dokkum et al. (2010) also found n to decrease with redshift, although their relation is steeper than the one measured in the current study. However the $n - z$ relation from van Dokkum et al. (2010) was derived from galaxies at $z < 2$, where the slopes are comparable, but where we measure systematically higher n .

2.5.5 Mass Assembly

Equipped with measurements of r_e and n , we can investigate surface-density profiles, and mass assembly as a function of radius. To generate these profiles, we have assumed that the mass-to-light ratio is constant across the profile, and that all the mass can be found within a radius of 75 kpc. Given these assumptions, and that the integrated mass within 75 kpc must equal the total mass found in the right panel of Fig 3.1 (i.e., the same constraints used in van Dokkum et al. 2010), we have generated stellar-mass density profiles which can be found in Fig. 2.9.

Fig. 2.9 shows the Sersic fits using the values of r_e and n for each redshift bin in the right panels of Fig. 2.7 and Fig. 2.10 respectively. The transition between the solid and dashed lines for each profile marks the point when the error in the background becomes significant. Since many of the values of r_e and n are either interpolated, or averaged (see Sec. 2.5.3 and Sec. 2.5.4), the profiles from which this transition point was determined were the closest to the rest-frame wavelength of $0.5 \mu\text{m}$ (these are the same bands which are displayed in Fig. 2.5).

Fig. 2.9 illustrates that the majority of mass build-up in galaxies since $z = 4$ occurs in the outskirts, consistent with previous findings and the inside-out growth paradigm for massive galaxies (van Dokkum et al. 2010; Toft et al. 2012; Bezanson et al. 2013; van de Sande et al. 2013; Belli et al. 2014a; Margalef-Bentabol et al. 2016). It is only at $z = 5$ that we begin to see significant growth in the inner regions. Important to note is that as we are incomplete in that redshift bin, we will be biased towards blue, and possibly diskier galaxies which would likely have lower values of n . However given the trend of Sersic index with redshift found in Fig. 2.10, this does not seem to be an unreasonable depiction of the progenitors.

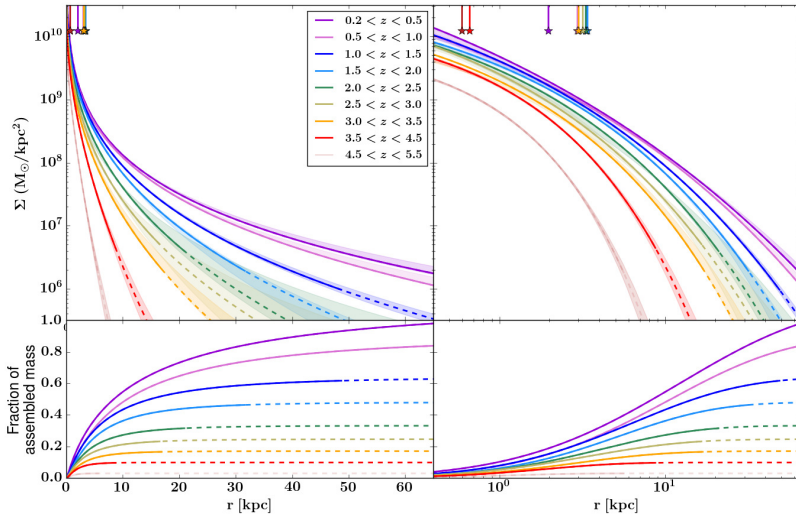


Figure 2.9 *Top*: The projected surface mass-density profiles for our stacks (presented in both log-linear and log-log scales). Each profile is a Sersic, with the r_e and n taken from the right panels of Fig. 2.7 and Fig. 2.10, with the constraint on normalization that the integrated mass within 75 kpc be equal to the implied progenitor mass from Fig. 3.1. The faded filled region corresponds to profiles within the 16th and 84th percentile from the bootstrapped images. The transition from solid to dashed line in the profile marks the point where the error in the profile is at the level of the background. The PSF HWHM for each redshift is also marked with a vertical line ending in a star at the top of each plot. *Bottom*: The fraction of assembled mass with radius for each profile (presented in both log-linear and log-log scales). The curves are all normalized to the total mass at $0.2 < z < 0.5$. The curve for $4.5 < z < 5.5$ is faded to remind the reader that we are mass incomplete in that z -bin.

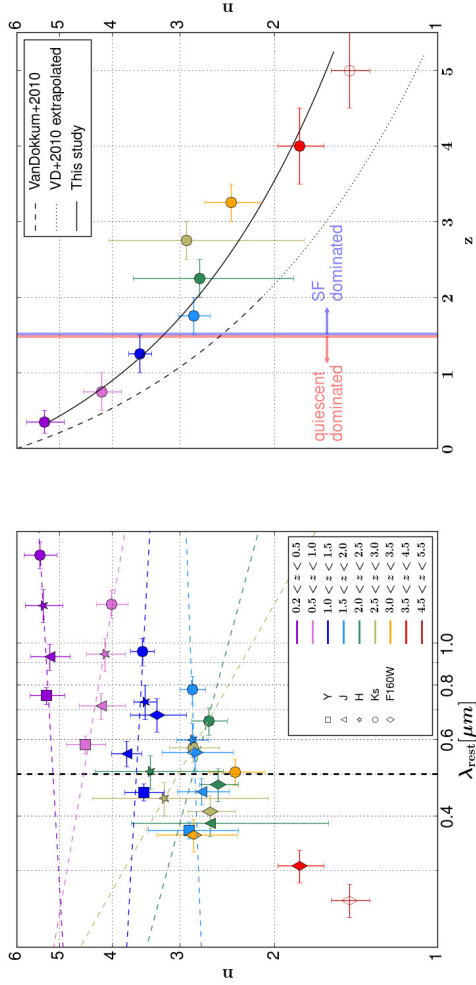


Figure 2.10 The same figure as Fig. 2.7, but with Sersic index instead of the effective radius. *Left*: Sersic index plotted against the rest-frame wavelength with the same plotting convention as Fig. 2.7. As the relation between n and λ_{rest} is consistent with flat, there is no extrapolation to the $0.5 \mu\text{m}$ point. Instead, the values are averaged to produce a representative n for each z -bin. *Right*: The evolution of n with z . Over-plotted are the best fit relation for this study, as well as the relation from van Dokkum et al. (2010).

In Fig. 2.11, we have divided the surface mass density profile for each redshift bin from Fig. 2.9 by the surface mass density profile at $0.2 < z < 0.5$. In this way, we are able to trace the fractional mass assembly as a function of radius. At the highest redshift bins, we see the central regions are the first to form, with very little of the stellar mass beyond 3 kpc in place at $z \sim 5$. Between $3.0 < z < 4.5$, we see rapid growth, with the fraction of mass assembled in the inner regions more than doubling. It is also in this redshift interval that a not insignificant fraction of stellar mass is assembled between 3 and 10 kpc. We can trace the redshift of formation as a function of radius by tracing the horizontal dashed-line in Fig. 2.11, which marks the point at which half of the stellar mass was assembled. As you trace from small to large radii, the dashed line crosses different coloured regions, indicating that the interior regions were the first to assemble, with the outer regions assembling at later and later times, indicative of ‘inside-out’ growth.

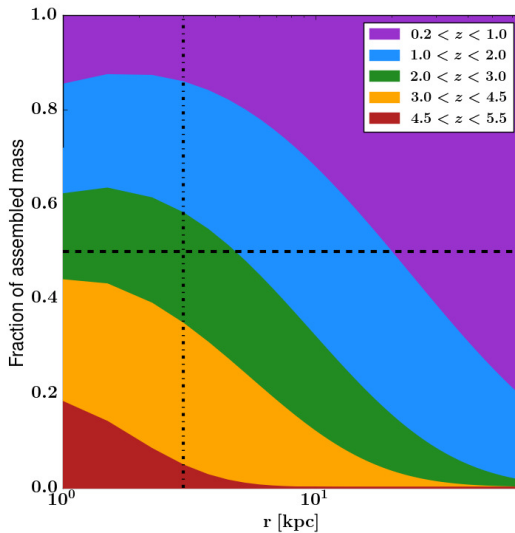


Figure 2.11 The fractional build-up of stellar mass, as a function of radius, assembled at various z intervals (i.e. each mass profile in Fig. 2.9 divided by the mass profile for $0.2 < z < 0.5$). The horizontal dashed lines marks the 50% assembly point, and the vertical dot-dashed line is drawn at the 3 kpc point for clarity. From this plot, the formation redshift for the interior vs. exterior regions can be seen, with the inner regions containing 50% of their final stellar mass between $2.0 < z < 3.0$, with the outer region z of formation lagging behind.

We can trace this growth quantitatively by considering the total mass in and outside the 3 kpc boundary. We have de-projected the surface density profiles of Fig. 2.9, and separated the mass growth into stellar mass assembly that is within $r < 3$ kpc, and exterior to $r > 3$ kpc. The total mass assembly is indicated in black,

and is the same mass assembly seen in the right panel of Fig. 3.1. From the red line, we see continuous, albeit decelerating, mass assembly from $z = 5$ to $z = 0$. This is inconsistent with previous works such as van Dokkum et al. (2010) and Patel et al. (2013a) who found the interior regions are consistent with no assembly since $z = 2$, oft cited to be evidence of ‘inside-out’ growth, although it depends on precisely what is meant by this term.

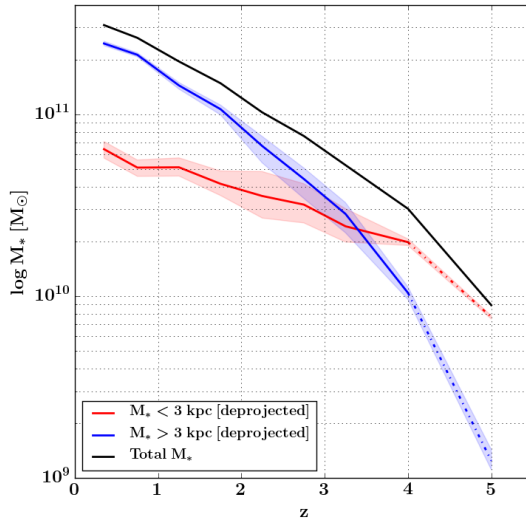


Figure 2.12 The total projected mass within 3 kpc (red-line) and outside 3 kpc as implied by integrating the profiles from Fig. 2.9. The last symbol is plotted as open faced to remind the reader that we are mass incomplete in that z -bin. There is growth in both radial regions, however the growth is not self-similar with the growth outside $r = 3$ kpc proceeding at a faster pace than the inner regions.

It is important to note from Fig. 2.11 and Fig. 2.12 that even though the regions outside 3 kpc experience a greater growth rate than the inner regions, there is still significant mass build-up from $z = 5$ to $z = 0$ in the interior. Although the growth between the inner and outer regions is not self-similar, the growth is not necessarily ‘inside-out’ as described in previous works (e.g., van Dokkum et al. 2010; van de Sande et al. 2013), especially when considering the mass assembly at $z > 3$. At these redshifts, significant stellar mass is assembled at all radii (although mass accretion is concentrated in the central regions).

2.5.6 Comparisons with simulations

There have been many comparisons between the mass growth of galaxies in extra-galactic surveys (i.e. mass functions) to hydrodynamical galaxy simulations (e.g.,

Vogelsberger et al. 2014; Schaye et al. 2015). In fact, the EAGLE simulation has been calibrated to reproduce the galaxy stellar mass function at $z = 0$. However, there remain few examples (e.g, Snyder et al. 2015; Wellons et al. 2015) in the literature which explicitly compare the evolution of structure in simulations to observations. In this section, we endeavour to make such a comparison.

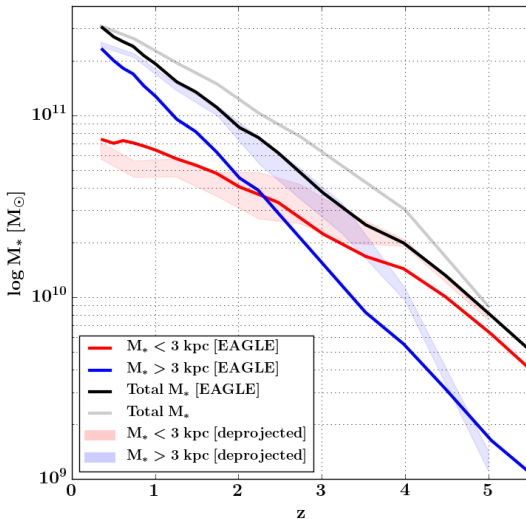


Figure 2.13 Above show the the build-up of stellar mass inside (red line) and outside (blue line) a 3 kpc aperture as predicted by the EAGLE simulation, as well as the total stellar mass evolution (black line). The faded colours is the mass evolution from this study, with the colours corresponding to the same regions as the simulations. The simulations show rapid build up of the outer regions, which is qualitatively similar to the data. The main difference between the observations and the simulations is the total mass evolution proceeds more rapidly in the simulations, with most of the effects see in the build up of the outer regions.

In Fig 2.13, we see how the mass assembly as implied by our observations compares to the EAGLE simulation (Schaye et al. 2015). In Fig. 2.13, we see the total mass assembly (black line), the mass assembly within a 3 kpc aperture and the mass assembly outside a 3 kpc aperture. Also plotted in Fig. 2.13 are the de-projected aperture masses from this study for comparison. The progenitors in EAGLE are defined as the ‘true’ progenitors, and are selected in a similar method to the dark-matter halo mergers trees from Behroozi et al. (2013) which inform the abundance matching technique, i.e. only the most massive progenitor from the precursors of a merger is considered. The progenitors were traced from all galaxies within the EAGLE simulation that have a stellar mass within 0.1 dex of $\log(M_*/M_\odot) \sim 11.5$ (i.e. chosen to match the starting point of this study), which

amounted to 24 galaxies. The aperture masses from EAGLE quoted above are averages from the progenitors of these 24 galaxies.

A qualitative comparison between the simulations and the observations show remarkable agreement. For the mass within 3 kpc, the agreement is always within a factor of 2, which is within the uncertainty associated with the assumptions made when determining stellar masses from photometry (Conroy et al. 2009). Both methods predict the same overall trend i.e. that there is a steady build up of stellar mass within 3 kpc, and rapid assembly at later times at radii larger than 3 kpc. The main difference between the simulations and observations is that EAGLE predicts a more rapid assembly of the progenitors. The progenitors in EAGLE must assemble more mass in the same period of time in order to result in the final stellar mass of $\log M_*/M_\odot = 11.5$ at $z \sim 0.3$. This offset is not entirely unexpected, given differences between the evolution of the observed and simulated galaxy stellar mass functions at high- z in the mass ranges considered for this study ($\sim 10^{10} - 10^{11} M_\odot$, Furlong et al. 2015).

The progenitors in EAGLE must assemble more mass in the same period of time in order to come to the same descendant mass by $z \sim 0.3$; and given the agreement with observations at $r < 3$ kpc, nearly all of this mass growth must occur in the outer regions. This suggests the progenitors in EAGLE are more centrally concentrated than observed, except at $z > 4$. Between $4 < z < 5$, the fraction of stellar mass outside a 3 kpc aperture is broad agreement with the observations, which does not follow the trend at $z < 4$. One possible reason for this is the effective radius at these redshifts is close to 1 kpc, which suggests nearly all of the total bound mass in the galaxy would be within 3 kpc, which is not true at lower redshifts.

Some caveats that could affect the above comparison are some assumptions that were made in the observations, in particular the assumption of a constant mass-to-light ratio for our surface mass density profiles. If there is a strong gradient of stellar age with radius in the progenitors, and the interiors are older (which would be consistent with what we see in Fig. 2.11), then we would over-predict the fraction of the total stellar mass which is located at large radii, bringing us closer to agreement with the simulations. A similar effect would be expected if there are also strong gradients in dust. An analysis of forthcoming virtual observations from EAGLE with the effects of dust and inter-cluster light taken into account would be a better comparison, the investigation of which is beyond the scope of this paper.

2.6 Discussions and Conclusions

2.6.1 Mass and size growth at $z < 2$

In this paper, we have selected the progenitors of today's massive galaxies through an evolving cumulative number density technique, and have made image stacks to infer their evolution with redshift. Based on rest-frame $U-V$ and $V-J$ colours, we find the progenitors of massive galaxies become increasingly star forming out to higher redshift, and by assuming Sersic profiles for the mass distribution, we find

the progenitors decrease in both r_e and n . These trends are qualitatively similar to previous studies which select based on fixed (e.g., van Dokkum et al. 2010; Patel et al. 2013a; Ownsworth et al. 2014), and evolving (Marchesini et al. 2014) cumulative number densities at $z \lesssim 2$

Although the qualitative trends are consistent with the literature, there are quantitative differences, especially in regards to the evolution of the central mass densities with redshift. Previous works (e.g., van Dokkum et al. 2010; Patel et al. 2013a; van Dokkum et al. 2014) have found little to no mass assembly in the inner regions ($r < 2$ kpc), and find that mass assembly occurs in an inside-out fashion with the majority of mass growth since $z \sim 2$ occurring at $r > 2$ kpc (although in van Dokkum et al. 2010 at ~ 1 kpc, there is a spread in mass-density of at least 0.1 dex since $z = 2$ suggesting modest mass growth). In this study, we find the central regions have accumulated $\approx 50\%$ of their mass between $2.0 < z < 2.5$, but continue to experience mass growth out to $z = 0.2$, albeit at a lower rate (i.e. we find $\sim 90\%$ of the mass within 2 kpc was in place by $z \sim 1$).

The suspected cause of this discrepancy is the differences which arise between a fixed vs. evolving cumulative number density selection. By using a fixed cumulative number density selection, one is biased towards the most massive progenitors (e.g., Clauwens et al. 2016; Wellons & Torrey 2016). This is a result of the fact that an abundance matching technique (i.e Behroozi et al. 2013) predicts higher number densities with increasing redshift, whereas a fixed cumulative number density will select galaxies at a steeper point in the mass function which is inhabited by higher mass galaxies. We have tested this hypothesis by re-measuring the surface mass density profiles for a fixed cumulative number density selection (see Fig. 3.1 for the mass assembly history), and do find the redshift evolution in central regions of the stellar surface mass density profiles is considerably weaker than for an evolving number density selection (Fig. 2.14). Details of this analysis can be found in an attached appendix.

In contrast to a fixed cumulative number density selection, van Dokkum et al. (2014) selected galaxies based on their stellar surface mass density within 1 kpc (i.e. 'dense cores'), and found evidence that the interiors are formed first, with the outer radii forming around them. This inconsistency can also be attributed to selection, and the progenitors van Dokkum et al. (2014) select are likely a subpopulation of the progenitors of massive galaxies. Since they are selected on central stellar density, and central stellar density is correlated with quiescence, they will not select star forming progenitors. This is evidenced by the differences in quiescent fraction at $2.0 < z < 2.5$; van Dokkum et al. (2014) find a quiescent fraction of 57%, whereas the selection of the current study has a quiescent fraction of 23% in the same redshift range.

The most massive progenitors are likely to host older stellar populations, have less star formation, and more compact configurations due to rapid early assembly. As these progenitors would have assembled first, they experience more passive evolution in their central regions between $z = 2$ and today (e.g., van de Sande et al. 2013). The star forming progenitors however, still must quench, and might involve more violent events, such as disk instabilities which result in compaction, i.e. the driving of mass towards smaller radii (Dekel & Burkert 2014; Barro et al.

2014). By averaging these populations, one would expect modest gains in stellar mass density in the central regions, which is what is seen in our analysis.

An important caveat to consider when selecting progenitors at systematically higher number densities is the effect of a lower normalization to the mass profiles. Our profiles are designed such that 100% of the stellar mass, as determined from the mass functions as outlined in Fig. 3.1, is contained within 75 kpc. If at each z step we have a slightly lower mass selection than studies based on a fixed cumulative number density selection, the normalization of the profile will trend to lower values which imposes sustained mass growth in the central regions (see Fig. 2.14, and discussion in the appendix).

Although we find the progenitors continue to assemble mass at all radii, the growth rate at small and large radii is not self-similar. The fractional growth rate is higher at larger radii, consistent with the idea that minor mergers play a dominant role in the mass assembly at $z < 1.5$, and especially at $z < 1$ as found by Newman et al. (2012); Whitaker et al. (2012); Belli et al. (2014b, 2015); Vulcani et al. (2016).

This is also in agreement with our quiescent fractions, which are $> 90\%$ at $z < 1$, suggesting that the majority of the mass growth cannot be from star formation. However between $1 < z < 2$ our star-forming fraction exceeds 50%, suggesting the increasing importance of star formation in mass assembly, which is in broad agreement with Vulcani et al. (2016) who find star-formation and minor mergers play equal roles in mass growth during this epoch. Additionally, $H\alpha$ maps of massive star-forming galaxies between $0.7 < z < 1.5$ reveal that the disk scale lengths are larger in $H\alpha$ than in the stellar continuum, suggesting that star formation also contributes to the mass build-up at large radii (Nelson et al. 2016), and not just in the inner regions.

2.6.2 Mass and size growth at $z > 2$

In addition to comparisons with other works, which are largely limited to $z < 2$, we have selected progenitors, and generated stacks for galaxies out to $z = 5.5$. In this regime we see a continuation of the trends at $z < 2$, i.e. progenitors are smaller, and have Sersic indices which imply more disk-like configurations than spheroidal. This is consistent with the evolution of our quiescent fraction which continues to decrease with increasing z , suggesting the progenitors are dominated by star forming galaxies which also tend to have disk-like morphology, which is observed in massive galaxies at high redshift (e.g., van der Wel et al. 2011; Wuyts et al. 2011; Bruce et al. 2012; Newman et al. 2015). This is in agreement with the prediction of Patel et al. (2013a) who posited that the progenitors of massive galaxies at $z > 3$ will continue the trend towards smaller sizes.

The trends in the evolution of the mass-size relation, the r_e , the Sersic index, the UVJ colour evolution, and the FIR derived SFRs all corroborate the idea that $z \sim 1.5$ represents a transitional period in how the progenitors of massive galaxies assemble their mass. At $z > 1.5$ the UVJ colours and the FIR SFRs suggests the progenitors are actively forming stars, and the Sersic index suggests those stars are consistent with being distributed in an exponential disk. The change in power-

law slope at $z \sim 1.5$ in the evolution of the mass-size plane suggests a change in assembly method; one in which the size evolves more efficiently with mass than at higher redshift, consistent with the minor merger scenario (see Sec. 5.1 and references therein). This is further corroborated by the fact that the FIR SFR is insufficient to account for the rate of stellar mass assembly at $z < 1.5$ (Fig. 2.4).

This study supports the scenario that the progenitors of massive galaxies begin with a disk-like morphology with the disk forming concurrently with the central regions (i.e. the ‘bulge’). At some point, the disk morphology is destroyed, either by major mergers, or disk instabilities which may also be responsible for the increase in quiescent fraction. Evidence of disks (e.g., van Dokkum et al. 2008; van der Wel et al. 2011; Wuyts et al. 2011; Bruce et al. 2012; Bell et al. 2012) and rotation (Newman et al. 2015) in massive compact quenched galaxies are seen at intermediate ($1.5 < z < 3$) redshifts which confirms that at least *some* of the massive progenitors host/hosted disk-like morphology. By $z = 1.5$, assembly is less violent, with mass growth dominated by minor mergers, and more passive quenching (i.e. gas exhaustion) until $z = 0$.

The scenario that the progenitors of massive galaxies begin as disks have support in cosmological simulations. Fiacconi et al. (2016b) simulated the assembly of the main progenitor of a $z = 0$ ultra-massive elliptical, and found the progenitor to be disk dominated, with an exponential brightness profile at $z > 6$ which had experienced several major mergers at $z > 9$. The ‘survival’, or more accurately, the reassembly of the disk after a major merger is feasible, provided the major mergers are sufficiently gas rich (e.g., Hopkins et al. 2009). Fiacconi et al. (2016b) also calculated the Toomre parameter for their simulated disk and found it to be stable against fragmentation for all resolved spatial scales, with the disk supported by a turbulent inter-stellar medium thought to be due to feedback from star-formation. They also predict, that gas-rich star forming disks at $z > 5$ should not host a significant bulge, but is rather built up by mergers occurring at $2 < z < 4$ (Fiacconi et al. 2016a). This is consistent with our analysis which show the majority of the stellar mass in the central regions (i.e. $r < 1$ kpc, which we take as a proxy for the bulge) is assembled between $2.0 < z < 5.5$.

Stacking analysis is a useful tool to probe the average properties of low-surface brightness features of a population of galaxies. However, specific aspects of the morphology are lost in a stack. To verify our hypothesis about the nature of the progenitors of today's massive galaxies will require resolution and sensitivity of spaced based observatories such as HST. At high- z , the rest-frame optical emission is shifted further into the infrared, of which future space observatories such as JWST which will observe at wavelengths beyond the K -band, will prove to be invaluable in determining the nature of ‘regular’ galaxies at $z > 2$.

2.7 Summary

To briefly summarize the paper, we have traced the stellar mass evolution of the median progenitors of $\log M_*/M_\odot = 11.5$ galaxies at $z = 0.35$ using abundance matching techniques. Using photometric data from the UltraVISTA and 3DHST

surveys and their associated catalogs, we have used stacking analysis to trace the mass assembly of the progenitors out to $z = 5.5$. By fitting the images stacks with 2D convolved Sersic profiles, we have found the following.

1. Selecting progenitors based on an evolving cumulative number density selection results in progenitors that are less massive than if selected based on a fixed cumulative number density selection. This discrepancy becomes significant at $z > 2$.
2. The progenitors of massive galaxies become progressively more star forming, with star forming fractions exceeding 50% at $z > 1.5$ as determined by their rest-frame $U - V$ and $V - J$ colours.
3. The progenitors decrease in both effective radius and Sersic index with increasing redshift, which is consistent with the picture that the progenitors of today's massive galaxies began with disk-like morphology.
4. The progenitors continue to assemble mass at all radii until $z = 0.35$, which suggests a more complex mass assembly then 'inside-out' growth.
5. Even though galaxies continue to assemble mass in their interiors to low redshift, the redshift at which half of the resultant stellar mass is assembled is higher for the interiors than the exterior regions, with $z_{f,r=3 \text{ kpc}} \sim 2 - 3$, and $z_{f,r=10 \text{ kpc}} \sim 1 - 2$.
6. A brief comparison between the implied mass assembly of this study to results from the EAGLE simulation show a very similar qualitative trend. However the results from simulations imply a more rapid assembly of the outer regions.

2.8 Acknowledgments

The authors would like to thank the anonymous referee, as well as Matthew Ashby, and Joop Schaye for the helpful comments and discussion which greatly improved this paper. The research leading to these results has received funding from the European Research Council under the European Union's Seventh Framework Program (FP7/2007-2013)/ERC Grant agreement no. EGGS-278202. This work is based on data products from observations made with ESO Telescopes at the La Silla Paranal Observatory under ESO programme ID 179.A-2005 and on data products produced by TERAPIX and the Cambridge Astronomy Survey Unit on behalf of the UltraVISTA consortium. This work is also made possible by the observations taken by the 3D-HST Treasury Program (GO 12177 and 12328) with the NASA/ESA HST, which is operated by the Association of University for Research in Astronomy, Inc., under NASA contract NAS5-26555. DM acknowledges the support of the Research Corporation for Science Advancement's Cottrell Scholarship, and the National Science Foundation under Grant No. 1513473. KIC acknowledges funding from the European Research Council through the award of the Consolidator Grant ID 681627-BUILDUP. This research has made use of NASA's Astrophysics Data System.

2.9 Appendix

2.9.1 The effects of a fixed cumulative number density selection on the stellar surface mass density profiles

In this appendix, we briefly explore the effects of mass selection on the stellar surface mass density profiles. A key finding of this study is that the central ($r < 1 - 2$ kpc) stellar surface mass densities evolve more strongly than observed in earlier works (e.g., van Dokkum et al. 2010; Patel et al. 2013a; van Dokkum et al. 2014). It was suspected that this discrepancy was a result of the different number density selections (i.e. a fixed vs. evolving cumulative number density selection as discussed in Sec. 2.2.1), with a fixed number density selection yielding more massive progenitors (Fig. 3.1).

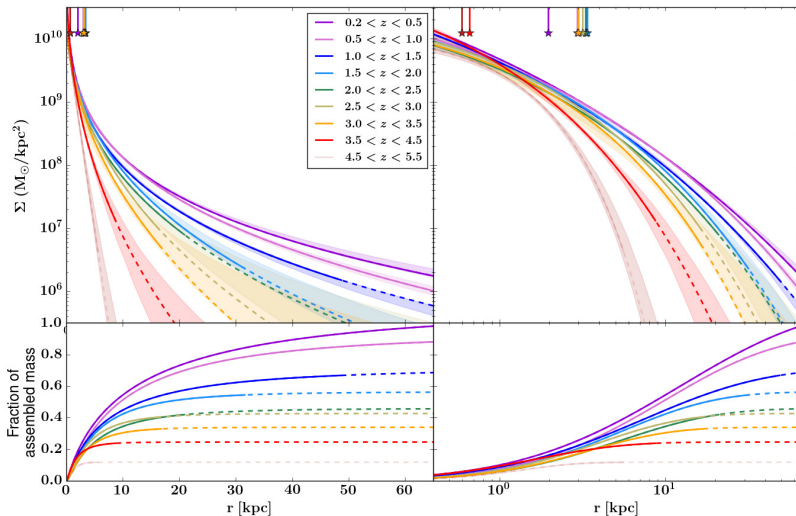


Figure 2.14 This figure is analogous to Fig. 2.9, with the profiles derived from stacks of galaxies using a fixed cumulative number density selection. In this figure, we see that the increase in the surface mass density within $1 - 2$ kpc observed in Fig. 2.9 largely disappears, and the inner profiles do not show strong evolution with redshift.

To properly investigate this, we repeated our analysis (as detailed in Sec. 2.5) for a fixed cumulative number density selected sample. In Fig. 2.14, we plot the resultant surface mass density profiles. A comparison of the right panels of Fig. 2.9 and Fig. 2.14 shows the new mass selection significantly alters the observed surface mass density profiles in the central regions. In Fig. 2.9, we see a difference of ≈ 1 dex between the lowest and highest redshift bin at $r < 2$ kpc. In contrast, the

inner profiles in Fig. 2.14 lie approximately on top of each other with most mass evolution occurring in the outskirts.

By choosing progenitors using the same methods as previous studies (e.g., van Dokkum et al. 2010; Patel et al. 2013a; van Dokkum et al. 2014), we recover their trends, i.e., there is very little redshift evolution in the central stellar surface mass densities and that most mass evolution is occurring in the outskirts ($r > 2$ kpc). The effect of selection on the evolution of surface mass-density profiles is two-fold. First, a fixed cumulative number density selection yields higher mass progenitors, which will tend to be more spheroidal, and more centrally concentrated. Secondly, for an evolving cumulative number density selection, the mass evolves more steeply, with less-massive progenitors at high redshift. This will mean the normalization of surface-mass density profiles will also evolve more steeply which is reflected in the evolution of the central stellar surface mass density (as seen in Fig. 2.9).

References

- Baldry, I. K., Driver, S. P., Loveday, J., et al. 2012, *MNRAS*, 421, 621
- Barro, G., Faber, S. M., Pérez-González, P. G., et al. 2013, *ApJ*, 765, 104
- . 2014, *ApJ*, 791, 52
- Barro, G., Kriek, M., Pérez-González, P. G., et al. 2016, *ApJL*, 827, L32
- Behroozi, P. S., Marchesini, D., Wechsler, R. H., et al. 2013, *ApJL*, 777, L10
- Bell, E. F., McIntosh, D. H., Katz, N., & Weinberg, M. D. 2003, *ApJS*, 149, 289
- Bell, E. F., van der Wel, A., Papovich, C., et al. 2012, *ApJ*, 753, 167
- Belli, S., Newman, A. B., & Ellis, R. S. 2014a, *ApJ*, 783, 117
- . 2015, *ApJ*, 799, 206
- Belli, S., Newman, A. B., Ellis, R. S., & Konidaris, N. P. 2014b, *ApJL*, 788, L29
- Bertin, E., & Arnouts, S. 1996, *A&AS*, 117, 393
- Bezanson, R., van Dokkum, P. G., Tal, T., et al. 2009, *ApJ*, 697, 1290
- Bezanson, R., van Dokkum, P. G., van de Sande, J., et al. 2013, *ApJL*, 779, L21
- Bezanson, R., van Dokkum, P. G., Franx, M., et al. 2011, *ApJL*, 737, L31
- Brammer, G. B., Whitaker, K. E., van Dokkum, P. G., et al. 2011, *ApJ*, 739, 24
- Brammer, G. B., van Dokkum, P. G., Franx, M., et al. 2012, *ApJS*, 200, 13
- Bruce, V. A., Dunlop, J. S., Cirasuolo, M., et al. 2012, *MNRAS*, 427, 1666
- Capak, P., Aussel, H., Bundy, K., et al. 2012, *SPLASH: Spitzer Large Area Survey with Hyper-Suprime-Cam*, Spitzer Proposal
- Cappellari, M., Emsellem, E., Krajnović, D., et al. 2011, *MNRAS*, 416, 1680
- Caputi, K. I., Cirasuolo, M., Dunlop, J. S., et al. 2011, *MNRAS*, 413, 162
- Caputi, K. I., Ilbert, O., Laigle, C., et al. 2015, *ApJ*, 810, 73
- Cassata, P., Giavalisco, M., Guo, Y., et al. 2011, *ApJ*, 743, 96
- Cimatti, A., Cassata, P., Pozzetti, L., et al. 2008, *A&A*, 482, 21
- Clauwens, B., Franx, M., & Schaye, J. 2016, *MNRAS*, 463, L1
- Cole, S., Norberg, P., Baugh, C. M., et al. 2001, *MNRAS*, 326, 255
- Conroy, C., Gunn, J. E., & White, M. 2009, *ApJ*, 699, 486
- Conselice, C. J., Blackburne, J. A., & Papovich, C. 2005, *ApJ*, 620, 564

REFERENCES

- Couto, G. S., Colina, L., López, J. P., Storchi-Bergmann, T., & Arribas, S. 2016, *A&A*, 594, A74
- Daddi, E., Renzini, A., Pirzkal, N., et al. 2005, *ApJ*, 626, 680
- Damjanov, I., McCarthy, P. J., Abraham, R. G., et al. 2009, *ApJ*, 695, 101
- Damjanov, I., Abraham, R. G., Glazebrook, K., et al. 2011, *ApJL*, 739, L44
- Davis, T. A., Young, L. M., Crocker, A. F., et al. 2014, *MNRAS*, 444, 3427
- Dekel, A., & Burkert, A. 2014, *MNRAS*, 438, 1870
- Duncan, K., Conselice, C. J., Mortlock, A., et al. 2014, *MNRAS*, 444, 2960
- Fiacconi, D., Madau, P., Potter, D., & Stadel, J. 2016a, *ApJ*, 824, 144
- Fiacconi, D., Mayer, L., Madau, P., et al. 2016b, *ArXiv e-prints*
- Fontana, A., Pozzetti, L., Donnarumma, I., et al. 2004, *A&A*, 424, 23
- Franx, M., van Dokkum, P. G., Förster Schreiber, N. M., et al. 2008, *ApJ*, 688, 770
- Freeman, K. C. 1970, *ApJ*, 160, 811
- Fumagalli, M., Patel, S. G., Franx, M., et al. 2012, *ApJL*, 757, L22
- Fumagalli, M., Labbé, I., Patel, S. G., et al. 2014, *ApJ*, 796, 35
- Furlong, M., Bower, R. G., Theuns, T., et al. 2015, *MNRAS*, 450, 4486
- Gallazzi, A., Charlot, S., Brinchmann, J., White, S. D. M., & Tremonti, C. A. 2005, *MNRAS*, 362, 41
- Grazian, A., Fontana, A., Santini, P., et al. 2015, *A&A*, 575, A96
- Grogin, N. A., Kocevski, D. D., Faber, S. M., et al. 2011, *ApJS*, 197, 35
- Hill, A. R., Muzzin, A., Franx, M., & van de Sande, J. 2016, *ApJ*, 819, 74
- Hilz, M., Naab, T., & Ostriker, J. P. 2013, *MNRAS*, 429, 2924
- Hopkins, P. F., Bundy, K., Hernquist, L., Wuyts, S., & Cox, T. J. 2010, *MNRAS*, 401, 1099
- Hopkins, P. F., Cox, T. J., Younger, J. D., & Hernquist, L. 2009, *ApJ*, 691, 1168
- Huertas-Company, M., Bernardi, M., Pérez-González, P. G., et al. 2016, *MNRAS*, 462, 4495
- Ilbert, O., McCracken, H. J., Le Fèvre, O., et al. 2013, *A&A*, 556, A55
- Kelvin, L. S., Driver, S. P., Robotham, A. S. G., et al. 2012, *MNRAS*, 421, 1007
- Kennicutt, Jr., R. C. 1998, *ApJ*, 498, 541
- Koekemoer, A. M., Faber, S. M., Ferguson, H. C., et al. 2011, *ApJS*, 197, 36
- Kriek, M., van der Wel, A., van Dokkum, P. G., Franx, M., & Illingworth, G. D. 2008, *ApJ*, 682, 896
- Kuntschner, H., Emsellem, E., Bacon, R., et al. 2010, *MNRAS*, 408, 97
- Labbé, I., Huang, J., Franx, M., et al. 2005, *ApJL*, 624, L81
- Lange, R., Driver, S. P., Robotham, A. S. G., et al. 2015, *MNRAS*, 447, 2603
- Lee, B., Giavalisco, M., Williams, C. C., et al. 2013, *ApJ*, 774, 47
- Leja, J., van Dokkum, P., & Franx, M. 2013, *ApJ*, 766, 33
- Madau, P., & Dickinson, M. 2014, *ARA&A*, 52, 415
- Man, A. W. S., Greve, T. R., Toft, S., et al. 2016, *ApJ*, 820, 11
- Marchesini, D., van Dokkum, P. G., Förster Schreiber, N. M., et al. 2009, *ApJ*, 701, 1765
- Marchesini, D., Muzzin, A., Stefanon, M., et al. 2014, *ApJ*, 794, 65
- Margalef-Bentabol, B., Conselice, C. J., Mortlock, A., et al. 2016, *MNRAS*, 461, 2728

- McCracken, H. J., Milvang-Jensen, B., Dunlop, J., et al. 2012, *A&A*, 544, A156
- McDermid, R. M., Alatalo, K., Blitz, L., et al. 2015, *MNRAS*, 448, 3484
- McLure, R. J., Pearce, H. J., Dunlop, J. S., et al. 2013, *MNRAS*, 428, 1088
- Milvang-Jensen, B., Freudling, W., Zabl, J., et al. 2013, *A&A*, 560, A94
- Momcheva, I. G., Brammer, G. B., van Dokkum, P. G., et al. 2016, *ApJS*, 225, 27
- Morishita, T., Ichikawa, T., Noguchi, M., et al. 2015, *ApJ*, 805, 34
- Mortlock, A., Conselice, C. J., Hartley, W. G., et al. 2013, *MNRAS*, 433, 1185
- . 2015, *MNRAS*, 447, 2
- Mosleh, M., Williams, R. J., Franx, M., & Kriek, M. 2011, *ApJ*, 727, 5
- Moustakas, J., Coil, A. L., Aird, J., et al. 2013, *ApJ*, 767, 50
- Muzzin, A., Labbé, I., Franx, M., et al. 2012, *ApJ*, 761, 142
- Muzzin, A., Marchesini, D., Stefanon, M., et al. 2013a, *ApJS*, 206, 8
- . 2013b, *ApJ*, 777, 18
- Naab, T., Johansson, P. H., & Ostriker, J. P. 2009, *ApJL*, 699, L178
- Nelson, E. J., van Dokkum, P. G., Förster Schreiber, N. M., et al. 2016, *ApJ*, 828, 27
- Newman, A. B., Belli, S., & Ellis, R. S. 2015, *ApJL*, 813, L7
- Newman, A. B., Ellis, R. S., Bundy, K., & Treu, T. 2012, *ApJ*, 746, 162
- Newman, A. B., Ellis, R. S., Treu, T., & Bundy, K. 2010, *ApJL*, 717, L103
- Oser, L., Naab, T., Ostriker, J. P., & Johansson, P. H. 2012, *ApJ*, 744, 63
- Ownsworth, J. R., Conselice, C. J., Mortlock, A., et al. 2014, *MNRAS*, 445, 2198
- Ownsworth, J. R., Conselice, C. J., Mortlock, A., Hartley, W. G., & Buitrago, F. 2012, *MNRAS*, 426, 764
- Ownsworth, J. R., Conselice, C. J., Mundy, C. J., et al. 2016, *MNRAS*, 461, 1112
- Papovich, C., Finkelstein, S. L., Ferguson, H. C., Lotz, J. M., & Giavalisco, M. 2011, *MNRAS*, 412, 1123
- Papovich, C., Moustakas, L. A., Dickinson, M., et al. 2006, *ApJ*, 640, 92
- Patel, S. G., Holden, B. P., Kelson, D. D., et al. 2012, *ApJL*, 748, L27
- Patel, S. G., van Dokkum, P. G., Franx, M., et al. 2013, *ApJ*, 766, 15
- Peng, C. Y., Ho, L. C., Impey, C. D., & Rix, H.-W. 2010, *AJ*, 139, 2097
- Schaye, J., Crain, R. A., Bower, R. G., et al. 2015, *MNRAS*, 446, 521
- Schreiber, C., Pannella, M., Elbaz, D., et al. 2015, *A&A*, 575, A74
- Sersic, J. L. 1968, *Atlas de galaxias australes*
- Shen, S., Mo, H. J., White, S. D. M., et al. 2003, *MNRAS*, 343, 978
- Skelton, R. E., Whitaker, K. E., Momcheva, I. G., et al. 2014, *ApJS*, 214, 24
- Snyder, G. F., Torrey, P., Lotz, J. M., et al. 2015, *MNRAS*, 454, 1886
- Somerville, R. S., & Davé, R. 2015, *ARA&A*, 53, 51
- Stefanon, M., Marchesini, D., Rudnick, G. H., Brammer, G. B., & Whitaker, K. E. 2013, *ApJ*, 768, 92
- Stefanon, M., Marchesini, D., Muzzin, A., et al. 2015, *ApJ*, 803, 11
- Straatman, C. M. S., Labbé, I., Spitler, L. R., et al. 2015, *ApJL*, 808, L29
- Swinbank, A. M., Smail, I., Chapman, S. C., et al. 2010, *MNRAS*, 405, 234
- Szomoru, D., Franx, M., & van Dokkum, P. G. 2012, *ApJ*, 749, 121
- Szomoru, D., Franx, M., van Dokkum, P. G., et al. 2013, *ApJ*, 763, 73
- . 2010, *ApJL*, 714, L244

REFERENCES

- Thomas, D., Maraston, C., Bender, R., & Mendes de Oliveira, C. 2005, *ApJ*, 621, 673
- Thomas, D., Maraston, C., Schawinski, K., Sarzi, M., & Silk, J. 2010, *MNRAS*, 404, 1775
- Toft, S., Gallazzi, A., Zirm, A., et al. 2012, *ApJ*, 754, 3
- Toft, S., van Dokkum, P., Franx, M., et al. 2007, *ApJ*, 671, 285
- Toft, S., Smolčić, V., Magnelli, B., et al. 2014, *ApJ*, 782, 68
- Tomczak, A. R., Quadri, R. F., Tran, K.-V. H., et al. 2014, *ApJ*, 783, 85
- . 2016, *ApJ*, 817, 118
- Torrey, P., Wellons, S., Machado, F., et al. 2015, *MNRAS*, 454, 2770
- Trujillo, I., Ferreras, I., & de La Rosa, I. G. 2011, *MNRAS*, 415, 3903
- Trujillo, I., Förster Schreiber, N. M., Rudnick, G., et al. 2006, *ApJ*, 650, 18
- van de Sande, J., Kriek, M., Franx, M., Bezanson, R., & van Dokkum, P. G. 2015, *ApJ*, 799, 125
- van de Sande, J., Kriek, M., Franx, M., et al. 2011, *ApJL*, 736, L9
- . 2013, *ApJ*, 771, 85
- van der Wel, A., Rix, H.-W., Wuyts, S., et al. 2011, *ApJ*, 730, 38
- van der Wel, A., Franx, M., van Dokkum, P. G., et al. 2014, *ApJ*, 788, 28
- van Dokkum, P. G., Franx, M., Kriek, M., et al. 2008, *ApJL*, 677, L5
- van Dokkum, P. G., Whitaker, K. E., Brammer, G., et al. 2010, *ApJ*, 709, 1018
- van Dokkum, P. G., Brammer, G., Fumagalli, M., et al. 2011, *ApJL*, 743, L15
- van Dokkum, P. G., Leja, J., Nelson, E. J., et al. 2013, *ApJL*, 771, L35
- van Dokkum, P. G., Bezanson, R., van der Wel, A., et al. 2014, *ApJ*, 791, 45
- van Dokkum, P. G., Nelson, E. J., Franx, M., et al. 2015, *ApJ*, 813, 23
- Vogelsberger, M., Genel, S., Springel, V., et al. 2014, *MNRAS*, 444, 1518
- Vulcani, B., Marchesini, D., De Lucia, G., et al. 2016, *ApJ*, 816, 86
- Wellons, S., & Torrey, P. 2016, *ArXiv e-prints*
- Wellons, S., Torrey, P., Ma, C.-P., et al. 2015, *MNRAS*, 449, 361
- Whitaker, K. E., Kriek, M., van Dokkum, P. G., et al. 2012, *ApJ*, 745, 179
- Whitaker, K. E., Labbé, I., van Dokkum, P. G., et al. 2011, *ApJ*, 735, 86
- Whitaker, K. E., Bezanson, R., van Dokkum, P. G., et al. 2016, *ArXiv e-prints*
- Williams, C. C., Gialalisco, M., Cassata, P., et al. 2014, *ApJ*, 780, 1
- Williams, R. J., Quadri, R. F., Franx, M., van Dokkum, P., & Labbé, I. 2009, *ApJ*, 691, 1879
- Williams, R. J., Quadri, R. F., Franx, M., et al. 2010, *ApJ*, 713, 738
- Wuyts, S., Förster Schreiber, N. M., van der Wel, A., et al. 2011, *ApJ*, 742, 96
- Yano, M., Kriek, M., van der Wel, A., & Whitaker, K. E. 2016, *ApJL*, 817, L21

THE MASS GROWTH AND STELLAR AGES OF GALAXIES: OBSERVATIONS VERSUS SIMULATIONS

Using observed stellar mass functions out to $z = 5$, we measure the main progenitor stellar mass growth of descendant galaxies with masses of $\log M_*/M_\odot = 11.5, 11.0, 10.5, 10.0$ at $z \sim 0.1$ using an evolving cumulative number density selection. From these mass growth histories, we are able to measure the time at which half the total stellar mass of the descendant galaxy was assembled, t_a , which, in order of decreasing mass corresponds to redshifts of $z_a = 1.28, 0.92, 0.60$ and 0.51 . We compare this to the median light-weighted stellar age t_* ($z_* = 2.08, 1.49, 0.82$ and 0.37) of a sample of low redshift SDSS galaxies (from the literature) and find the timescales are consistent with more massive galaxies forming a higher fraction of their stars ex-situ compared to lower mass descendants. We find that both t_* and t_a strongly correlate with mass which is in contrast to what is found in the EAGLE hydrodynamical simulation which shows a flat relationship between t_a and M_* . However, the semi-analytic model of Henriques et al. (2015) is consistent with the observations in both t_a and t_* with M_* , showing the most recent semi-analytic models are better able to decouple the evolution of the baryons from the dark matter in lower-mass galaxies.

Allison R. Hill, Adam Muzzin, Marijn Franx, and Danilo Marchesini
The Astrophysical Journal Letters
Volume 849, Issue 2, pp. L26 (2017)

3.1 Introduction

Inferring the assembly history of present-day galaxies is challenging. It requires accurately linking progenitor to descendant, a process which is obfuscated by the fact that we only ever observe a galaxy at one snapshot in time. However, by using mass-complete censuses of galaxies at different redshifts and observing how populations of galaxies move through various parameter spaces (i.e., SFR, sSFR, central surface mass density, central stellar velocity dispersion, number density, etc.), one can begin to connect descendant galaxies to their likely progenitor population.

By tracing galaxy evolution using a variety of the aforementioned parameters, observational studies are united in the finding that massive galaxies assemble most of their stellar mass before low mass galaxies, indicative of baryonic 'down-sizing' (e.g., Pérez-González et al. 2008; Marchesini et al. 2009; Behroozi et al. 2013; Muzzin et al. 2013b; González Delgado et al. 2017). This is consistent with analyses of the stellar populations of local galaxies, which find that more massive galaxies are host to older stellar populations (e.g., Kauffmann et al. 2003; Gallazzi et al. 2005; Thomas et al. 2010)

In contrast to observations, semi-analytic models (SAMs) and hydrodynamical simulations do not share the same consistency. Although both hydrodynamical simulations and semi-analytic models reproduce the positive correlation of stellar age with stellar mass, they differ in their predictions for when that mass assembled. Recent SAMs predict massive galaxies forming earlier than their low mass counterparts (e.g., Henriques et al. 2015), in contrast to recent hydrodynamical simulations who show either a flat relationship between assembly time (the time at which 50% of the mass was assembled) and stellar mass (Qu et al. 2017), or a weak positive correlation (Sparre et al. 2015).

Although these models are inconsistent with each other on trends of stellar mass with assembly, they do all predict a higher fraction of the stars in massive galaxies were formed ex-situ (e.g., Rodriguez-Gomez et al. 2016; Qu et al. 2017; Mundy et al. 2017). This picture is consistent with observations that indicate mergers are an important avenue of mass growth in massive galaxies since $z \sim 1$ (e.g., Newman et al. 2012; Hill et al. 2017). However, the role of mergers in the mass growth of lower mass galaxies remains uncertain.

In this Letter, we endeavour to draw a direct observational comparison between the assembly time and the mass-weighted stellar age of galaxies, and demonstrate more concretely the relationship between galaxy stellar mass and the fraction of ex-situ stars. We also compare these timescales to the EAGLE simulation as well as the recent SAM of Henriques et al. (2015) (hereafter H2015).

Unless otherwise specified, all ages and assembly times are for galaxies corresponding to a references redshift of $z = 0.1$, with all ages reported in lookback times. We assume a Λ -CDM cosmology ($H_0 = 70 \text{ kms}^{-1}\text{Mpc}^{-1}$, $\Omega_M = 0.3$, and $\Omega_\Lambda = 0.7$).

3.2 Analysis

3.2.1 Measuring the assembly times

To estimate the assembly time (t_a) for a galaxy, we must first determine a mass assembly history. The first challenge to analyzing the mass evolution of present day galaxies is properly identifying their progenitors. There are several methods to do this, e.g., by inferring the mass growth from the evolution of the SFR-mass relation (e.g. Patel et al. 2013b), selection via central surface-mass density (e.g. van Dokkum et al. 2014), selection via fixed central velocity dispersion (e.g., Bezanson et al. 2012), and the evolution of the stellar mass function (e.g., Pérez-González et al. 2008; Marchesini et al. 2009; Muzzin et al. 2013b) (among others). The simplest and most appropriate method to derive the progenitor masses of galaxies is through cumulative number density selection. This method begins with the simple assumption that cumulative density would remain constant if there were no mergers or scatter in assembly; the evolution in the cumulative density due to these effects can be predicted robustly from models (Behroozi et al. 2013). These predictions have been tested and verified against more detailed simulations which accurately recover the median mass evolution (e.g., Torrey et al. 2015; Clauwens et al. 2016; Wellons & Torrey 2016). This method is the only method which can give a fair estimate from the evolution of the mass function alone, i.e., it does not need any detailed modelling to the full $f(M_*, SFR, \text{merger rate})$ distribution of galaxies.

In Figure 3.1 we show the number density, and progenitor mass evolution for four different descendant masses of $\log M_*/M_\odot = 11.5, 11.0, 10.5, 10.0$ at $z \sim 0.1$. As in Hill et al. (2017), we utilize the mass functions of Muzzin et al. (2013b), Grazian et al. (2015) (with the addition of Bernardi et al. 2017 to extend to $z \sim 0.1$) to translate the number densities from Behroozi et al. (2013) into galaxy stellar masses as a function of redshift (left panel, Figure 3.1). The regular evolution of the implied progenitor mass as a function of redshift in the right-panel highlights the quality of the input mass functions. Also indicated in the right panel of Figure 3.1 are the assembly times, t_a , the points at which half the final stellar masses were assembled. For our progenitors selection, this corresponds to an assembly redshifts (in order of decreasing stellar mass) of $z_a = 1.28, 0.92, 0.60, 0.51$. In this plot we see a clear trend towards baryonic cosmic ‘down-sizing’, with the most massive galaxies assembling half their stellar mass earlier.

3.2.2 Measuring the stellar ages

To compare t_a to the present-day age of the stellar populations in those galaxies, t_* , we take the light-weighted ages from Gallazzi et al. (2005) ($t_{*,LW}$) which were measured from a subsample of 44 254 SDSS galaxy spectra. This subsample was chosen such that the median S/N per pixel was greater than 20, in order to accurately, and simultaneously model both the age and metal sensitive spectral indices such as $H\beta, H\delta_A, H\gamma_A, D4000$, and $[Mg_2Fe]$. They also were careful to exclude galaxies at redshifts which deviated substantially from the Hubble flow, resulting in a redshift range of $0.005 < z < 0.22$, with a median redshift of $z = 0.13$. Extensive

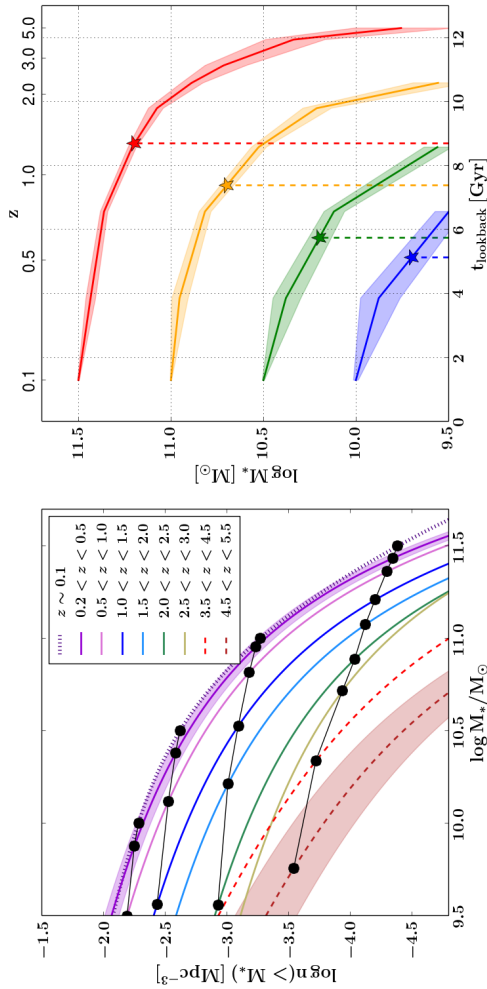


Figure 3.1 *Left*: The cumulative number-density as a function of stellar mass at different z . Solid, dashed and dotted lines indicate the mass functions of Muzzin et al. (2013b), Grazian et al. (2015), and Bernardi et al. (2017) respectively, with colour indicating the redshift. Uncertainties in the mass functions take into consideration the uncertainties in the photo- z 's, SFH and cosmic variance. For clarity, only the uncertainties for the highest- and lowest- z are shown (as the uncertainties monotonically increase with z). Black circles indicate the cumulative number density selection of Behroozi et al. (2013) for four different descendant masses at $z \sim 0.1$ ($\log M_*/M_\odot = 11.5, 11.0, 10.5, 10.0$). *Right*: The corresponding mass evolution of the descendants considered in the left panel. Shaded regions indicate the uncertainty in the progenitor mass from the uncertainties in the mass functions. We trace the progenitors of four different descendant masses at $z \sim 0.1$. Also plotted are the assembly times (t_{assembly} ; coloured stars), which are the times at which half the final descendant mass is assembled.

and careful modelling, using a library of 150 000 Monte Carlo realizations which cover a wide parameter space of plausible star formation histories, were used to accurately determine both age and metallicity as well as quantify the magnitude of the errors on these derived quantities. A full description of their methods can be found in Gallazzi et al. (2005).

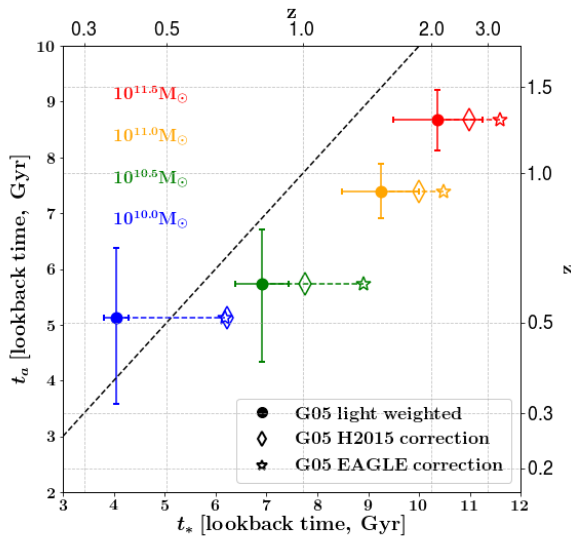


Figure 3.2 The assembly age, t_a , plotted as a function of the stellar age, t_* . t_a is defined as the age at which half the stellar mass was assembled, as determined from the stellar-mass evolution tracks in the right panel of Figure 3.1, with the errors estimated from uncertainties from the stellar mass functions. The stellar ages are the median light-weighted ages (filled-circles) taken from Gallazzi et al. (2005), with the errors representing the expected uncertainty resulting from age gradients (see text for details). We have also estimated a mass-weighted age correction to the light-weighted ages using corrections measured from both EAGLE and H2015 (details can be found in the main text). We see a positive correlation between t_* , t_a and mass, with the most massive galaxies assembling first.

For a galaxy with a given M_* , we take the median $t_{*,LW}$ (see Table 2 in Gallazzi et al. 2005). As $t_{*,LW}$ is a median value, the formal errors are small (fractions of a percentage point), so we do not include those errors. However, as the SDSS fibres impose an aperture, there is potential for errors resulting from age gradients, especially in the larger galaxies. A recent analysis of age gradients in SDSS galaxies by Goddard et al. (2017) found gradients at a level of $\sim 0.1 \text{ dex}/R_e$ from the centre to $1.5R_e$. This translates to an aperture correction of approximately 10%, which we use as a conservative error estimate in the median $t_{*,LW}$.

Light-weighted ages are biased towards younger stellar populations, as young

stars dominate the optical emission where many age sensitive indices are measured (see Kauffmann et al. 2003). A more representative t_* metric is the mass-weighted age, $t_{*,MW}$. Since the SFH is not known for these galaxies, we generate stellar-mass dependent corrections to $t_{*,MW}$ using the differences between the mass-weighted ages and r-band weighted ages from both H2015 (available in their catalog) and EAGLE (James Trayford, private communication) and apply it in the following way:

$$t_{*,MW,G05} = t_{*,LW,G05} + (t_{*,MW,sims} - t_{*,LW,sims}) \quad (3.1)$$

Figure 3.2 shows t_a , $t_{*,MW,G05}$ for both H2015 and EAGLE, and $t_{*,LW,G05}$ for all of our descendant galaxy masses. We see a range of assembly times, from ~ 5 Gyr at the low-mass end, to almost 9 Gyr for our highest mass bin. The span is larger in t_* where we see a range of $\sim 5 - 11$ Gyr. We see all values are consistent with $t_a < t_{*,MW}$ which confirms our results are physical. We observe $t_* - t_a$ increasing with stellar mass, which suggests a higher fraction of the stars in massive galaxies are formed ex-situ than at lower masses. When comparing $t_* - t_a$ to the ex-situ fractions of the H2015 SAMs, they imply an ex-situ fraction of between 3–33% for $\log M_* \geq 10.5$ and between 1–33% for $\log M_* = 10.0$. This finding is consistent with other observational studies (e.g, most recently, Rodríguez-Puebla et al. 2017, who use sub-halo abundance matching to find a $M_* \sim 5 \times 10^{11} M_\odot$ galaxy has $\sim 36\%$ of their mass formed ex-situ compared to only $\sim 2.4\%$ for Milky-Way mass galaxies). This trend is also seen simulations (see Sec. 5.1 and references therein).

3.2.3 Comparison to Simulations

In Figure 3.3, we compare our assembly times, and the stellar ages of Gallazzi et al. (2005) to the median values of those found in the EAGLE simulation (Schaye et al. 2015), and the SAM of H2015 as a function of stellar mass. In this figure, we record the median r-band weighted stellar age of a narrow stellar mass range ($\Delta \log M_*/M_\odot = 0.05$) of galaxies from the largest EAGLE simulation (Ref-L100N1504) at $z = 0.1$, and the millennium simulation (Henriques2015a..MRscPlanck1). We also trace the mass evolution of the most massive progenitors of these galaxies to estimate an assembly redshift.

Figure 3.3 shows that the observations display a positive correlation between t_* , t_a and stellar mass (as implied by the mass functions), assuming the relationships are of the form

$$t_* \propto \alpha \log M_*, \quad t_a \propto \beta \log M_* \quad (3.2)$$

where α and β are the best fit linear slopes for t_* and t_a respectively. The H2015 model also reproduces the positive trend between stellar mass, t_* and t_a , albeit with slightly flatter slopes. For observations, we find $\alpha_{obs} = 4.25 \pm 0.55$, and $\beta_{obs} = 2.46 \pm 0.30$ which are both steeper than the those implied for H2015 ($\alpha_{H2015} = 3.42 \pm 0.56$, $\beta_{H2015} = 1.38 \pm 0.34$) although they agree to within 2σ . This suggests the SAMs are doing a good job at reproducing the formation of stars and

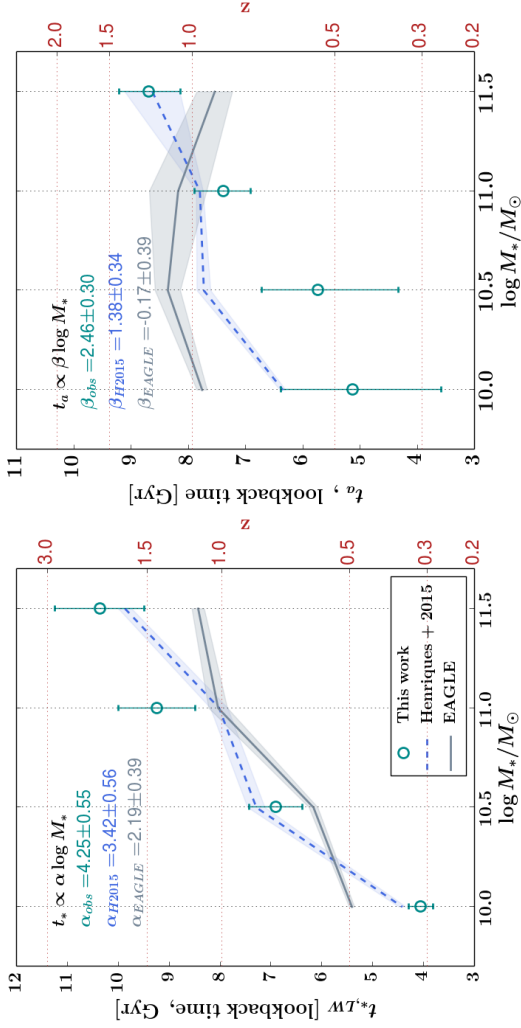


Figure 3.3 The stellar age (t_* ; left panel) and assembly age (t_a ; right panel) plotted as function of their final stellar masses. The turquoise circles are the values determined from observations (as in Figure 3.2), solid grey lines are median values from the EAGLE simulation Ref-L100N1504, and dashed blue lines are from H2015. with the shaded regions around these lines representing the error implied from bootstrapping the samples. We see the same positive correlation between t_* and M_* , with H2015 better matching (to within 2σ) the steep dependence than EAGLE, which has a flatter relationship than the observations imply. In the right panel, we see the same flat relationship between M_* and t_a in EAGLE as found in Qu et al. (2017) which does not match the observations, and is in fact consistent with a slope of 0. The t_a measured from H2015 are in good agreement with the observations (to within 2σ).

their assembly for the stellar mass ranges considered in this study, with a slight bias towards earlier formation.

The EAGLE simulation similarly reproduces the relationship between t_* and M_* , although the value for α is even flatter than that of H2015 ($\alpha_{EAGLE} = 2.19 \pm 0.39$). For the assembly time, EAGLE does not reproduce the trend at all, and instead has a β consistent with 0 ($\beta_{EAGLE} = -0.17 \pm 0.40$). This is also seen in Qu et al. (2017), who performed a more robust analysis of the EAGLE simulation galaxy assembly, and who's median assembly times also indicate a flat relationship with M_* .

At high masses ($M_* = 10^{11.5} M_\odot$), compared to observations, massive EAGLE galaxies assemble their mass too quickly. There are also issues at the lowest mass where the discrepancy of stellar ages and assembly times in EAGLE at $\log M_*/M_\odot = 10.0$ is significant (and also present in H2015, although not as discrepant in the SAM) and likely related to simulations over-producing low-mass galaxies at higher redshift (see Weinmann et al. 2012; Henriques et al. 2013; Lacey et al. 2016).

3.3 Discussions and Conclusions

From Figure 3.1 and 3.2, we see a clear trend between t_a and t_* with stellar mass. More massive galaxies formed earlier, and at $\log M_*/M_\odot \geq 10.5$, they also have stellar ages which are older than their respective assembly times, suggesting that a larger fraction of their stars formed ex-situ compared to lower mass galaxies. This picture implies that mergers are a more important component of stellar mass growth in massive galaxies, which is consistent with what is seen in previous studies (e.g., Naab et al. 2009; Hopkins et al. 2010; van Dokkum et al. 2010; Trujillo et al. 2011; Newman et al. 2012; Hilz et al. 2013; McLure et al. 2013; Vulcani et al. 2016; Hill et al. 2017; Mundy et al. 2017). In contrast, with $t_a \approx t_*$ for galaxies at $\log M_*/M_\odot < 10.5$, almost all the stars can be attributed to in-situ formation.

Although the t_a was not calculated explicitly, both Patel et al. (2013a) and van Dokkum et al. (2013) used fixed cumulative number density arguments to calculate the stellar mass evolution as a function of redshift, from which a z_a can be inferred. Using their fits for $M_*(z)$, for a $10^{11.2} M_\odot$ galaxy, Patel et al. (2013a) found an assembly redshift of 1.97. Using our prescription, for the same galaxy mass, we would find $z_a = 1.42$. van Dokkum et al. (2013), for a $10^{10.7} M_\odot$ galaxy, find $z_a = 1.35$ (and for which we would find $z_a = 0.91$). Both studies find earlier assembly redshifts than we do. About half this redshift discrepancy is due different selection criteria (i.e. the use of a fixed cumulative number density instead of an evolving cumulative number density, where the former predicts higher mass progenitors (see Hill et al. 2017), with the remainder due to the use of different mass functions.

A comparison of our results to recent hydrodynamical simulations (Schaye et al. 2015) and semi-analytic models (H2015) show good agreement in the relationship of t_* with stellar mass in all but the lowest mass bin (with the exception of the highest mass bin in the EAGLE simulation). This is especially impressive in EAGLE considering the models were not calibrated to reproduce stellar ages.

The disagreement in t_* in the lowest mass bin suggests either simulations are still forming stars too early, or, conversely the stellar ages in lower mass galaxies are underestimated. Using deep ($S/N(\text{\AA}) > 50$) spectroscopy of a handful of local group galaxies, Sánchez-Blázquez et al. (2011) found that nearby barred-spiral galaxies were dominated by stars with ages on the order of ~ 10 Gyr. Using deep, color-magnitude diagrams of local dwarfs, Hidalgo et al. (2013) also found that the majority of stars in local dwarfs are between 9 – 10 Gyr old. This is in apparent contradiction to the median ages found by Gallazzi et al. (2005). It is possible that the smaller local samples are not representative of the population as a whole. Conversely, the reverse could also be true and that the low-mass end of the galaxies from Gallazzi et al. (2005) are also not representative. Alternatively, one way to resolve the discrepancy is to assume that there is a positive relation between stellar mass and age, which has a turnover at dwarf-galaxy stellar masses (although this seems unlikely). A more robust survey of low-mass, and hence low-surface brightness galaxies would be needed to address these issues.

If we assume that the mass-weighted stellar ages inferred from Gallazzi et al. (2005) are correct, then the disagreement between observations and EAGLE of t_* also folds into the assembly times, where we see more significant disagreement between EAGLE and our estimates (although with large scatter). EAGLE does not reproduce the positive correlation between t_a and stellar mass, but instead predicts a flat relationship which might be related to the fact that EAGLE doesn't reproduce the GSMF (Furlong et al. 2015).

Considering the SAMs of a decade ago (e.g., De Lucia et al. 2006), there has been massive improvement, with the assembly times calculated from the most recent SAM (H2015) agreeing remarkably well with the observations (to within 2σ), with a slight bias to early assembly times. Although there have been great improvements in recent modelling and simulation work in regards to reproducing the GSMF, these results suggests that there are potential systematic offsets which need to be addressed, and that the evolution of the baryonic component of low-mass galaxies has not been sufficiently decoupled from their host dark-matter halos. Observationally, there is an under-explored parameter space in regards to low-mass galaxies which are crucially needed to inform the simulations.

3.4 Summary

In this Letter, we have measured the assembly time, and stellar ages from observations for four different mass descendant galaxies ($\log M_*/M_\odot = 11.5, 11.0, 10.5, 10.0$) at $z \sim 0.1$ and find

1. The assembly times, and stellar ages decrease with decreasing stellar mass, consistent with cosmic 'down-sizing'.
2. The difference between t_a and t_* increases weakly with increasing stellar mass suggesting that massive galaxies form a larger fraction of their stars ex-situ compared to lower mass galaxies.

3. t_a and t_* both increase with stellar mass, ranging from $\sim 5 - 11$ Gyr in mass-weighted stellar age and $\sim 5 - 9$ Gyr in assembly times. The SAM model of H2015 reproduces these trends to within 2σ , albeit with slightly flatter relationships. EAGLE reproduces the positive correlation with t_* , but not with t_a where EAGLE predicts no mass dependence on assembly times.
4. The assembly times and stellar ages from the most recent SAM from the Millennium simulations (Henriques et al. 2015) are in good agreement with the observations, with a slight bias to earlier formation and assembly.

3.5 Acknowledgments

We would like to thank Bruno Henriques, and James Trayford for deriving values from the H2015 and EAGLE catalogs, respectively. We are also grateful to Pieter van Dokkum and the anonymous referee whose comments greatly improved the presentation of this work. DM acknowledges the National Science Foundation under grant No. 1513473. This research has made use of NASA's Astrophysics Data System.

References

- Behroozi, P. S., Marchesini, D., Wechsler, R. H., et al. 2013, *ApJL*, 777, L10
Bernardi, M., Meert, A., Sheth, R. K., et al. 2017, *MNRAS*, 467, 2217
Bezanson, R., van Dokkum, P., & Franx, M. 2012, *ApJ*, 760, 62
Clauwens, B., Franx, M., & Schaye, J. 2016, *MNRAS*, 463, L1
De Lucia, G., Springel, V., White, S. D. M., Croton, D., & Kauffmann, G. 2006, *MNRAS*, 366, 499
Furlong, M., Bower, R. G., Theuns, T., et al. 2015, *MNRAS*, 450, 4486
Gallazzi, A., Charlot, S., Brinchmann, J., White, S. D. M., & Tremonti, C. A. 2005, *MNRAS*, 362, 41
Goddard, D., Thomas, D., Maraston, C., White, et al. 2017, *MNRAS*, 466, 4731
González Delgado, R. M., Pérez, E., Cid Fernandes, R., et al. 2017, *ArXiv e-prints*
Grazian, A., Fontana, A., Santini, P., et al. 2015, *A&A*, 575, A96
Henriques, B. M. B., White, S. D. M., Thomas, P. A., et al. 2015, *MNRAS*, 451, 2663
—. 2013, *MNRAS*, 431, 3373
Hidalgo, S. L., Monelli, M., Aparicio, A., et al. 2013, *ApJ*, 778, 103
Hill, A. R., Muzzin, A., Franx, M., et al. 2017, *ApJ*, 837, 147
Hilz, M., Naab, T., & Ostriker, J. P. 2013, *MNRAS*, 429, 2924
Hopkins, P. F., Bundy, K., Hernquist, L., Wuyts, S., & Cox, T. J. 2010, *MNRAS*, 401, 1099
Kauffmann, G., Heckman, T. M., White, S. D. M., et al. 2003, *MNRAS*, 341, 33
Lacey, C. G., Baugh, C. M., Frenk, C. S., et al. 2016, *MNRAS*, 462, 3854
Marchesini, D., van Dokkum, P. G., Förster Schreiber, N. M., et al. 2009, *ApJ*, 701, 1765

-
- McLure, R. J., Pearce, H. J., Dunlop, J. S., et al. 2013, *MNRAS*, 428, 1088
- Mundy, C. J., Conselice, C. J., Duncan, K. J., et al. 2017, *ArXiv e-prints*
- Muzzin, A., Marchesini, D., Stefanon, M., et al. 2013, *ApJ*, 777, 18
- Naab, T., Johansson, P. H., & Ostriker, J. P. 2009, *ApJL*, 699, L178
- Newman, A. B., Ellis, R. S., Bundy, K., & Treu, T. 2012, *ApJ*, 746, 162
- Patel, S. G., van Dokkum, P. G., Franx, M., et al. 2013a, *ApJ*, 766, 15
- Patel, S. G., Fumagalli, M., Franx, M., et al. 2013b, *ApJ*, 778, 115
- Pérez-González, P. G., Rieke, G. H., Villar, V., et al. 2008, *ApJ*, 675, 234
- Qu, Y., Helly, J. C., Bower, R. G., et al. 2017, *MNRAS*, 464, 1659
- Rodríguez-Gomez, V., Pillepich, A., Sales, L. V., et al. 2016, *MNRAS*, 458, 2371
- Rodríguez-Puebla, A., Primack, J. R., Avila-Reese, V., & Faber, S. M. 2017, *MNRAS*, 470, 651
- Sánchez-Blázquez, P., Ocvirk, P., Gibson, B. K., Pérez, I., & Peletier, R. F. 2011, *MNRAS*, 415, 709
- Schaye, J., Crain, R. A., Bower, R. G., et al. 2015, *MNRAS*, 446, 521
- Sparre, M., Hayward, C. C., Springel, V., et al. 2015, *MNRAS*, 447, 3548
- Thomas, D., Maraston, C., Schawinski, K., Sarzi, M., & Silk, J. 2010, *MNRAS*, 404, 1775
- Torrey, P., Wellons, S., Machado, F., et al. 2015, *MNRAS*, 454, 2770
- Trujillo, I., Ferreras, I., & de La Rosa, I. G. 2011, *MNRAS*, 415, 3903
- van Dokkum, P. G., Whitaker, K. E., Brammer, G., et al. 2010, *ApJ*, 709, 1018
- van Dokkum, P. G., Leja, J., Nelson, E. J., et al. 2013, *ApJL*, 771, L35
- van Dokkum, P. G., Bezanson, R., van der Wel, A., et al. 2014, *ApJ*, 791, 45
- Vulcani, B., Marchesini, D., De Lucia, G., et al. 2016, *ApJ*, 816, 86
- Weinmann, S. M., Pasquali, A., Oppenheimer, B. D., et al. 2012, *MNRAS*, 426, 2797
- Wellons, S., & Torrey, P. 2016, *ArXiv e-prints*

Chapter 4

THE EVOLUTION OF GALAXY FLATTENING AT $z < 4$ IN CANDELS

We investigate the median flattening of galaxies at $0.2 < z < 4.0$ in all five CANDELS fields via the apparent axis ratio q . Massive quiescent and star-forming galaxies have similar median q (q_{med}) values at $z > 2.5$, consistent with the formation of quiescent galaxies through wet mergers and/or transitions from star-forming to quiescent without structural transformation. At lower redshifts, quiescent galaxies are rounder than star-forming galaxies of the same stellar mass (M_*). The evolution in q_{med} and the correlations between q and M_* coincide with changes in the sérsic index (n): rounder galaxies on average have higher n . For star-forming galaxies there is a strong additional dependence on galaxy size: galaxies with small r_e are rounder than galaxies with large r_e , even after removing the trend with n . While keeping in mind that attenuation by dust may affect the measurements of structural parameters, in particular for edge-on (flat) galaxies, our findings suggest that the evolution in q_{med} generally traces bulge evolution for both the star-forming and the quiescent population. For star-forming galaxies we are witnessing the initial formation and growth of bulges, while for quiescent galaxies we are witnessing the progressive destruction of pre-existing disks through (dry) merging.

Allison R. Hill, Arjen van der Wel, Marijn Franx, Adam Muzzin
in prep

4.1 Introduction

Tracing the morphological evolution of galaxies from photometry is valuable in providing insights into the underlying kinematics of galaxy evolution when time-expensive, high S/N spectra are unavailable. Physical parameters have been long known to be broadly couple to Hubble-type (e.g., Roberts & Haynes 1994; Blanton et al. 2003), with young, star forming (SF) galaxies exhibiting some form of gas-rich disk or flattened structure and quiescent (Q) galaxies exhibiting older stellar populations in rounder, puffed up ellipticals (although passive disks do make up a small, but not insignificant population of passive galaxies; Bruce et al. e.g., 2014a).

In order to quantify the morphological evolution, various structural parameters have proven to be useful proxies for visual classification. In general, disk galaxies have been associated with a low ($n \sim 1$) sersic index surface brightness profile (or an exponential profile), and elliptical galaxies with a high ($n \sim 4$) sersic index light profile (de vacouleurs profile). Along with a sersic parameter, galaxies have also been quantified based on their effective radius, r_e , and their apparent axis ratio, q .

On a galaxy-by-galaxy basis, q is not in itself a very useful parameter as it can depend strongly on inclination angle. However, distributions of q have been used to infer the intrinsic axis ratios of populations of galaxies separated by their Hubble type (e.g., Sandage et al. 1970; Lambas et al. 1992) and by mass, star-forming state and redshift (e.g., Law et al. 2012; Chang et al. 2013; van der Wel et al. 2014b). For instance, in the local universe, Lambas et al. (1992) found that the elliptical q -distribution implied that these galaxies are intrinsically triaxial as pure oblate/prolate models could not account for the observed axis ratio distributions.

van der Wel et al. (2014b) and Chang et al. (2013) used similar methodology to measure how the distributions evolve with redshift in star-forming and quiescent galaxies. Chang et al. (2013) confirmed that the apparent axis ratio distribution of quiescent galaxies at low- z is consistent with intrinsic triaxial shapes, and that this is also true in their high-redshift ($1 < z < 2.5$) counterparts. They also found that at $z > 1$, galaxies with $M_* \sim 10^{11} M_\odot$ exhibited a higher oblate fraction which they interpreted as massive galaxies being comprised of disks in the past, which were destroyed in major-merger events. For lower-mass quiescent galaxies ($M_* < 10^{11.5} M_\odot$), the evolution of the oblate fraction is reversed, with low-mass quiescent galaxies at high- z not having sufficient time to settle into stable disk systems as compared to today.

In star-forming galaxies, van der Wel et al. (2014b) found that disks are ubiquitous among massive galaxies at all redshifts below $z \sim 2$. At lower stellar mass ($M_* < 10^{10} M_\odot$), the fraction of galaxies with elongated intrinsic shapes increases towards higher redshifts and lower masses, and that similar to their low-mass quiescent counter parts discussed in Chang et al. (2013), these galaxies did not have sufficient time to settle into stable disks. This interpretation is supported by kinematic analysis in IFU studies, such as Simons et al. (2017) who find that disordered (i.e. dispersion dominated) motions decreases with decreasing redshift in low-mass star-forming galaxies.

In this study, we choose to investigate the median apparent axis-ratio (q_{med}) evolution instead of modelling the distributions and inferring their intrinsic shapes.

We instead, infer the intrinsic flattening from the median flattening, with the underlying assumption that the trends in the median encapsulate trends in the larger population. This is caveated with the fact that many studies who investigated the apparent axis ratio distribution, $P(q)$, find that a single morphological type often does not reproduce the observed $P(q)$, and that the models demand a more heterogeneous population (e.g., Lambas et al. 1992; Chang et al. 2013; van der Wel et al. 2014b). By using the q_{med} , we can quantify the dependency on other structural parameters such as n , and r_e and their evolution. We analyze how these values change as a function of the star-forming state of these galaxies and determine what q_{med} is tracing in these different populations.

Throughout this article, we assume a Λ -CDM cosmology ($H_0 = 70 \text{ kms}^{-1}\text{Mpc}^{-1}$, $\Omega_M = 0.3$, and $\Omega_\Lambda = 0.7$).

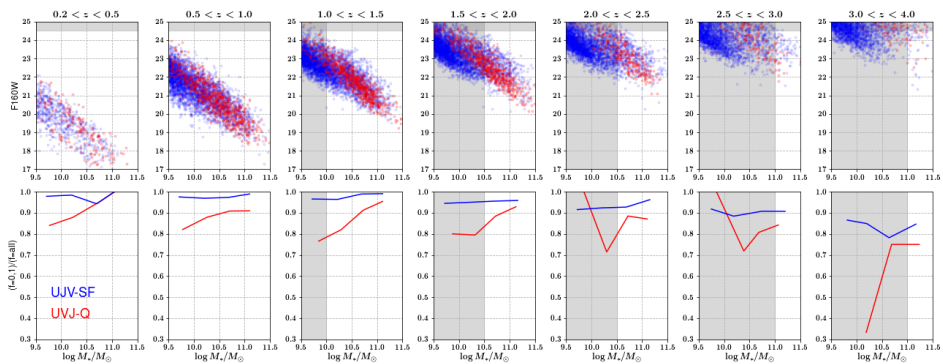


Figure 4.1 The top panels are the $F160W$ magnitude plotted against mass, with each panel showing a different redshift bin. The bottom panels show the corresponding recovery of ‘good’ fits (i.e. a flag value of 0 or 1 the van der Wel et al. (2012) catalogs) as a function of UVJ star-forming state. The grey-shaded region marks our selected mass and magnitude completeness limits for this study, with the mass limit evolving with increasing z .

4.2 Sample Selection

This work makes use of the structural parameter catalogues of van der Wel et al. (2012) which were generated using GALFIT Peng et al. (2010). We also utilize the most recent (v4.1.5) photometric catalogues on which they are based from the CANDELS-3DHST survey (Brammer et al. 2012; Skelton et al. 2014). We use the stellar population parameters, and rest-frame colours based on the ‘zbest’ catalogues, which will use (if available) first a spectroscopic redshift, then a (good) grism redshift and lastly a photometric redshift if a spectroscopic and grism redshift were not available. We refer the reader to the aforementioned papers and their associated documentation for details.

Table 4.1. Number of galaxies in each redshift range by UVJ SF-state

z -range	<i>Quiescent</i>	<i>Starforming</i>
$0.2 < z < 0.5$	173	589
$0.5 < z < 1.0$	781	3426
$1.0 < z < 1.5$	643	1904
$1.5 < z < 2.0$	357	614
$2.0 < z < 2.5$	187	477
$2.5 < z < 3.0$	16	78
$3.0 < z < 4.0$	12	44

Note. — Above are the number of galaxies in each redshift range that are above our mass limits outlined in Fig. 4.1.

We perform a first pass selection using the 3DHST photometric flags (`use_phot = 1`), as well as an *F160W* magnitude cut of $m_{AB} = 24.5$ to ensure uncertainties in size and shape were within 10% (as described in van der Wel et al. 2012). We use objects with a quality flag of $f = 0, 1$ in van der Wel et al. (2012) which means that GALFIT converged on a solution (without crashing) and that the solution did not require parameters to take on their ‘constraint’ values.

We also separate our sample into SF and Q galaxies based on their rest-frame $U - V$ and $V - J$ colours, where galaxies display a colour bi-modality and separate based on specific star formation rates (Labbé et al. 2005; Williams et al. 2009, 2010; Whitaker et al. 2011). We use the *UVJ* boundaries defined in Muzzin et al. (2013b) to separate the Q and SF sequences.

In Figure 4.1 we have plotted the *F160W* AB magnitude, and the fraction of ‘good’ structural fits ($f = 0, 1$ in van der Wel et al. (2012)) as a function of mass and redshift, as well as SF state to determine our mass completeness as a result of our magnitude limit and the effect of our decision to take only ‘good’ structural parameters. In the top panels we have indicated the mass completeness limit for each redshift (which ranges from $\log M_*/M_\odot = 9.5 - 11.0$), to ensure sufficient signal-to-noise (S/N). In the bottom panels, we see the recovery of ‘good’ structural fits is always greater in the SF galaxies, likely because of the difference in their rest-frame optical colours. This is particularly striking for quiescent galaxies at the highest redshift bin ($3.0 < z < 4.0$) at $\log M_*/M_\odot < 10.5$ where we see the recovery of ‘good’ fits is $\sim 30\%$. However, our mass cut from the top panels ensures we have recovered $> 80\%$ of the total galaxies in each redshift bin.

After applying all the aforementioned selection criteria to the complete 3DHST catalogue, we are left with 9301 galaxies. A census of these galaxies broken down into their respective redshift and UVJ-SF state can be found in Table 4.1.

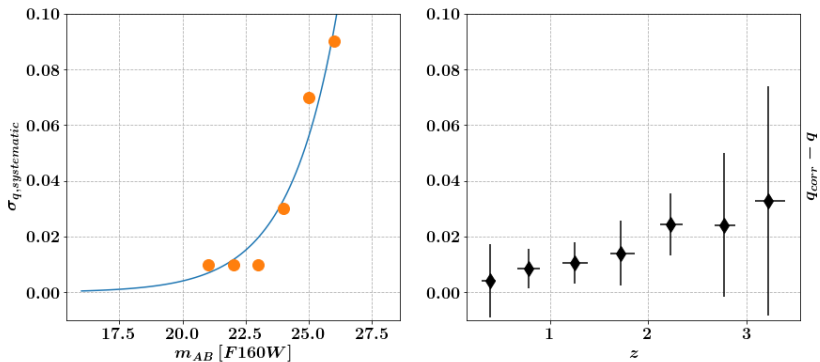


Figure 4.2 Left: Magnitude of the systematic uncertainty as measured by van der Wel et al. (2012) (orange points; see their Table 3) as a function of the $F160W$ magnitude. The blue line is an exponential fit to the data. Right: The difference between the q_{med} from the original structural catalog from van der Wel et al. (2012) and a correction to q_{med} (q_{corr} , based on the fit in the left panel) as a function of z . The error bars show the variance in values. As expected, the total effect of the systematics grows bigger with redshift.

4.3 Analysis

4.3.1 Correcting for Systematics

Since we are taking a median of $P(q)$, and we have already imposed a fairly conservative S/N cut, our random errors on the median are a fraction of a percent for most data points in this article. However, the systematics in q can be significant at the faintest magnitudes. Since we wish to investigate the trends with flattening out to significant z , rather than exclude these galaxies from our sample, we chose to correct for the systematics investigated by van der Wel et al. (2012).

In their article, van der Wel et al. (2012) used model light profiles convolved with the noise and PSF profiles of HST to estimate the effects of systematics. They repeated their surface brightness profile fitting on the simulated images and found that near the magnitude limits of their survey, the measured q in the data were flatter than the model images. In their Table 3, they tabulated the average systematic as a function of $F160W$ magnitude, which we have plotted in Fig. 4.2. In the left panel of Fig. 4.2, we fit an exponential function to the data, and made corrections to the values of q in the catalog based on each object's $F160W$ magnitude. Although we do not know the magnitude of the systematic for any individual object, our approach of medians means we can apply these corrections. In the right panel of Fig. 4.2 we have shown the median correction as a function of z . As expected, the magnitude of the correction is larger at higher redshift, where the sample is dominated by objects at fainter magnitude limit (as seen in the upper

panel of Fig. 4.1).

Unless otherwise specified, the values of q presented in this paper are corrected for the systematic effects.

4.3.2 Trends with star-formation, M_* , z , r_e and n

To investigate trends in q_{med} with other properties, we binned our galaxies into 7 different redshift bins (with ranges specified in Table 4.1), as well as 4 different stellar mass bins ($\log M_*/M_\odot \in [9.5, 10.0]$, $[10.0, 10.5]$, $[10.5, 11.0]$, $[11.0, 12.0]$), 3 bins of r_e ($r_e[kpc] \in [0, 3]$, $[3, 6]$, $[6, 9]$, $[9, 20]$), and 3 bins of n ($n \in [0, 2.0]$, $[2.0, 4.0]$, $[4.0, 8.0]$). We exclude galaxies with $r_e < 0.1''$ from our sample, as this is smaller than the HWHM of the PSF.

In Fig. 4.3 we have plotted q_{med} as a function of $\log M_*/M_\odot$ and z . In this figure, we only plot our results to $z = 2.5$ because we are not complete in mass above this redshift (although we plot our highest mass bin, $M_* > 10^{11} M_\odot$ where we are complete in Fig. 4.4). Considering only the quiescent galaxies, we see that there are no strong trends with stellar mass. On the other hand, star-forming galaxies at $z < 1$ do display a broad mass dependence, with lower mass galaxies appearing flatter than higher mass galaxies which could be driven by the bulge-to-disk ratio. Because we are mass-limited, whether or not this trend continues at $z > 1$ is an open question which would require deeper survey depths to answer.

If we now consider the broad difference between quiescent and star-forming galaxies in Fig. 4.3, we see that at $z < 2.0$, the quiescent galaxies are always rounder than their equivalent mass star-forming counterparts. This becomes less apparent at $z > 2.0$ where at $\log M_*/M_\odot > 11.0$, the axis ratios are equivalent. This could be indicative of similar morphology between the two populations at these redshifts.

We investigate this similarity to higher redshifts by only considering galaxies in our highest mass bin where we have sufficient redshift coverage given our mass-complete limits. In Fig. 4.4, we have plotted the apparent axis ratio of galaxies in our highest mass bin as a function of redshift. We see quiescent galaxies are flatter at higher redshifts of equivalent mass, whereas the star-forming galaxies show little evolution in q_{med} with redshift. As in Fig. 4.3, at $z < 2$, the quiescent galaxies are rounder than their star-forming counterparts. At $z > 2$, we see that there is no discernible difference in the q_{med} between the star-forming and quiescent populations, suggesting that at this mass (as alluded to in Fig. 4.3) perhaps these galaxies have similar structure.

Given the known association between a galaxy's mass and size (e.g., Shen et al. 2003; van der Wel et al. 2014a; Lange et al. 2015) and that the size of galaxies at an equivalent mass are observed to be smaller at larger redshifts (e.g., Daddi et al. 2005; Trujillo et al. 2006; van Dokkum et al. 2008; Straatman et al. 2015), it is also important to determine whether the trends observed in Fig. 4.3 are driven by the size evolution. As previously mentioned, we have binned our data according to r_e and have plotted how this evolves with z and M_* in Fig. 4.5 and Fig. 4.6, respectively, but have omitted bins with fewer than 3 galaxies.

In Fig. 4.5, we see that the q_{med} of star-forming galaxies depends more strongly

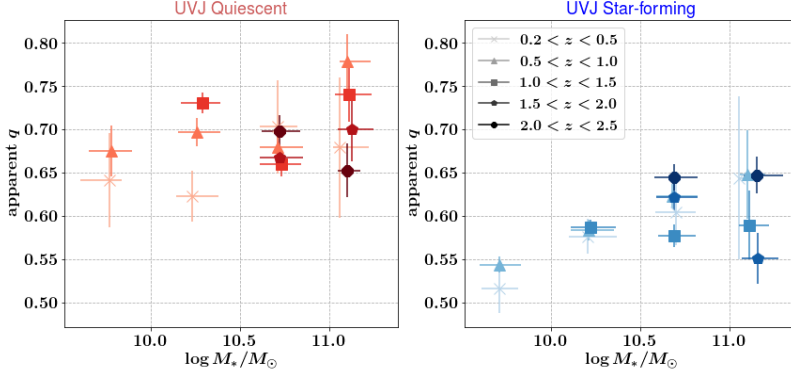


Figure 4.3 Apparent axis ratio as a function of mass and redshift for both UVJ-quiescent (left) and UVJ-SF (right). The error bars in $\log M_*/M_\odot$ represent the interquartile range, and the error bars in q_{med} are the 1σ range from a bootstrapped median, and represents the variance.

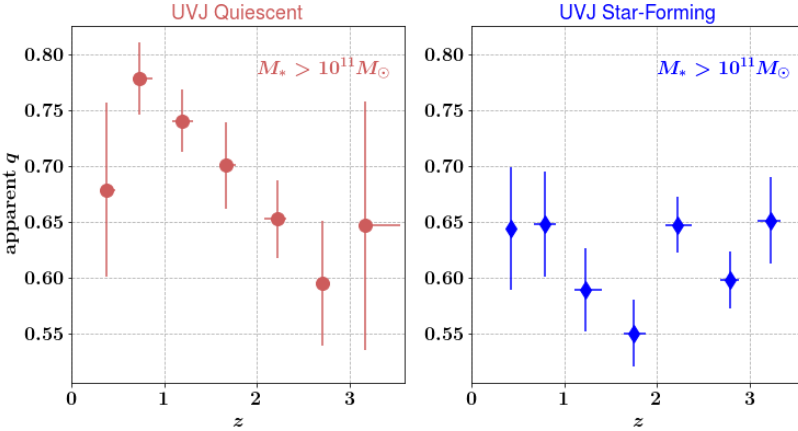


Figure 4.4 Apparent axis ratio as a function of redshift, and separated into quiescent (left) and star-forming galaxies (right) via a UVJ colour selection for galaxies at $M_* > 10^{11} M_\odot$. The error bars in q_{med} are from the bootstrapped median, and are representative of the scatter, and the error bars in z show the interquartile range. Here we see the quiescent galaxies are rounder than the star-forming galaxies at $z < 2$, but are comparable at $z > 2$. We also note that the apparent axis ratio has shown significant evolution in quiescent galaxies, but the trend in q_{med} with z for star forming galaxies is flat.

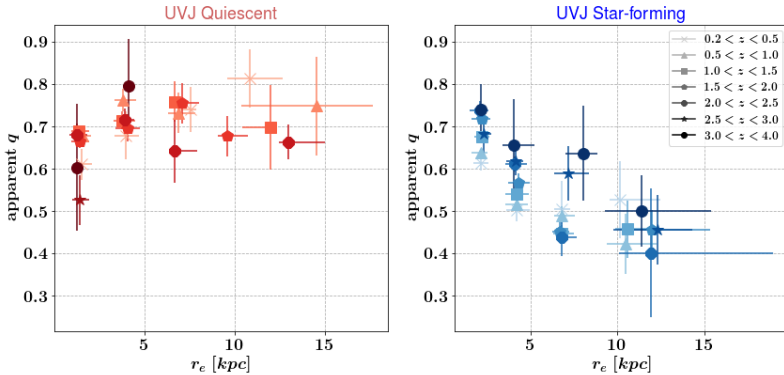


Figure 4.5 Apparent axis ratio as a function of effective radius for the same redshifts bins as Fig. 3. As in previous figures, the error bars in q_{med} are the 1σ from the bootstrapped sample, and the errors in r_e represent the interquartile range. Bins with 2 or fewer galaxies have been omitted, which is why there are missing data points in the left hand panel at $z > 2.5$. In star-forming galaxies, there is a significant anti-correlation between q_{med} and r_e , although no consistent z evolution.

on r_e than their quiescent counterparts, with large galaxies being flatter than smaller galaxies. At low- z , quiescent galaxies become marginally rounder with increasing size, with this trend disappearing, or even reversing at $z > 2$. The stronger trend in q_{med} with r_e in star-forming galaxies could be the result of the bulge-to-disk ratio (B/T), with the bulge ‘out-shining’ the disk at smaller r_e .

Fig 4.6 echoes the trends with r_e seen in Fig. 4.5 (with star-forming galaxies showing stronger correlations than quiescent galaxies), however there is a much stronger dependence on M_* than with z , with massive galaxies always rounder than less massive galaxies at fixed r_e , with the exception of the smallest quiescent galaxies where the trend reverses. These trends are also what are expected if the B/T ratio increases with increasing M_* and decreasing r_e . In this figure, we also plot q_{med} as a function of $r_e/r_{e,ms}$, where $r_{e,ms}$ is the expected size given the stellar mass from the mass-size relations of van der Wel et al. (2014a). This can be thought of as a deviation from the mass-size relation. When plotting this fraction instead of the r_e , we see the mass dependence largely disappears in both quiescent and star-forming galaxies. In quiescent galaxies we see a relatively flat relationship. For star-forming galaxies, galaxies that lie below the mass-size relation are rounder than those that lie above it.

In Fig. 4.7, we investigate the dependencies of n on q_{med} and M_* . In this Figure, the galaxies have been binned by n . We observe a strong positive correlation between q_{med} and n in both quiescent and star forming galaxies, with no significant M_* dependence. Because there is no significant M_* dependence, we have plotted trend lines in Fig. 4.7 based on the median of all galaxies, as well as only

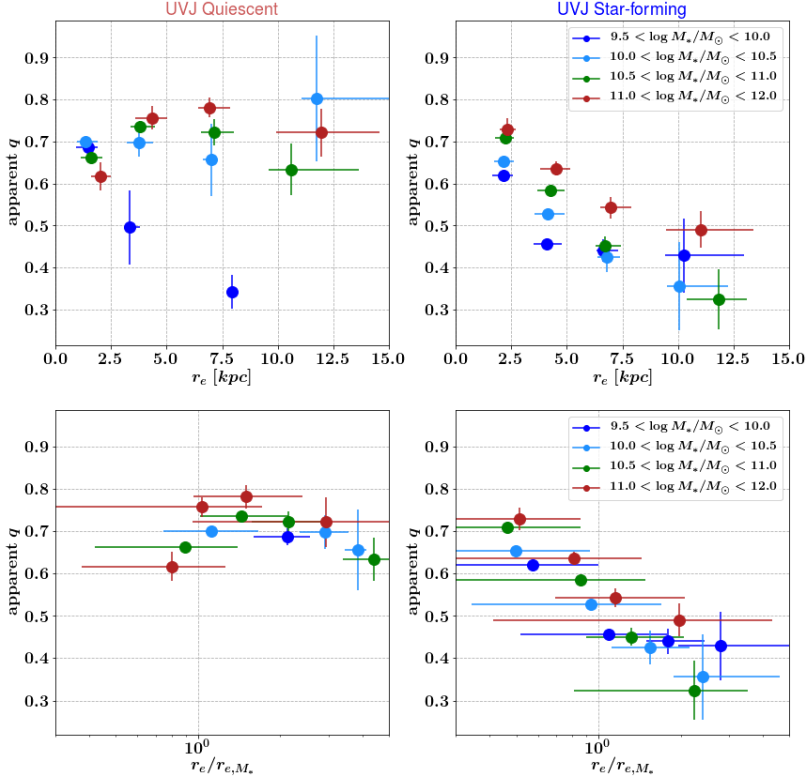


Figure 4.6 Top: Similar to Fig. 4.5, except galaxies have been binned according to M_* instead of redshift. Bottom: The same as the top row, except instead of plotting the axis ratio against r_e , we have plotted the ratio of r_e to the expected size based on its mass from the mass-size relation of van der Wel et al. (2014a) ($r_{e,ms}$). The differences in mass bin seen in the top row disappear when considering the deviation from the mass-size relation.

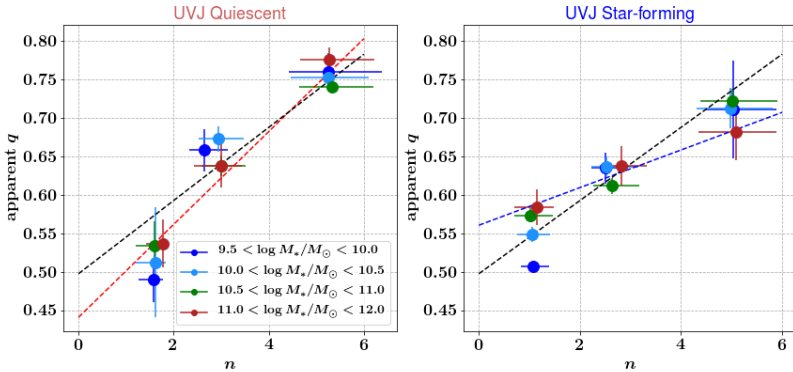


Figure 4.7 Apparent axis ratio binned by sersic index for 4 different mass bins for UVJ-quiescent (left) and UVJ-SF (right). Black dashed lines both panels is the linear least squares fit to the combined star-forming and quiescent sample. Red and blue dashed lines are the linear fits to the quiescent and star-forming galaxies, respectively. In the left panel, we see no apparent mass evolution in the quiescent galaxies, but we do see a strong evolution in sersic index. In the right panel, we see a flatter, albeit, still strong relationship between n and q_{med} , with no apparent mass trend, except in the lowest mass bin where more massive galaxies are rounder.

the quiescent/star-forming in their respective n bin. These lines show that the n dependence is steeper for quiescent galaxies. This is the most significant trend observed out of the structural parameters investigated.

4.3.3 Is n driving trends with q_{med} ?

Because of the tight relationship between q_{med} and n , we re-investigate the observed trends with q_{med} to test the extent to which these trends can be explained by trends in n . To this end, we re-calculate q_{med} using their measured values of n as well as the relationships for star-forming and quiescent galaxies in Fig. 4.7, q_n . We then take the residual between q_{med} and q_n and plot that against M_* , z and r_e .

Fig. 4.8 shows the residuals of the values in Fig. 4.3. In this figure, we see for most data points that the residuals are $\sim 10\%$ of the original values, and can account for most of the observed q_{med} . For star-forming galaxies, although there is structure in the residuals, n can also account for the trends, especially at the lowest redshifts.

In Fig. 4.9, we show the residuals of the relationship of our massive galaxy subsample ($M_* > 10^{11}$) with z . In massive galaxies, we see that q_{med} can be fully accounted for by n , and the trend of massive galaxies becoming rounder at lower redshift is also gone, with this relationship accounted for by an evolution in the median n . We see the flat relationship with star-forming galaxies is also maintained. Therefore, we conclude that the evolution in n can account for any

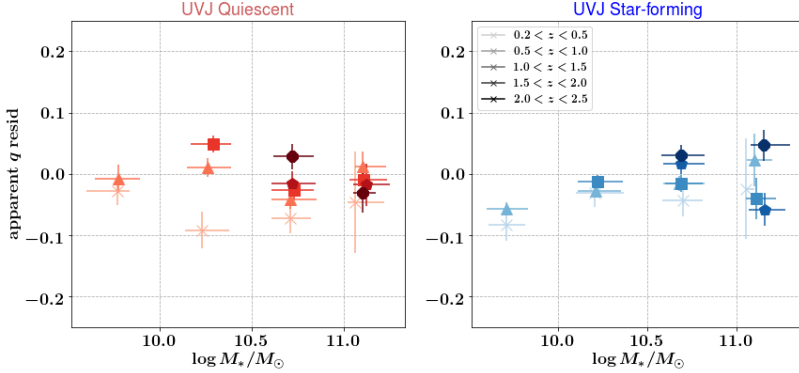


Figure 4.8 These plots contain the same galaxies and bin as in Fig. 4.3, except the abscissa is now the residual between the actual q_{med} , and q_n where q_n is the q_{med} expected based on the galaxies sersic index using the quiescent and star-forming relationships from Fig. 4.7. n is able to account for the observed q_{med} to within $\sim 10\%$ for most of the mass and redshift bins. Although there is structure in the residuals for the star-forming galaxies, the spread in q_{med} observed in Fig. 4.3 disappears, suggesting n is sufficient to explain the trends.

q_{med} evolution in massive galaxies.

Although n can convincingly account for most of the observed q_{med} , as well as trends with M_* and z , it is insufficient to explain the trends in r_e for star-forming galaxies. Fig. 4.10 and Fig. 4.11 are the residuals plots of Fig. 4.5 and Fig. 4.6, respectively. For the quiescent galaxies in Fig. 4.6, we do see that the previously seen mass dependence of q_{med} at fixed radius is gone (again with the exception of galaxies at the smallest radius). However, the mass dependence for star-forming galaxies persists, as well as the overall trend with r_e .

4.4 Discussions and Conclusions

In the previous sections, we investigated the dependence of the observed q_{med} with various structural parameters. At all masses below $z < 2$, quiescent galaxies are rounder than their star-forming counterparts (Fig 4.3). For quiescent galaxies, when binned by M_* there was no discernible trend with mass, whereas star-forming galaxies do show a significant mass dependence at low-redshift ($z < 1.0$). At the highest masses ($M_* > 10^{11}$), quiescent galaxies show a strong trend, becoming increasingly flat at higher- z , until they match the apparent q_{med} at $z > 2$, suggesting that at the highest redshifts, massive quiescent galaxies are structurally similar to their star-forming counterparts, and that high- z quiescent galaxies could be disk-like, a notion that has been posited previously (e.g., van der Wel et al. 2011; Wuyts et al. 2011; Bruce et al. 2012; Chang et al. 2013; Newman et al. 2015; Hill et al.

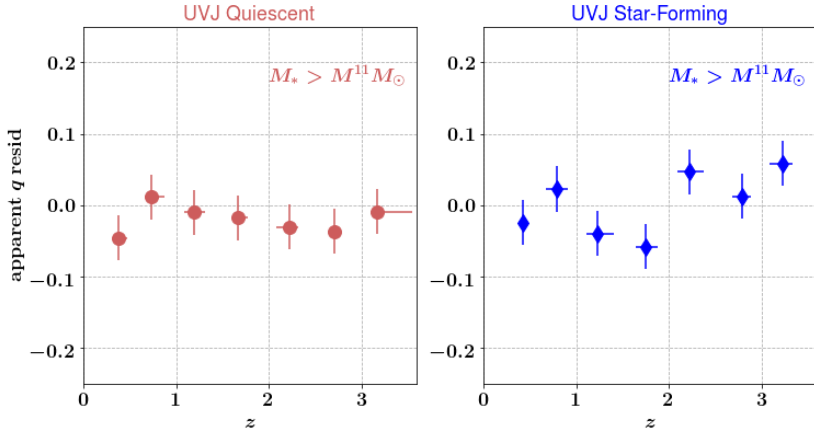


Figure 4.9 This figure shows the residuals of Fig. 4.4, after subtracting q_n (the expected q_{med} from a galaxy’s n assuming the relationships from Fig. 4.7) for galaxies at $\log M_*/M_\odot > 10^{11}$. The strong trend of q_{med} with z for quiescent galaxies are consistent with zero, showing the trend was driven by an evolution in the axis ratio and that n is able to account for the observed q_{med} for massive galaxies. The residuals with the star-forming galaxies are also consistent with zero.

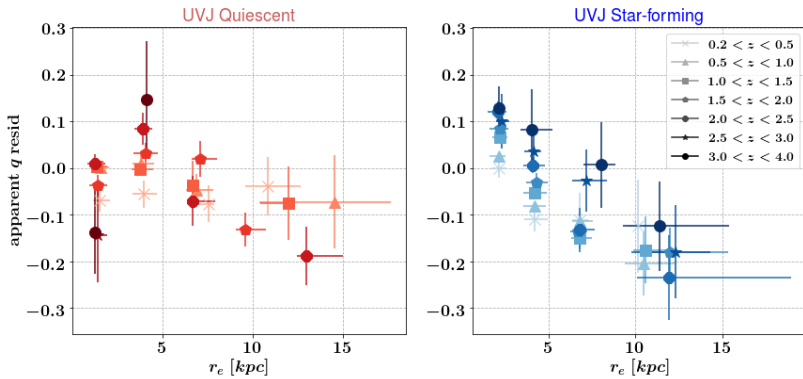


Figure 4.10 This figure shows the residuals of Fig. 4.5, after subtracting q_n (the expected q_{med} from a galaxy’s n assuming the relationships from Fig. 4.7) for galaxies at $\log M_*/M_\odot > 10^{11}$. This trend is sufficient to explain the observed q_{med} of quiescent galaxies, but does not account for the trend of q_{med} with r_e in star-forming galaxies where the magnitude of the trend persists.

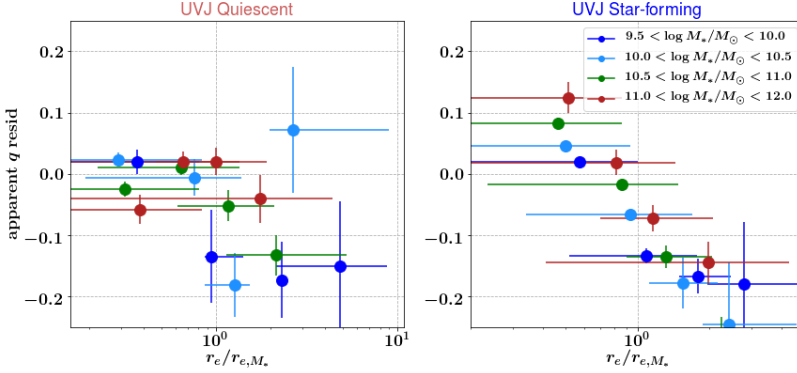


Figure 4.11 The residual values after subtracting q_n (the expected q_{med} from a galaxy’s n assuming the relationships from Fig. 4.7) from q_{med} in Fig. 4.6. As in Fig. 4.10, n is able to account for $\sim 80 - 90\%$ of the observed q_{med} in quiescent galaxies. In star-forming galaxies, the observed trend with r_e cannot be accounted for with n .

2017)

The observed trend of massive galaxies flattening at higher redshift (Fig. 4.4) can be explained entirely by the dependence of n on q_{med} . This conclusion was drawn through an analysis of the residuals after subtracting the effect of n from q_{med} . To obtain this correction, we binned our sample according to n and M_* and found n to correlate strongly with q_{med} and surprisingly, with no apparent stellar-mass dependence (Fig. 4.7). By using the linear relationship surmised in Fig. 4.7, we calculated what q_{med} would be given the modelled n from the catalog of van der Wel et al. (2012), and plotted the residuals. The residuals for q_{med} with z in massive galaxies were consistent with 0 (Fig. 4.9), with the conclusion that the evolution in n drives the evolution in q_{med} .

The q_{med} -residuals were also plotted for the other masses, which showed very little residual correlation. However, the magnitude of the trend between q_{med} and M_* for star-forming galaxies is not successfully accounted for by n , as there is still structure in the residuals from the lowest stellar-mass bin. This could be because these low-mass galaxies are triaxial, although further investigation is required.

When binning galaxies based on their r_e , for star-forming galaxies we observed an inverse correlation between q_{med} and r_e , with larger galaxies exhibiting stronger flattening than smaller star forming galaxies, regardless of z (Fig. 4.5). This trend persists when comparing star-forming galaxies at fixed r_e in different mass bins (Fig. 4.6). At fixed r_e , massive galaxies are always rounder than lower mass galaxies, regardless of star-forming state (with the exception of the smallest quiescent galaxies which requires further investigation). This mass dependence disappears when considering q as a function from the deviation of the relevant mass-size relation (Fig. 4.6).

One possible interpretation of our results is that q_{med} is tracing the bulge-to-total galaxy ratio (B/T) in star-forming galaxies. It has been shown previously that n broadly traces B/T in massive galaxies (e.g., Bruce et al. 2014b; Kennedy et al. 2016); this combined with the our observation that q_{med} is also tracing n links this idea quite well. This would explain why smaller star-forming galaxies are rounder than extended star-forming galaxies, as well as why more massive star-forming galaxies are rounder than less-massive galaxies at fixed radii (Fig. 4.11); the bulge is dominating more of the light in smaller galaxies, and more massive star-forming galaxies have built up more of a bulge.

This could potentially provide a proxy for estimating the dominance of bulges in galaxy populations at high- z when the size of the galaxy is approaching the PSF of the instrument making seraic modelling increasingly uncertain (see, for example, Hill et al. 2017). We do emphasize that all of these trends are based on medians of populations, and thus would likely be inapplicable on a galaxy-by-galaxy basis. There is much more detailed investigation required to confirm this result.

4.5 Summary

We have taken the catalogues of van der Wel et al. (2012) and studied the evolution of the median apparent axis ratio (q_{med}) for over 9000 galaxies out to $z = 3$ with M_* , z , n and r_e . We find

1. Quiescent galaxies are rounder than their star-forming counterparts at all masses below $z < 2$. Above $z > 2$, the flattening between massive quiescent and star-forming galaxies is identical, suggesting they had very similar structure in the early universe. This is an extension in redshift of previous work (Chang et al. 2013) who found an increased incidence of disk-like structure in massive quiescent galaxies at $z > 1$.
2. The flattening in quiescent galaxies is mass independent, whereas in star-forming galaxies, there is a strong positive correlation with stellar mass at least until $z = 1$; due to our mass limits, whether this trend continues to higher z is an open question.
3. In star-forming galaxies, q_{med} correlates significantly with r_e , in contrast to quiescent galaxies where there is no significant trend.
4. In quiescent galaxies, the strongest common correlation was between q_{med} and n . For most relationships, there is very little residual correlation between q_{med} and q_n (the expected q calculated from the sérsic index), however this was not the case in star-forming galaxies.
5. We suspect that q_{med} is likely tracing the B/T ratio which would explain why smaller/more massive star-forming galaxies are rounder than their extended/less massive counterparts, as well as why we do not observe strong M_* and r_e dependencies in quiescent galaxies, as the majority of the quiescent galaxies are not expected to have prominent disks. We caveat that we are

also only tracing the light, which would weight blue disks with lower mass-to-light ratios heavily in the observables, and that the mass distribution could be quite different.

4.6 Acknowledgments

This research has made use of NASA’s Astrophysics Data System.

References

- Blanton, M. R., Hogg, D. W., Bahcall, N. A., et al. 2003, *ApJ*, 594, 186
 Brammer, G. B., van Dokkum, P. G., Franx, M., et al. 2012, *ApJS*, 200, 13
 Bruce, V. A., Dunlop, J. S., Cirasuolo, M., et al. 2012, *MNRAS*, 427, 1666
 Bruce, V. A., Dunlop, J. S., McLure, R. J., et al. 2014a, *MNRAS*, 444, 1001
 —. 2014b, *MNRAS*, 444, 1660
 Chang, Y.-Y., van der Wel, A., Rix, H.-W., et al. 2013, *ApJ*, 773, 149
 Daddi, E., Renzini, A., Pirzkal, N., et al. 2005, *ApJ*, 626, 680
 Hill, A. R., Muzzin, A., Franx, M., et al. 2017, *ApJ*, 837, 147
 Kennedy, R., Bamford, S. P., Häußler, B., et al. 2016, *MNRAS*, 460, 3458
 Labbé, I., Huang, J., Franx, M., et al. 2005, *ApJL*, 624, L81
 Lambas, D. G., Maddox, S. J., & Loveday, J. 1992, *MNRAS*, 258, 404
 Lange, R., Driver, S. P., Robotham, A. S. G., et al. 2015, *MNRAS*, 447, 2603
 Law, D. R., Steidel, C. C., Shapley, A. E., et al. 2012, *ApJ*, 745, 85
 Muzzin, A., Marchesini, D., Stefanon, M., et al. 2013, *ApJ*, 777, 18
 Newman, A. B., Belli, S., & Ellis, R. S. 2015, *ApJL*, 813, L7
 Peng, C. Y., Ho, L. C., Impey, C. D., & Rix, H.-W. 2010, *AJ*, 139, 2097
 Roberts, M. S., & Haynes, M. P. 1994, *ARA&A*, 32, 115
 Sandage, A., Freeman, K. C., & Stokes, N. R. 1970, *ApJ*, 160, 831
 Shen, S., Mo, H. J., White, S. D. M., et al. 2003, *MNRAS*, 343, 978
 Simons, R. C., Kassin, S. A., Weiner, B. J., et al. 2017, *ApJ*, 843, 46
 Skelton, R. E., Whitaker, K. E., Momcheva, I. G., et al. 2014, *ApJS*, 214, 24
 Straatman, C. M. S., Labbé, I., Spitler, L. R., et al. 2015, *ApJL*, 808, L29
 Trujillo, I., Förster Schreiber, N. M., Rudnick, G., et al. 2006, *ApJ*, 650, 18
 van der Wel, A., Rix, H.-W., Wuyts, S., et al. 2011, *ApJ*, 730, 38
 van der Wel, A., Bell, E. F., Häußler, B., et al. 2012, *ApJS*, 203, 24
 van der Wel, A., Franx, M., van Dokkum, P. G., et al. 2014a, *ApJ*, 788, 28
 van der Wel, A., Chang, Y.-Y., Bell, E. F., et al. 2014b, *ApJL*, 792, L6
 van Dokkum, P. G., Franx, M., Kriek, M., et al. 2008, *ApJL*, 677, L5
 Whitaker, K. E., Labbé, I., van Dokkum, P. G., et al. 2011, *ApJ*, 735, 86
 Williams, R. J., Quadri, R. F., Franx, M., van Dokkum, P., & Labbé, I. 2009, *ApJ*, 691, 1879
 Williams, R. J., Quadri, R. F., Franx, M., et al. 2010, *ApJ*, 713, 738
 Wuyts, S., Förster Schreiber, N. M., van der Wel, A., et al. 2011, *ApJ*, 742, 96

A STELLAR VELOCITY DISPERSION FOR A STRONGLY-LENSED, INTERMEDIATE-MASS QUIESCENT GALAXY AT $z = 2.8$

In this paper, we present deep X-Shooter spectroscopy of one of only two known gravitationally-lensed massive quiescent galaxies at $z > 2$. This galaxy is quadruply imaged, with the brightest images magnified by a factor of ~ 5 . The total exposure time of our data is 9.8 hours on-source; however the magnification, and the slit placement encompassing 2 images, provides a total equivalent exposure time of 215 hours. From this deep spectrum we measure a redshift ($z_{\text{spec}} = 2.756 \pm 0.001$), making this one of the highest redshift quiescent galaxies that is spectroscopically confirmed. We simultaneously fit both the spectroscopic and photometric data to determine stellar population parameters and conclude this galaxy is relatively young (560_{-80}^{+100} Myr), intermediate-mass ($\log M_*/M_\odot = 10.59_{-0.05}^{+0.04}$), consistent with low dust content ($A_V = 0.20_{-0.20}^{+0.26}$), and has quenched only relatively recently. This recent quenching is confirmed by strong Balmer absorption, particularly $H\delta$ ($H\delta_A = 6.66_{-0.92}^{+0.96}$). Remarkably, this proves that at least some intermediate-mass galaxies have already quenched as early as $z \sim 2.8$. Additionally, we have measured a velocity dispersion ($\sigma = 187 \pm 43$ km/s), making this the highest-redshift quiescent galaxy with a dispersion measurement. We confirm that this galaxy falls on the same mass fundamental plane (MFP) as galaxies at $z=2.2$, consistent with little to no evolution in the MFP up to $z=2.8$. Overall this galaxy is proof of existence of intermediate-mass quenched galaxies in the distant universe, and that lensing is a powerful tool for determining their properties with improved accuracy.

5.1 Introduction

It is well established that galaxies with evolved stellar populations were already in place when the universe was less than half of its current age (see for example McCracken et al. 2012; Ilbert et al. 2013; Muzzin et al. 2013b). These galaxies were first identified from a population which exhibited red $J_s - K_s$ colors (Franx et al. 2003). These colors were consistent with taking the spectral energy distribution (SED) of an elliptical or dusty star-burst galaxy and red-shifting to $z \sim 2$, with the degeneracy between the two types of galaxies lifted with the inclusion of IRAC data (Labbé et al. 2005; Williams et al. 2009). Out of the Franx et al. (2003) sample, subsequent spectroscopy later confirmed that a subset of these ‘red-galaxies’ were indeed quiescent (van Dokkum et al. 2003; Kriek et al. 2006), establishing that galaxies with strongly suppressed star formation were present at higher redshifts.

A comparison of the stellar populations of quiescent galaxies between $z \sim 2$ and $z \sim 0$ via their mass-to-light ratios show that the stellar populations in these galaxies are consistent with passive evolution (e.g., van Dokkum et al. 1998; Treu et al. 1999; Bernardi et al. 2003; van Dokkum et al. 2006). Although quiescent, the $z \sim 2$ galaxies are strikingly different in their structure compared to present-day ellipticals. At a given mass, their effective radii (r_e) are a factor of $\sim 2 - 4$ smaller than at $z \sim 0$ (e.g., Daddi et al. 2005; Trujillo et al. 2006; Zirm et al. 2007; van Dokkum et al. 2008, 2010; Szomoru et al. 2012). This difference in r_e between present-day ellipticals and high-redshift galaxies implies a rapid structural evolution between $z \sim 2$ and today. Although these galaxies must grow by a factor of a few in size, their central stellar-velocity dispersions show little evolution (Toft et al. 2012; van de Sande et al. 2013; Bezanson et al. 2013; Belli et al. 2014a) between these redshifts.

The evolution of stellar populations between redshift $z \sim 2$ and $z \sim 0$ is mirrored in the evolution of the zero-point in the fundamental plane (FP). The FP represents a locus of galaxies which occupy a tight plane determined by a galaxy’s surface brightness, size and velocity dispersion (Dressler et al. 1987; Djorgovski & Davis 1987). This plane maintains a slight tilt with respect to the expectation from the assumption of virial equilibrium. This tilt is thought to be caused by a deviation from homology (Pahre et al. 1995; Capelato et al. 1995; Busarello et al. 1997), and by variations in the mass-to-light ratio (van Dokkum et al. 1998; Cappellari et al. 2006; Robertson et al. 2006; Bolton et al. 2007; Cappellari et al. 2013).

When the dependence of the FP on surface brightness is replaced with the average stellar mass density (i.e. the mass fundamental plane; henceforth MFP), the tilt in the FP virtually disappears (Bolton et al. 2007), or is at least shown to be weaker than the tilt in the FP (Bolton et al. 2008; Holden et al. 2010; Bezanson et al. 2013). In contrast to the evolution in the zero-point of the FP (e.g., van de Sande et al. 2014), the MFP zero-point shows very little evolution out to $z \sim 2$ (Bezanson et al. 2013), reminiscent of the lack of evolution in central stellar-velocity dispersion (Toft et al. 2012; Bezanson et al. 2013; Belli et al. 2014a). However the precise evolution depends on assumptions when counting galaxies and how to connect progenitors to their descendants (van de Sande et al. 2014).

The consistency of the slope of the MFP with that predicted from virial equi-

librium points to variations in mass-to-light ratios as the likely cause of the tilt in the FP. The evolution in mass-to-light ratios are driven by either variations in dark matter content, variations in stellar populations, or a combination of both. In the context of MFP evolution at high- z , it is important to note that the sample of Bezanson et al. 2013 in the highest redshift bin was restricted to massive galaxies i.e $\log M_*/M_\odot > 11.0$, leaving the MFP unpopulated below this mass threshold at $z \sim 2$, and due to redshift coverage, at all masses above $z \sim 2$.

Although valuable for testing the evolution of the MPF, measuring stellar velocity dispersions of quiescent galaxies beyond $z \sim 2$ has proven technically challenging. At these redshifts their optical absorption lines are redshifted to the near-infrared (NIR) which has a high and variable sky background. In contrast to actively star-forming galaxies, measuring a stellar-velocity dispersion of quiescent galaxies requires a continuum detection, with moderate signal-to-noise ratios (S/N). Because of the long integration times required to achieve the necessary S/N enabling a stellar velocity dispersion measurement, the community has been restricted to observing the brightest galaxies at these redshifts (Onodera et al. 2010; van de Sande et al. 2011; Toft et al. 2012; van de Sande et al. 2013; Bezanson et al. 2013; Belli et al. 2014a), which van de Sande et al. (2014) showed is also biased towards younger post-starburst galaxies.

In order to probe higher redshifts and/or lower masses, and circumvent the need for long integration times prior to the era of the James Webb Space Telescope (JWST), we aim to take advantage of the brightening and magnifying effects of strong gravitational lensing. This tool has been successfully implemented in studying the properties of distant star-forming galaxies, with higher resolution and better signal-to-noise than normally possible including Lyman-break (e.g. Smail et al. 2007), sub-millimetre (e.g. Vieira et al. 2013) and UV-bright galaxies (e.g. Brammer et al. 2012; Sharon et al. 2012; van der Wel et al. 2013). We aim to extend the utility of gravitational lensing to red, quiescent galaxies.

Lensed, quiescent galaxies at high redshifts ($z > 2$) are comparably more difficult to find than lensed star-forming galaxies for a variety of reasons. First quiescent galaxies show a declining number density with increasing redshift (i.e., Muzzin et al. 2013b). Thus, there are fewer quiescent galaxies to be lensed at high redshift as compared to star-forming galaxies. Secondly, blue, lensed star-forming galaxies stand out in red, quiescently dominated galaxy clusters, whereas red, lensed galaxies do not. One of the best places to search for lensed galaxies is behind galaxy clusters as they have deep potential wells. As a result of high star formation rates (SFR), SMGs exhaust their gas on relatively short timescales, and are thus extremely rare in local galaxy clusters. Because of SMG rarity in local clusters, the foreground lensing cluster has few sources in the sub-mm images allowing for trivial detection of the lensed SMGs. This is not the case for quiescent galaxies, where the foreground cluster is also NIR bright. Blue, star-forming galaxies are UV-bright, and lensed candidates at redshift ~ 2 have this emission shifted to the rest-frame optical, making the high-redshift blue galaxies behind clusters optically bright. With the existence of wide and relatively deep optical surveys such as SDSS, there is a wealth of lensed blue galaxies (e.g. Stark et al. 2013), however large area NIR surveys of comparable depth are not available.

As such, there are only five red, lensed galaxies presented in the literature. Auger et al. (2011) present an intermediate redshift ($z = 0.6$) lensed candidate which is multiply imaged. Two of the high-redshift ($z = 1.71, 2.15$) examples in the literature (Geier et al. 2013) are singly imaged, which are more difficult to create lens models for. There are only two examples of multiply imaged red-lenses at high redshift. One, found by Newman et al. (2015), with a spectroscopic redshift of $z = 2.636$, and the other is the object of this study which was first identified by Muzzin et al. (2012).

In this paper we present X-Shooter spectroscopy, and a stellar velocity dispersion measurement of COSMOS 0050 + 4901, a quiescent galaxy found by Muzzin et al. (2012) in the COSMOS/UltraVISTA field (McCracken et al. 2012). With the current data, this is now the highest redshift quiescent galaxy with a stellar velocity dispersion measurement, as well as the least massive quiescent galaxy beyond redshift 2 with a rest-frame optical spectrum.

We assume a Λ -CDM cosmology ($H_0 = 70 \text{ kms}^{-1}\text{Mpc}^{-1}$, $\Omega_M = 0.3$, and $\Omega_\Lambda = 0.7$), and AB magnitudes.

5.2 Data

5.2.1 COSMOS 0050+4901

COSMOS 0050 + 4901 is a strongly-lensed system where the lens is a single galaxy at $z = 0.960$ found serendipitously in the COSMOS/UltraVISTA field (McCracken et al. 2012) as a group of exceptionally bright, red galaxies. The source is quadruply imaged, with photometric redshifts of $z \sim 2.3 - 2.4$ (depending on which of the multiple images is analyzed; Muzzin et al. 2012, hereafter M12). The brightest 3 images are magnified by a factor of ~ 5 (M12, Muzzin et al. in prep). In Fig. 5.1 we show a 3-color UltraVISTA J, H and Ks-band image of the lens-source system. Included in this figure is the placement of the slit used for the spectroscopic data (see Sec. 5.2.3). As illustrated by the slit position shown in Fig. 5.1, we have obtained spectroscopy of two images, effectively doubling our exposure time. Fig. 5.1 also qualitatively illustrates the difference in color between the foreground lens and the source images as a result of their differing redshifts.

M12 performed an initial estimate of the structural properties of the galaxy using the ground-based K_s -band data. Assuming the best photometric redshift at that time, they estimated an $r_e = 0.64^{+0.08}_{-0.18}$ kpc and a Sersic index of $n = 2.2^{+2.3}_{-0.9}$. Recently, we have obtained high-resolution HST F160W imaging of COSMOS 0050 + 4901. With the deep HST image and spectroscopic redshift determined in this analysis, Muzzin et al. (in prep) determined a well-constrained lens model, which allowed them to accurately determine the circularized r_e (corrected for magnification) and n to be $0.86^{+0.19}_{-0.14}$ kpc and $3.50^{+0.68}_{-0.60}$.

5.2.2 Rest-Frame UVJ Colors

Williams et al. (2009) demonstrate that galaxies display a clear bi-modality in $U-V$ and $V-J$ color-space out to $z = 2$. Galaxies tend to separate into two sequences

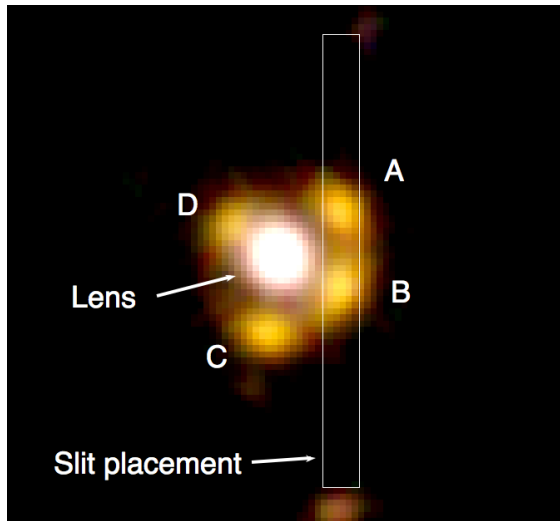


Figure 5.1 RGB-image using UltraVISTA Ks, H, and J-band DR2 images. The source images are labeled A, B, C, and D, and the foreground lens is indicated. The source images are noticeably redder than the lens because of the discordant redshifts ($z_{\text{lens}} = 0.960$ and $z_{\text{source}} = 2.76$) which result in the continuum emission from the lens and source galaxies peaking in different bands. The position of the X-Shooter slit on the sky is indicated. Note that the slit was placed such that it falls on galaxies A and B.

in color-color space, one consisting primarily of star forming galaxies, and one primarily consisting of quiescent galaxies. This bi-modality is driven by a galaxy’s UV+IR determined SFR. Beyond $z = 2$, measurement errors, and completeness limits reduces this bi-modality (Williams et al. 2009; Muzzin et al. 2013b).

We calculate the rest-frame $U-V$ and $V-J$ colors for *COSMOS* 0050+4901 using the photometric data presented in M12 (via *EAZY*; Brammer et al. 2008). We de-blending the lens from the images, which showed non-negligible contamination in the PSF-matched ground based imaging, by simultaneously fitting both the images and the lens using *GALFIT* (Peng et al. 2010) (further details may be found in M12).

In Fig. 5.2 we show that our object falls on the quiescent region in the UVJ diagram (using $z_{\text{spec}} = 2.756$; the determination of which is described in Sec. 5.3.1). We compare and contrast it to a quiescent, spectroscopic sample compilation (from van de Sande et al. 2015, with a redshift distribution of $0.6 < z < 2.2$). This sample contains 63 galaxies at $0.4 < z < 1.6$ from Bezanson et al. (2013), 38 galaxies at $1 < z < 1.4$ from Belli et al. (2014a), 18 galaxies at $0.6 < z < 1.1$ from van der Wel et al. (2005), 16 galaxies at $z \sim 0.8$ from Wuyts et al. (2004), 5 galaxies at $1.2 < z < 1.6$ from Newman et al. (2010), 4 galaxies at $1.4 < z < 2.1$ from van de Sande et al. (2013), 3 galaxies at $2.1 < z < 2.4$ from Belli et al. (2014b), 1

galaxy at $z = 2.2$ from van Dokkum et al. (2009), 1 galaxy at $z = 1.8$ from Onodera et al. (2012), and 1 galaxy at $z = 2.6$ from Newman et al. (2015) (see Table in van de Sande et al. 2015 for further details). As stated in van de Sande et al. (2015), the sample is selected based on the availability of kinematic measurements in the literature. Thus, this sample is biased towards brighter objects. In Fig. 5.2 we also indicate the UVJ color selection from van de Sande et al. (2015) as the dashed-black line.

Also plotted in grayscale in Fig. 5.2 is a redshift-selected ($1.5 < z < 2.5$), photometric sub-sample from the K-band selected catalog of UltraVISTA from Muzzin et al. (2013a) (with the limiting magnitude $K < 24.4$ in a $2.1''$ aperture). This sub-sample contains both star forming, and quiescent galaxies. The redshift range was chosen in order to highlight the color bi-modality, which as previously mentioned, is erased at higher redshifts due to incompleteness and measurement errors. In comparison to both the spectroscopic, and photometric samples, our object has colors similar to galaxies with quiescent populations.

5.2.3 Spectroscopic Data

Data were obtained using the X-Shooter instrument on the VLT UT2 (D’Odorico et al. 2006; Vernet et al. 2011) with the K-band blocking filter in place. The target was observed in service mode; the observations were carried out between 2012 December and 2014 February (program Muzzin 090.B-0452(A), and DDT program Muzzin 288.B-5043(A)). All observations had clear sky conditions and an average seeing of $0.8''$. A $0.9''$ slit was used in the NIR, aligned in the North-South direction with two of the images on the slit, as shown in the UltraVISTA color image in Fig. 5.1. X-Shooter simultaneously takes spectra in the observed UVB and VIS. The UVB and VIS arm data had no signal, as expected from the very red SED.

The NIR sky changes on short timescales (\sim minutes) and to compensate for changing sky levels, it is customary to perform a nodding pattern, with two frames adjacent in time subtracted from each other with the object offset in adjacent frames, often referred to as an ABBA observing pattern. Given the size of the X-Shooter slit ($0.9'' \times 11''$), the spatial extent of our object was such that there was insufficient space to perform this nodding pattern with enough empty sky for a successful sky subtraction. As such, observing blocks were 10 minutes, with a nodding pattern offset in declination in $0.4''$ increments to a maximum offset of $2''$ which corresponds to a shift on the slit of between 2 and 10 pixels. These offsets were made for the identification and removal of bad pixels.

The images were reduced using the method most commonly used in optical spectroscopy (see Section 5.2.4). Of 64 science frames with 600s exposure of exposure time on each frame, 5 frames did not contain the target and were thus not used in the final combination (but utilized in sky subtraction - see Section 5.2.4). This results in a science image with a total exposure time of 9.8hrs. However, obtaining a similar S/N spectrum on a single galaxy with comparable un-lensed magnitude ($K \sim 22.7$) would require 215 hours when accounting for the fact that our observations are sky-limited, 2 objects fall on the slit and that we are only

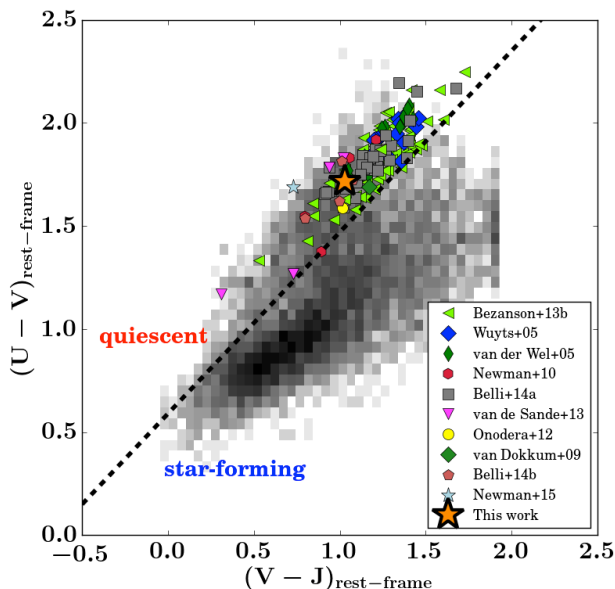


Figure 5.2 Rest-frame $U-V$ color vs $V-J$ color. Grey points are a redshift selected ($1.5 < z < 2.5$) comparison sample from the K_s -band selected UVISTA catalog (McCracken et al. 2012). The black dashed line is the colour selection implemented by van de Sande et al. (2015) to separate quiescent and star forming galaxies. Coloured points are a high redshift ($0.6 < z < 2.3$) sample compiled by van de Sande et al. (2015), with the literature sources indicated in the plot legend. Our object (orange star) sits on the UVISTA $1.5 < z < 2.5$ red sequence, and within the locus of other high redshift, quiescent galaxies with measured stellar velocity dispersions.

semi-resolved. This gain in S/N demonstrates the substantial observing advantage provided by strong gravitational lensing. Additionally, a B9V telluric standard star (Hipparcos 049704) was also observed before and after the science target for removal of atmospheric absorption lines, as well as relative flux calibration between orders.

5.2.4 Spectroscopic Reduction

The data were reduced with the ESO pipeline for X-Shooter (ver 3.10; Modigliani et al. 2010), following the “physical” mode reduction chain using EsoRex. Individual frames were reduced in stare mode, as the extent of the object on the slit made standard sky subtraction difficult. Bad-pixel masks were generated using IRAF task *ccd_mask*, and bad-pixels corrected for using the IRAF task *fixpix*.

Because of the methodology of our sky subtraction, we found several detector artefacts on the images which complicated this procedure. In order to subtract these artefacts, we generated a sky frame out of 5 blank sky frames from our observations, as well as other 10 min exposures which used the K-band blocking filter found in the X-Shooter archive. We used a total of 28 frames. These frames were all median combined to generate a high S/N sky-frame. This sky-frame was then subtracted from the science frames to subtract the detector artefacts.

The OH-emission lines in the NIR vary in flux, and change on short time scales, so the sky-frame subtraction could not account for sky lines. To account for this, the sky was modelled along each column in the spatial direction, while masking out rows which contained galaxy flux. This modelled sky was then subtracted from each column. The individual exposures were then median combined order by order.

The telluric standard spectra were reduced in the same way as the science frames. We constructed a response spectrum from the telluric star, and a black body curve with a T_{eff} matching a B9V star. Residuals from Balmer absorption in the telluric standard were removed by interpolation. The science observations were corrected for instrumental response and atmospheric absorption by division of the response spectrum.

To extract the spectrum, a 1D light profile was fit to each wavelength pixel (or column) along the spatial direction. The light profile was modelled from a median combination of all these fitted profiles from an order in the H-band (the highest S/N region of our spectrum). Order number 17 is shown in Fig 5.3 to illustrate. The light profile found in the top panel of Fig. 5.3 was fit, with a background term, to each column of the combined, 2D spectrum:

$$c_\lambda = a_\lambda P_y + b_\lambda \quad (5.1)$$

λ and y refer to the spatial and spectral dimensions. c_λ refers to the column, P_y is the double peaked profile fit to each column, a_λ and b_λ are the fitted coefficients. a_λ is effectively the 1D spectrum, and b_λ is the background term (see 4th and 5th panels in Fig.5.3). The error spectrum (bottom panel of Fig. 5.3) is the covariance of the fit, using the 1σ value of the pixels at each location. Skylines and bad columns were flagged using an error cutoff (above which the columns would be rejected).

The low-resolution spectrum was constructed by binning the 1D spectrum in the wavelength direction, using a bi-weight mean (as described in van de Sande et al. 2013) with a bin size of 10 good pixels. We show the spectrum, along with photometry and best fit BC03 model in Fig. 5.4, and 5.5.

5.3 Structural Properties and Stellar Populations

5.3.1 Redshift Determination

A spectroscopic redshift was measured using FAST (Kriek et al. 2009), an IDL-based fitting routine which fits stellar population synthesis models to photometry/spectra.

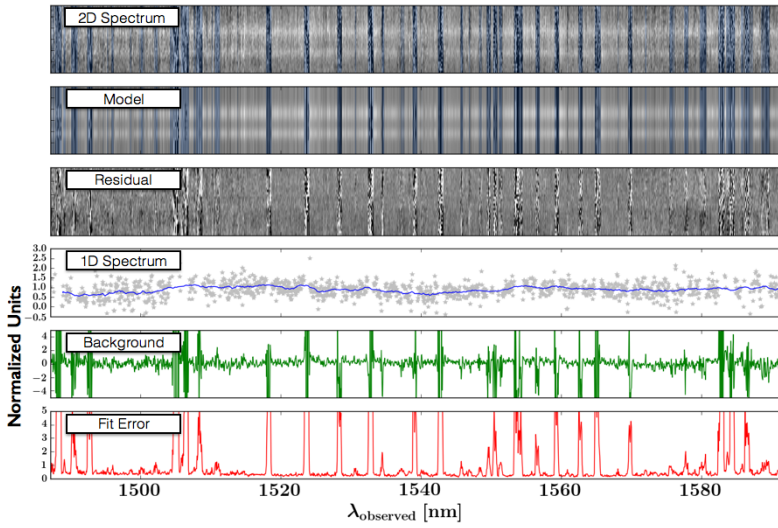


Figure 5.3 Above is an example of our prescription for column rejection and spectral extraction. From top to bottom: **(1)** The median combined 2D spectrum **(2)** The model reconstruction from the double gaussian fitting as described in “Spectroscopic Reduction” **(3)** The residuals of (1) and (2) **(4)** The coefficient of the relative strength of the double-peak profile (effectively the extracted 1D spectrum with normalized units) **(5)** The coefficient of the background term **(6)** The relative error from the fit. The columns are rejected above a specified ‘Fit Error’ which varied with each spectral order. The blue shaded regions in (1) and (2) are the columns which are rejected.

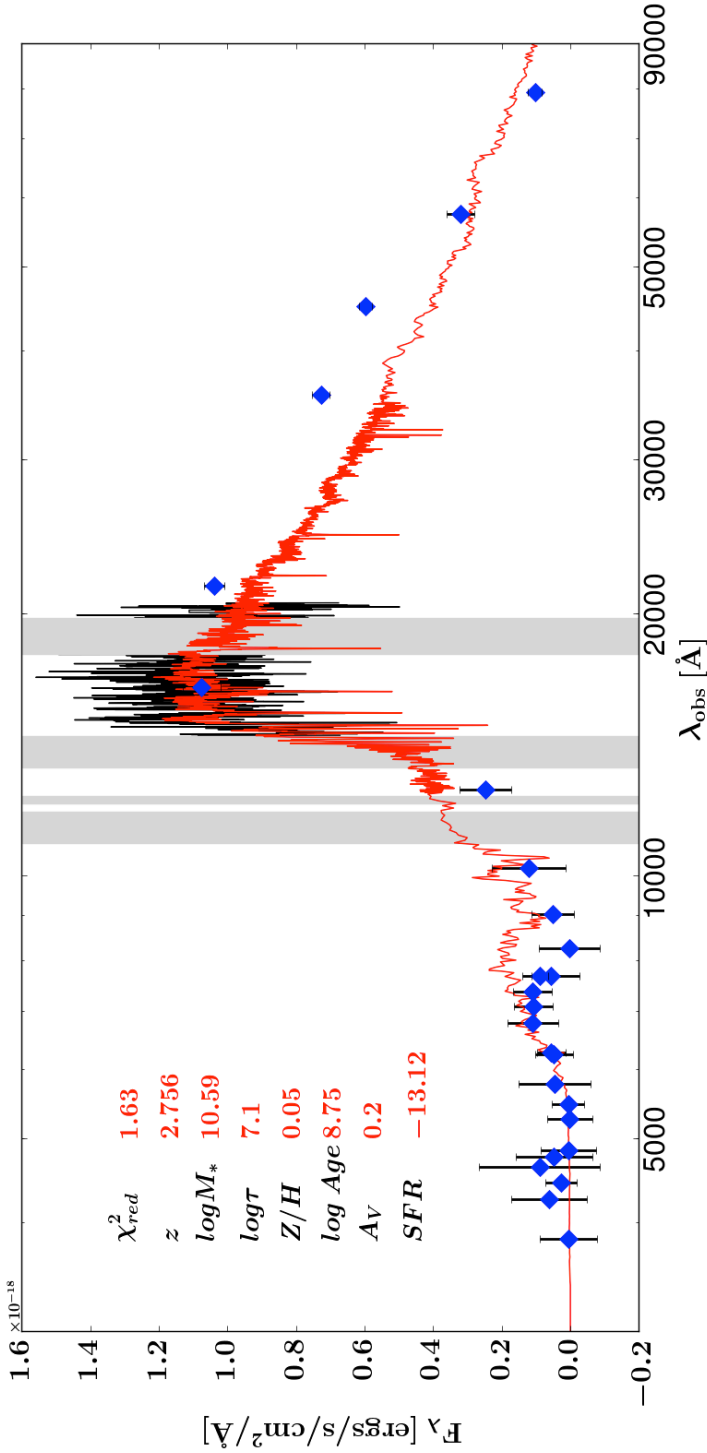


Figure 5.4 Best-fit FAST BC03 template (red-line) with photometry (blue points) and H-band X-Shooter spectrum (black-line). Grey regions indicate strong atmospheric absorption resulting in low S/N spectra. The J-band spectrum was omitted due to contamination from the lensing galaxy (see text for further discussion). Best-fit stellar population parameters and their 68% confidence intervals can be found in Table 5.1.

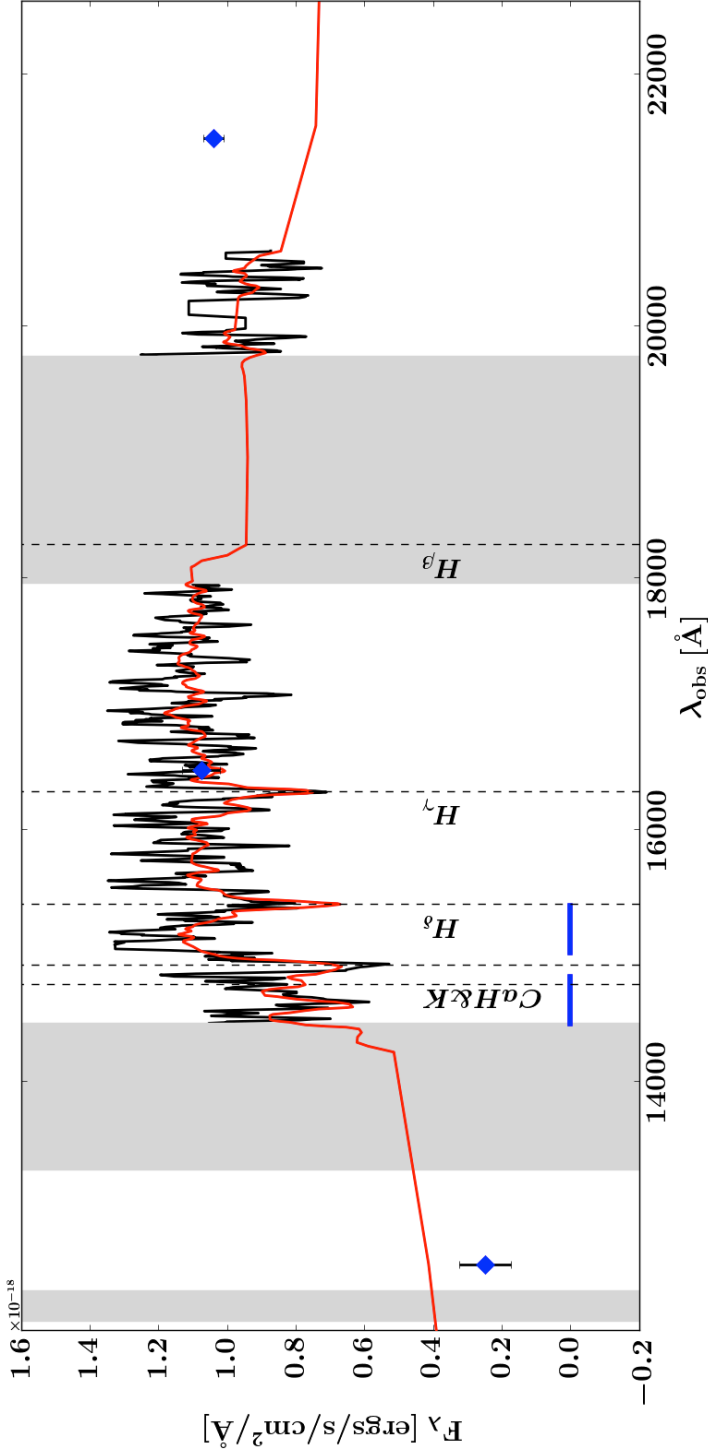


Figure 5.5 Similar to Fig. 5.4, but with the wavelength range restricted to the H-band, and the location of prominent absorption lines indicated. The fitted spectrum was smoothed using a bi-weight mean with a bin size of 10 good points (i.e. those that were not rejected by our criteria described in Sec. 2.3). The spectrum shown above has been smoothed to better illustrate the presence of absorption lines.

This fitting is described in more detail in Section 5.3.2.

Our best-fit redshift is $z_{\text{spec}} = 2.756 \pm 0.001$. This is a high-confidence measurement, as numerous absorption lines, such as Ca H&K, H δ , and H γ are detected. Notably, the difference between the photometric ($z_{\text{phot}} = 2.4 \pm 0.13$) and spectroscopic redshift ($z_{\text{spec}} = 2.756 \pm 0.001$) is more than twice the uncertainty on the photometric redshift. The possible explanations for this discrepancy are discussed below.

The difference between the z_{spec} and z_{phot} might originate from mistaking the 4000Å-break and Balmer-break. The 4000Å-break and Balmer-break ($\sim 3640\text{Å}$) are two continuum features which are difficult to resolve in photometric datasets due to their proximity in wavelength. Both continuum features result in a color differential between each side of the 4000Å/3650Å spectral region, the strength of which correlates with age in both cases. They do, however, originate from different physical processes, and thus *how* they correlate with age is different. The 4000Å break is a result of absorption by ionized metals which is strongest in older and high-metallicity stellar populations. The Balmer-break marks the limit of the Balmer series and blending of higher order Balmer lines, and is strongest in A-stars. The strength of the Balmer-break monotonically increases before peaking at intermediate ages ($\sim 0.5 - 1$ Gyr) when the stellar light is dominated by A-stars.

Both these features can be prominent in the continuum of quiescent galaxies, and fall into the NIR between $1.5 < z < 3$. The discrepancy between the z_{phot} and z_{spec} determination is likely caused by a combination of wavelength gaps between the transmission curves in the NIR bands (J,H, and K_s), as well as wide bandwidth in the same filters. This results in a J-H color appropriately explained by either the presence of the 4000Å-break at lower z , or the Balmer-break at higher z .

This uncertainty associated with the breaks falling between the NIR filters likely caused the fitting confusion between a quiescent galaxy with a prominent 4000 Å break at $z = 2.4$, and a post-SB galaxy with a 3650 Å Balmer-break at $z = 2.8$. This illustrates the challenges of using z_{phot} only. This issue is well-known, and that even with high S/N NIR photometry, photometric redshifts at $z > 2$ can be uncertain due to these issues. This has led to the use of NIR “medium bands” as in the NEWFIRM Medium Band Survey (Whitaker et al. 2011) and zFOURGE Survey (Straatman et al. 2014) to provide improved photometric redshifts for galaxies where the Balmer and 4000Å-breaks fall in the observed NIR.

This redshift difference is large enough that it changes the stellar population parameters by M12 at a level that is larger than the quoted uncertainties in that paper, particularly the stellar mass, age, and dust content. In the next section we present revised values for these parameters using the spectroscopic redshift.

5.3.2 Stellar Population Properties

Stellar population properties are estimated using FAST (Kriek et al. 2009). We used Bruzual & Charlot (2003) templates, with a delayed, exponentially declining star formation history (with timescale τ), a Chabrier (2003) IMF, and Calzetti et al. (2000) dust law.

We have simultaneously fit both the photometry and H-band spectrum. We

have omitted the J-band spectrum but include the J-band photometry. The spectrum in the J-band is very low S/N as the flux from the lens peaks in the J-band (see Fig. 4 of M12). The image and lens are spatially close with contamination affecting the continuum strength. The best-fit parameters are summarized in Table 5.1. The best-fit stellar population parameters provide a best-fit FAST age $\log \text{Age}/\text{yr} = 8.75^{+0.07}_{-0.07}$, stellar-mass $\log M_*/M_\odot = 10.59^{+0.04}_{-0.05}$ (corrected for lensing), and $A_V = 0.2^{+0.26}_{-0.20}$. This galaxy appears post-starburst, and is striking in that even at $z = 2.8$, intermediate-mass galaxies with quiescent stellar populations exist.

Muzzin et al. (2013b) suggests that the quenched fraction for galaxies of $\log M_*/M_\odot > 10.8$ is $\sim 20\%$ at these redshifts. The identification of galaxies with quiescent populations in Muzzin et al. (2013b) is based on rest-frame color selection and z_{phot} . Here we confirm unambiguously through spectroscopy that these galaxies do exist at these redshifts.

Compared to the values of M12, the effects of fitting the spectrum and photometry with the spectroscopic redshift result in a best-fit where the age changes from $\log \text{Age}/\text{yr} = 9.0^{+0.2}_{-0.2}$ to $\log \text{Age}/\text{yr} = 8.75^{+0.07}_{-0.07}$, stellar-mass from $\log M_*/M_\odot = 10.82^{+0.05}_{-0.07}$ to $\log M_*/M_\odot = 10.59^{+0.04}_{-0.05}$, and dust from $A_V = 0.9^{+0.2}_{-0.6}$ to $A_V = 0.2^{+0.26}_{-0.20}$. It is important to note that these values do not agree (within the 1σ errors) with the values reported by M12. However M12 underestimated the uncertainties associated with the z_{phot} , leaving a deficit in the error budget resulting in a disagreement of values. With the addition of a z_{spec} , the best-fit galaxy is younger, less massive, and contains less dust than previously determined by M12.

In order to understand the differences in best-fit stellar population parameters between M12 and the present study, we re-fit the data using the photometry and the spectroscopic redshift (omitting the spectra). This produced a different set of parameters from our best-fit and closer to the age, mass and dust content of M12, suggesting that the spectrum does drive the fit. We conclude that both the spectroscopic redshift and the spectrum itself, which shows strong Balmer absorption, drive the changes in the stellar populations.

We note that in Fig. 5.4, it is clear that our best-fit to the photometry and spectroscopy is not ideal. The most striking mismatch occurs in the IRAC bands. The disagreement between the spectrum and photometry in the far-infrared could be attributed to the challenges associated with de-blending the source from the lens, and the lens images from one another. In the IRAC bands, the FWHM of the PSF becomes comparable to the separation between source galaxies and the lens which is $2''$ for this system. Accurately separating the flux becomes more difficult than in the observed optical and NIR where the PSF is smaller. We ascertained the effect of the IRAC bands on the fit by re-fitting the spectrum and photometry without IRAC. We found the stellar population parameters to be the same within 1σ and conclude that the IRAC bands do not strongly influence the outcome of the fitting. The current analysis now includes age sensitive absorption features (see below), as well as the new spectroscopic redshift, and therefore we are confident in the stellar population parameters and associated uncertainties determined in this study.

In Fig. 5.5, we find a weak or absent Ca K absorption in the data, whereas the model suggests a stronger absorption line. The observed wavelength of Ca K

Table 5.1. Stellar Population Synthesis Properties

Z	z_{spec}	$\log \tau$ (yr)	$\log \text{Age}$ (yr)	A_v (mag)	$\log M_*$ (M_\odot)	$\log \text{SFR}^*$ ($M_\odot \text{ yr}^{-1}$)	$\log \text{sSFR}$ (yr^{-1})	χ^2_{red}
0.050	$2.756^{[2.757]}_{[2.755]}$	$7.1^{[7.63]}_{[7.00]}$	$8.75^{[8.82]}_{[8.68]}$	$0.2^{[0.46]}_{[0.0]}$	$10.59^{[10.63]}_{[10.54]}$ (11.25) [*]	$-13.12^{[-2.4]}_{[-17.52]}$ (-12.46) [*]	$-23.71^{[-13.00]}_{[-28.07]}$	1.63

*This is from the 30-band SED fit with a τ -model star formation history, and is effectively a UV-dust-corrected SFR.

**FAST output before adjusting for lensing magnification

Note. — The best-fit FAST parameters and their values within 68% confidence intervals, adjusted for the lensing magnification (where appropriate) from Muzzin et al. 2012

at $z=2.756$ is 4780 \AA which overlaps with a strong sky-line at 14793 \AA leading to poor spectral extraction in that region. Thus, the mismatch between the data and model Ca K absorption strength is likely caused by poor data quality in that region. We note that regions affected by strong skylines have larger errors, and will therefore have lower weight in the full spectral fitting.

In addition to the stellar population parameters fit with FAST, we measured the Lick index $H\delta_A$ (Worthey & Ottaviani 1997) and $D_n(4000)$ (Balogh et al. 1999) break, which are features shown to be sensitive to age (Kauffmann et al. 2003). With an $H\delta_A$ measurement from our spectrum, as well as coverage of the 4000 \AA break (as seen by the blue horizontal bars in Fig. 5.5), we are able to independently verify our model age determination. This independent age verification from the absorption features is important because of inherent degeneracies in fitting the SED. In Fig. 5.6, we have plotted $H\delta_A$ as a function of $D_n(4000)$ of our object, as well as a random sample of SDSS galaxies which contain both star-forming and quiescent galaxies.

Over-plotted in Fig. 5.6 are three different model tracks generated using GALAXEV (Bruzual & Charlot 2003). The best-fit super-solar metallicity of $Z = 0.05$ from FAST was used in each model track. Two fiducial models (a burst, and constant star formation history) are plotted in blue and magenta to highlight the extremes in the parameter space. A model with a delayed exponential SFH is also plotted in red, using the best-fit parameters from Table 5.1. The red point corresponds to the age of our best fit using FAST. The separation between the $H\delta_A$ vs. $D_n(4000)$ determined age and FAST modelled best-fit age is small, confirming the FAST best-fit age in a model independent way. Fig. 5.6 also shows very little difference in the τ vs. delayed- τ models, and that the star formation history is dominated by a population which is consistent with a single burst. From Fig. 5.6, we confirm that this galaxy is indeed relatively young, post-starburst, and consistent with being recently quenched.

5.3.3 MIPS 24 μm Photometry

As described in Sec. 5.3 of M12, there is corresponding MIPS 24 μm data which was remarked upon. We briefly summarize their findings. They detected observed-frame 24 μm emission at 4σ in the vicinity of the lens system. However, they found the MIPS source to be offset to the south-west by several arcseconds which suggests that the lens system is not the correct counterpart. Under the possibility that the MIPS detection *is* coincident with the lens-source system, M12 determined an estimate of the sSFR. Since the FWHM of the PSF is $5.5''$, individual sources could not be resolved in MIPS. Photometry was therefore performed in a $7''$ aperture which surrounded the entire lens system. For the source and lens, at $z_{\text{phot}} = 2.4$, they find $\log \text{sSFR} = -9.93^{+0.20}_{-0.20}$ which is below the star-forming main sequence for their derived stellar mass at $z_{\text{phot}} = 2.4$. Thus, even in the scenario where all of the MIPS emission is associated with the lensed galaxies, they would still be classified as quiescent.

The new z_{spec} determination will effect the sSFR found by M12, which we recalculate below. We follow the same procedure to find a total un-lensed mass of the source galaxies of $\log M_*/M_\odot = 11.56^{+0.08}_{-0.04}$. With the photometry from M12, and the templates of Dale & Helou (2002), the implied un-lensed SFR is $370^{+96}_{-83} M_\odot/\text{yr}$. This yields a $\log \text{sSFR} = -8.99^{+0.12}_{-0.12}$. The sSFR of a star-forming main sequence galaxy is $\log \text{sSFR} \sim -8.6$ for $\log M_*/M_\odot = 10.59$ between $2.5 < z < 3.5$ (Schreiber et al. 2015). This implies that if the MIPS detection is associate with the lensed system, then this galaxy is only 0.3 dex below the star-forming main sequence. We find this implied level of star formation unlikely for two reasons. The first is that the MIPS and NIR sources are offset from one another, and the MIPS detection is not likely associated. The second is our model independent age determination via the strengths of $\text{H}\delta_A$ and $\text{D}_n(4000)$ (as seen in Fig. 5.6) which emphasize an older age for the majority of the stars in this galaxy.

If the MIPS detection were coincident then all star-formation would need to be dust-enshrouded, and very recent, so that no young stars are visible outside the birth-clouds. An alternative explanation is that the lens-source system could host an AGN, but we do not see emission lines in the near-IR or optical. Additionally, M12 looked for X-ray and radio detections in *XMM-Newton* and the Very Large Array observations of the COSMOS field and found no detection in the vicinity of the system.

5.3.4 Stellar Velocity Dispersion

The presence of strong absorption features provide us with the means to study the kinematics of this galaxy, and determine a stellar velocity dispersion. With this measurement, we are able to calculate the dynamical mass and place strong constraints on the baryonic contribution to the total mass budget. Although random errors on broadband photometry can be quite low with state-of-the-art instruments, systematic uncertainties in mass determinations are difficult to estimate accurately (Conroy et al. 2009). Thus, velocity dispersions are key for placing upper limits on the total mass of the system, and hence validating stellar mass estimates.

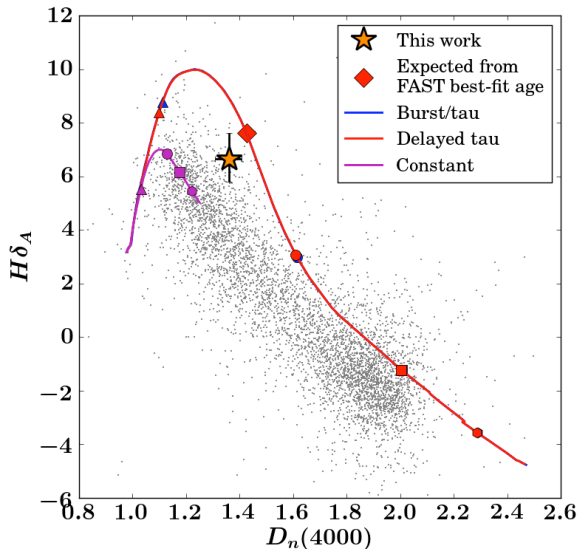


Figure 5.6 $H\delta_A$ as a function of $D_n(4000)$. Gray points are a random sample of SDSS galaxies. The orange star is the measurement from the H band spectroscopy. The solid, colored lines are different Bruzual & Charlot (2003) models with different SFH (burst, delayed exponential and constant) with the best fit values from Table 5.1 used as inputs. Different benchmark ages are indicated along each track with a triangle (0.1 Gyr), circle (1.0 Gyr), square (3.0 Gyr), and hexagon (10.0 Gyr). Marked on the delayed exponential SFH track (the model of choice from FAST), the best-fit age is indicated (red diamond). The close separation reaffirms our age determination.

A stellar velocity dispersion was estimated using Penalized Pixel-Fitting (pPXF) (Cappellari & Emsellem 2004). The spectrum was first resampled onto a logarithmic wavelength scale without interpolation, but with the masking of bad pixels. Template mismatch was accounted for by simultaneously fitting the continuum of the best-fit Bruzual & Charlot (2003) template with an additive polynomial, following the same analysis presented in Appendix 3 of van de Sande et al. (2013).

The effect of template choice can greatly affect the fitted velocity dispersion. We investigated the effect of template choice on the best-fit stellar velocity dispersion, in a similar manner to van de Sande et al. (2013). We fit the spectrum and photometry using FAST with a range of templates for a grid of fixed metallicity and ages. The allowable metallicities were $Z = 0.004$ (super sub-solar), 0.008 (sub-solar), 0.02 (solar) and 0.05 (super-solar). The age range considered was $\log \text{Age}/\text{yr} = 8.0 - 9.5$ in increments of 0.1 dex. We increased the resolution of the age grid to 0.05 dex between $\log \text{Age}/\text{yr} = 8.6 - 8.9$, as we found in previous fitting iterations that the FAST estimated 1σ -error was smaller than 0.1 dex.

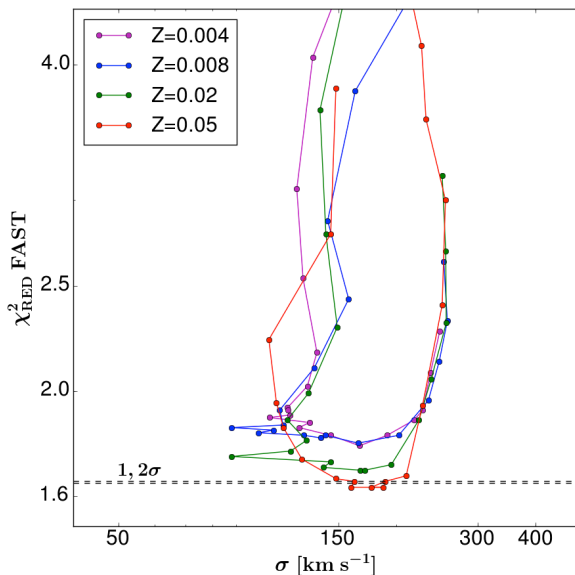


Figure 5.7 The pPXF best-fit stellar velocity dispersion plotted against the χ_{red}^2 output from FAST fitting both the spectrum and the photometry. Each point represents a different age (from $\log \text{Age}/\text{yr} = 8.0 - 9.5$), and each coloured ‘track’ a different metallicity. The horizontal dashed black lines are the 1σ and 2σ upper bounds from the Monte Carlo modelling of the best-fit template at $\log \text{Age}/\text{yr} = 8.75$. Points below these lines indicate templates that are statistically indistinguishable from each other. There are only three of these points, and they result in a stable stellar velocity dispersion implying that template choice is not the dominant source of uncertainty.

In Fig. 5.7, we show the χ_{red}^2 from FAST as a function of the best fit pPXF stellar velocity dispersion (corrected for template, $\sigma = 89 \text{ km/s}$, and instrument, $\sigma = 25 \text{ km/s}$, resolution). Using Monte-Carlo simulated errors, we determined 1 and 2 sigma limits on the χ_{red}^2 value of the best-fit FAST model (horizontal black dashed lines in Fig. 5.7). Points that fall below this line are statistically indistinguishable. We find a very narrow range of statistically indistinguishable templates, concluding that our error will be dominated by the formal errors of the fit, and not the template choice.

Accounting for instrumental and template resolution, as well as a rectangular aperture and seeing (see van de Sande et al. 2013), we find a best-fit pPXF stellar velocity dispersion of $\sigma = 187 \pm 43 \text{ km s}^{-1}$ (the error is the 68% confidence limits from the Monte-Carlo simulations).

From the assumption that the galaxy is virialized, we can determine the dy-

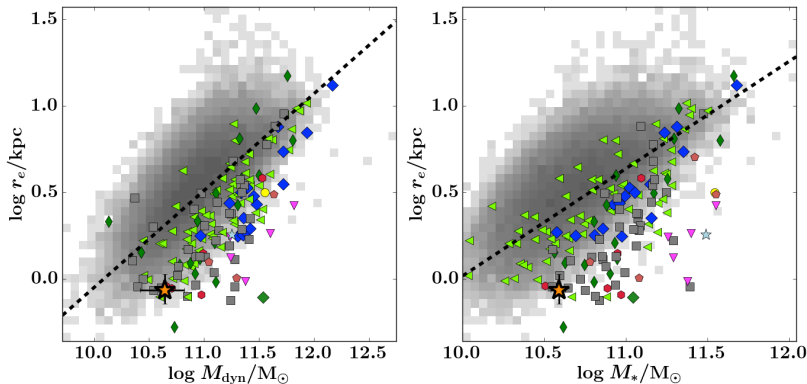


Figure 5.8 Left: The dynamical mass (M_{dyn}) versus r_e of the object of this study (orange star) plotted along side other high redshift objects compiled from van de Sande et al. 2015 where the colored symbols follow the same conventions as the legend in Fig. 5.2. The dashed black line is the parameterized mass-size relation of SDSS $z \sim 0$ quiescent galaxies, with the best fit parameters from van de Sande et al. 2011. Right: The same as the left plot, but with stellar mass instead of dynamical mass. In both instances, our object falls below the mass-size relation of $z \sim 0$ quiescent galaxies confirming compactness out to lower masses at high redshift.

namical mass as follows:

$$M_{\text{dyn}} = \frac{\beta(n)\sigma_e^2 r_e}{G} \quad (5.2)$$

Here G is the gravitational constant, and β is an expression as a function of the Sersic index, n , from Cappellari et al. (2006) (their equation 20):

$$\beta(n) = 8.87 - 0.831n + 0.0241n^2 \quad (5.3)$$

With $r_e = 0.86^{+0.19}_{-0.14}$ kpc and $3.50^{+0.68}_{-0.60}$ from Muzzin et al. (in prep), the dynamical mass is $\log M_{\text{dyn}}/M_{\odot} = 10.65^{+0.18}_{-0.23}$ which is quite similar to, but slightly above the derived stellar mass of $\log M_{*}/M_{\odot} = 10.59^{+0.04}_{-0.05}$.

Fig. 5.8 shows r_e as a function of stellar and dynamical mass for high and low- z galaxies with measured stellar velocity dispersions. Also included in Fig. 5.8 is the quiescent galaxy mass-size relation for $z \sim 0$ (dashed black line). In both stellar and dynamical mass we see that our galaxy is smaller than $z \sim 0$ galaxies at equivalent mass, and consistent with the higher-redshift quiescent population. This galaxy is indeed compact, which is well established for quiescent galaxies at these redshifts (see Sec. 5.1 and references therein).

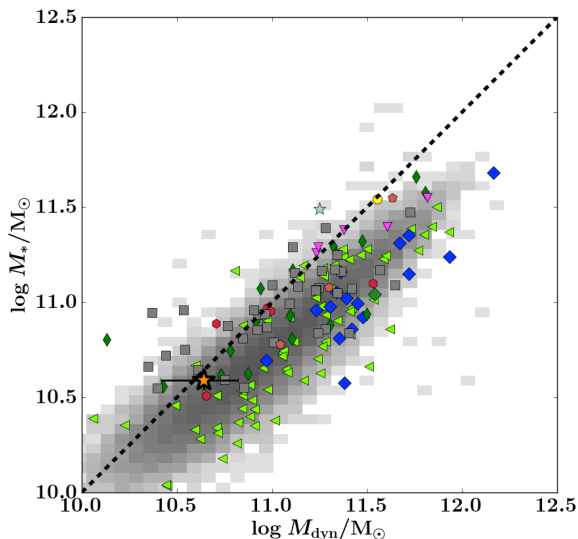


Figure 5.9 The dynamical (M_{dyn}) versus the stellar (M_*) mass of the object of this study (orange star) plotted along side other high-redshift objects compiled from van de Sande et al. 2015 where the colored symbols follow the same conventions as the legend in Fig. 5.2. The high- z objects are mass and colour selected. SDSS galaxies are the grey points (which have been colour selected with the same UVJ selection as found in Fig. 5.2), and the dashed black line is unity. For our object, the stellar mass and dynamical mass agree well.

Fig 5.9 shows the comparison between the FAST determined M_* , and the M_{dyn} . The black dashed line in Fig. 5.9 is unity - above this line is an ‘unphysical’ regime where the stellar mass exceeds the dynamical mass. From this figure, we see that the implied dark matter fraction appears to be very low, at least in the central regions of the galaxy where the bulk of the light is found (Fig. 5.8). However the error bars are large, and a dark matter fraction of 50% is also consistent with the data, therefore a definitive conclusion can not be drawn.

In Fig 5.10, we directly compare the total-to-stellar mass ratio (and thus, the dark matter fraction) as a function of redshift, where the mass fraction approaches unity (also seen in Fig. 5.9). This figure contains the same literature compilation of high- z quiescent galaxies with velocity dispersion measurements as found in Fig. 5.2. Of the known objects with a velocity dispersion, ours is at the highest redshift, and one of the lowest total-to-stellar mass ratios. There is also a weak trend, with quiescent galaxies becoming increasingly baryon dominated with redshift. This trend was also noted by van de Sande et al. (2013, 2015) whose sample extended out to $z = 2.3$, however between $z = 0$ and $z = 1.6$, Belli et al. (2014a) found no statistically significant evolution. This may suggest a rapid evolution

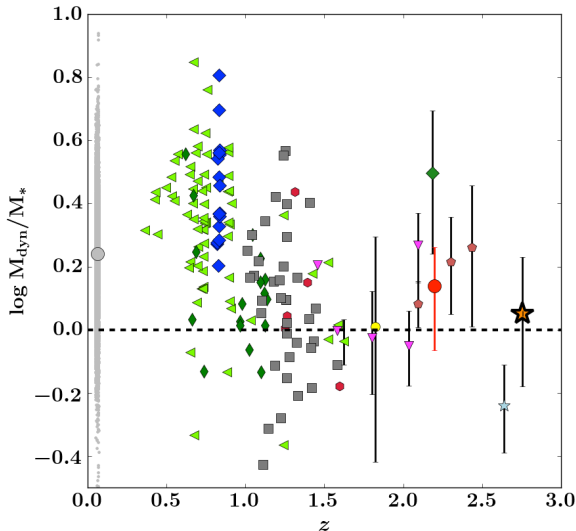


Figure 5.10 Redshift vs. ratio of dynamical to stellar masses of the color-selected sample compiled by van de Sande et al. (2015), and our object. Grey points are SDSS galaxies following the same color selection. The colored symbols follow the same conventions as the legend in Fig. 5.2. The grey circle is the average total-to-stellar mass ratio for SDSS galaxies. We note that the 68% confidence limit for the average total-to-stellar mass ratio for the SDSS galaxies is smaller than the grey symbol. The large red circle is the average total-to-stellar mass ratio for galaxies at $z > 1.6$ with 68% confidence limits. Our object is the highest redshift for which a dispersion has been measured.

between redshift $z \sim 3$ and $z \sim 1.6$. To test this, we compare the average total-to-stellar mass ratio of the SDSS sample to galaxies above redshift $z > 1.6$. In Fig. 5.10, we have indicated the SDSS median total-to-stellar mass ratio as grey circle. The average for galaxies above $z > 1.6$ is indicated by the red symbol with the 68% confidence interval. From Fig. 5.10, we see that galaxies at $z > 1.6$ do have a lower total-to-stellar mass ratio consistent with the findings of van de Sande et al. (2013, 2015), however the average value for the SDSS galaxies and those above $z > 1.6$ are not statistically different (i.e. they fall within the 2.5σ uncertainty).

5.3.5 Mass Fundamental Plane

Given a stellar mass, a precisely determined r_e , and our stellar velocity dispersion measurement, we are able to tentatively explore the MFP to $z \sim 3$, as well as lower masses. The most salient difference between the FP and MFP with regards to

evolution with redshift is the zero-point. Although the zero-point of the traditional luminosity FP is shown to evolve with redshift (e.g van Dokkum & Franx 1996; van Dokkum et al. 1998; Treu et al. 1999, 2001), the MFP does not (Bolton et al. 2008; Holden et al. 2010; Bezanson et al. 2013). The evolution of the zero-point of the FP can be used to investigate the luminosity evolution of quiescent galaxies, whereas the zero-point evolution in the MFP can be used to investigate the corresponding structural and dynamical evolution (Bezanson et al. 2013).

Strikingly, Bezanson et al. (2013) established that the zero-point of the MFP does not evolve significantly with redshift, in spite of evolution in the structure and size of quiescent galaxies since $z \sim 2$ (see Sec. 5.1 and references therein). One outstanding question is whether this trend holds to higher redshifts and lower mass. With this data, we are able to explore both issues simultaneously.

In Fig. 5.11 we compare our measurement to galaxies at the highest available redshifts which have velocity dispersions. We applied a redshift cut to the literature compilation of van de Sande et al. (2015) of $z > 2$, which left only 5 galaxies (where the highest spectroscopic redshift is $z_{\text{spec}} = 2.636$) for comparison. Fig. 5.11 shows that, within measurement uncertainty, our galaxy lies on the same MFP as galaxies at $z \sim 2$. This coherence between $z \sim 2$ and $z \sim 3$ suggests that the MFP evolves very little between these epochs. Further data at these redshifts are required for a definitive conclusion.

5.4 Discussion and Conclusions

We have obtained an X-Shooter VLT spectrum of the multiply imaged lensed galaxy COSMOS 0050+4901 found serendipitously in the UltraVISTA field. The lensing of this quiescent galaxy was fortunate, providing a detailed, 'sneak-peak' at the universe during an exciting time. In order to obtain a spectrum with equivalent S/N, without the magnifying effects of gravitational-lensing, 215 hours of integration time on a 10m class telescope would have been required. The existence of only a handful of gravitationally-lensed, quiescent galaxies (Auger et al. 2011; Geier et al. 2013; Newman et al. 2015) highlights the rarity of these objects, and the opportunity they provide to study the high- z , intermediate-mass mass universe preceding the era of JWST.

At $z_{\text{spec}} = 2.756 \pm 0.001$, COSMOS 0050+4901 is one of the highest-redshift quiescent galaxies with a spectroscopic redshift, as well as the highest-redshift galaxy with a measured velocity dispersion ($\sigma = 187 \pm 43 \text{ km s}^{-1}$). With this spectrum we have detected a suite of Balmer lines (H γ , H δ), and the CaH&K absorption lines in the observed H-band (Fig. 5.5). The detection of multiple absorption lines provides tight constraints on z_{spec} , and is additionally indicative of the presence of older stellar populations. Within the wavelength covered by the spectrum, we find no evidence of emission lines. With our spectrum, the understanding of the stellar populations of this galaxy change from an older ($\log \text{Age/yr} = 9.0^{+0.2}_{-0.2}$), massive ($\log M_*/M_\odot = 10.82^{+0.05}_{-0.07}$), dusty ($A_V = 0.9^{+0.2}_{-0.6}$) galaxy (as found by M12) to a younger ($\log \text{Age/yr} = 8.75^{+0.07}_{-0.07}$), post-starburst galaxy of intermediate mass ($\log M_*/M_\odot = 10.59^{+0.04}_{-0.05}$).

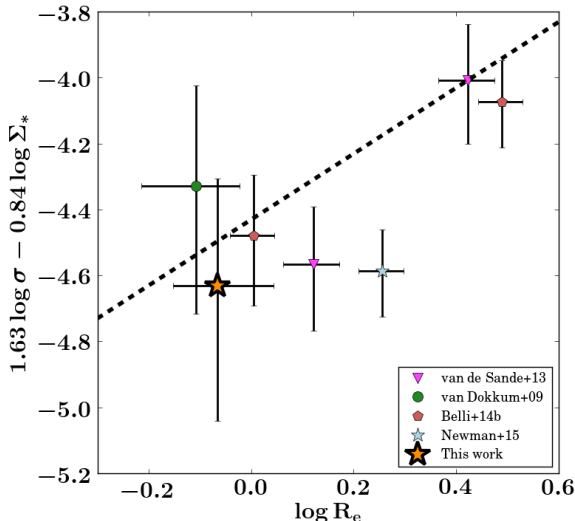


Figure 5.11 The mass fundamental plane for galaxies at redshift $z > 2$. Symbols are as per the previous figures. The black dashed line is the best-fit mass FP between $1.5 < z < 2.2$ from Bezanson et al. 2013. Our galaxy is within the variance of the galaxies at $z > 2$ around the mass fundamental plane suggesting it is in place at lower masses.

This new age determination is supported by spectral diagnostics such as the $D_n(4000)$ (Balogh et al. 1999), and the Lick index $H\delta_A$ (Worthey & Ottaviani 1997) which have been shown to be sensitive to age (Kauffmann et al. 2003). In Fig. 5.6, we show how the aforementioned spectral diagnostics reaffirm the younger age determination of this study in a model independent way. Equipped with this best-fit age, the rest-frame optical colors (Fig. 5.2), and star formation rate from stellar population modelling (Fig. 5.4) we confirm that intermediate-mass galaxies which halt in-situ star formation are in place by $z \sim 3$.

In addition to the brightening effects of the magnification, the magnifying effects also increase spatial resolution. With this increase in resolution, accurate structural parameters are determined. Muzzin et al. (in prep) modelled the gravitationally lensed system and determined the magnification, as well as the surface brightness profile, measuring a sersic index of $3.50^{+0.68}_{-0.60}$ and an $r_e = 0.86^{+0.19}_{-0.14}$ kpc. The right-hand panel of Fig. 5.8 shows the precise r_e measurement of Muzzin et al. (in prep) as a function of the stellar mass. Over-plotted for comparison are a local, and high-redshift sample. Like the high-redshift sample, our object falls below the local size-mass relation (Shen et al. 2003). We confirm, with a high degree of precision, that this galaxy is compact, which is consistent with what is seen for quiescent galaxies at $z \sim 2$ (e.g., Daddi et al. 2005; Trujillo et al. 2006;

Zirm et al. 2007; van Dokkum et al. 2008; Szomoru et al. 2012).

Spectroscopy also allows for a kinematic determination of the mass. The measurement of a dynamical mass is important, as it provides a direct, kinematic method of probing the total matter content of a galaxy, without the uncertainties and prior assumptions associated with parameters such as distance measurement, IMF, and dust content (i.e Conroy et al. 2009 places the uncertainty associated with stellar mass estimates to be 0.6 dex at $z \sim 2$). With the dynamical mass we are able to place a strict upper limit on the baryonic contribution to the total mass of the galaxy. In Fig. 5.9 we compare the two measurements, and find the stellar and dynamical masses to be consistent with each other, although our results suggest either a low dark matter fraction in the inner kpc of the galaxy, where the bulk of the light is found, or perhaps that the stellar mass content is overestimated within the parameters discussed by Conroy et al. (2009) (such as assumptions about the IMF, dust content). However, Fig. 5.6 shows, via the $H\delta_A$ and D_n4000 indices, a model independent estimation of the age of this object. This result implies consistency in the model choice.

With a kinematic determination of the mass, and accurately measured structural parameters (r_e , and the Sersic index n), we are able to place COSMOS 0050+4901 on the MFP (Fig. 5.11). It is well established that local, quiescent galaxies fall on a FP described by surface brightness, size and stellar velocity dispersion (Dressler et al. 1987; Djorgovski & Davis 1987), which is tilted with respect to the prediction from virial equilibrium. This tilt does not evolve significantly, but there is an offset in the plane which becomes larger towards higher redshifts (e.g van Dokkum & Franx 1996; van Dokkum et al. 1998; Treu et al. 1999, 2001) as a result of the luminosity evolution of these galaxies with cosmic time. When replacing the surface brightness with stellar mass density (i.e. the MFP), Bezanson et al. (2013) found that this offset does not evolve significantly and these galaxies fall on the same MFP out to $z \sim 2$. In Fig. 5.11 we compare the object in this study to the highest redshift galaxies available with a velocity dispersion measurement. We show that out to $z \sim 3$ quiescent galaxies fall on the same MFP, and that little evolution takes place between $z \sim 3$ and the present day.

A dynamical mass additionally enables the investigation of dark-matter content in the central regions of this galaxy. In Fig. 5.10, we have plotted the total-to-stellar mass ratio as a function of redshift, which shows evidence of a trend to decreasing values. However this trend is not statistically significant, as the uncertainties on the dynamical mass at high- z are large. More spectra of these types of objects are required to make a statistically significant claim. If this ratio is low, it is what is expected in the case of a gas-rich, major merger (Robertson et al. 2006; Hopkins et al. 2009), which implies that this galaxy could represent the first generation of quiescent galaxies in the hierarchical merging scenario (White & Rees 1978), making this redshift epoch an exciting prospect for study.

This case study stands as a proof of concept of the utility of lensed, red galaxies in studying the population of passive galaxies down to lower masses as well as to higher redshifts. This paper also illustrates that few rest-frame optical spectra of quiescent galaxies exist beyond $z > 2$, and even fewer of galaxies at intermediate mass. We stress the need for further spectra of passive galaxies at higher-redshift,

as well as to lower masses, as this parameter space is still under-explored.

5.5 Acknowledgments

This research has made use of NASA's Astrophysics Data System. The authors also wish to thank the anonymous referee who's suggestions improved the presentation, and overall clarity of this paper.

References

- Auger, M. W., Treu, T., Brewer, B. J., & Marshall, P. J. 2011, *MNRAS*, 411, L6
- Balogh, M. L., Morris, S. L., Yee, H. K. C., Carlberg, R. G., & Ellingson, E. 1999, *ApJ*, 527, 54
- Belli, S., Newman, A. B., & Ellis, R. S. 2014a, *ApJ*, 783, 117
- Belli, S., Newman, A. B., Ellis, R. S., & Konidaris, N. P. 2014b, *ApJL*, 788, L29
- Bernardi, M., Sheth, R. K., Annis, J., et al. 2003, *AJ*, 125, 1866
- Bezanson, R., van Dokkum, P. G., van de Sande, J., et al. 2013, *ApJL*, 779, L21
- Bolton, A. S., Burles, S., Treu, T., Koopmans, L. V. E., & Moustakas, L. A. 2007, *ApJL*, 665, L105
- Bolton, A. S., Treu, T., Koopmans, L. V. E., et al. 2008, *ApJ*, 684, 248
- Brammer, G. B., van Dokkum, P. G., & Coppi, P. 2008, *ApJ*, 686, 1503
- Brammer, G. B., Sánchez-Janssen, R., Labbé, I., et al. 2012, *ApJL*, 758, L17
- Bruzual, G., & Charlot, S. 2003, *MNRAS*, 344, 1000
- Busarello, G., Capaccioli, M., Capozziello, S., Longo, G., & Puddu, E. 1997, *A&A*, 320, 415
- Calzetti, D., Armus, L., Bohlin, R. C., et al. 2000, *ApJ*, 533, 682
- Capelato, H. V., de Carvalho, R. R., & Carlberg, R. G. 1995, *ApJ*, 451, 525
- Cappellari, M., & Emsellem, E. 2004, *PASP*, 116, 138
- Cappellari, M., Bacon, R., Bureau, M., et al. 2006, *MNRAS*, 366, 1126
- Cappellari, M., Scott, N., Alatalo, K., et al. 2013, *MNRAS*, 432, 1709
- Chabrier, G. 2003, *PASP*, 115, 763
- Conroy, C., Gunn, J. E., & White, M. 2009, *ApJ*, 699, 486
- Daddi, E., Renzini, A., Pirzkal, N., et al. 2005, *ApJ*, 626, 680
- Dale, D. A., & Helou, G. 2002, *ApJ*, 576, 159
- Djorgovski, S., & Davis, M. 1987, *ApJ*, 313, 59
- D'Odorico, S., Dekker, H., Mazzoleni, R., et al. 2006, in *Society of Photo-Optical Instrumentation Engineers (SPIE) Conference Series*, Vol. 6269, *Society of Photo-Optical Instrumentation Engineers (SPIE) Conference Series*, 33
- Dressler, A., Lynden-Bell, D., Burstein, D., et al. 1987, *ApJ*, 313, 42
- Franx, M., Labbé, I., Rudnick, G., et al. 2003, *ApJL*, 587, L79
- Geier, S., Richard, J., Man, A. W. S., et al. 2013, *ApJ*, 777, 87
- Holden, B. P., van der Wel, A., Kelson, D. D., Franx, M., & Illingworth, G. D. 2010, *ApJ*, 724, 714
- Hopkins, P. F., Cox, T. J., Dutta, S. N., et al. 2009, *ApJS*, 181, 135
- Ilbert, O., McCracken, H. J., Le Fèvre, O., et al. 2013, *A&A*, 556, A55

- Kauffmann, G., Heckman, T. M., White, S. D. M., et al. 2003, *MNRAS*, 341, 33
- Kriek, M., van Dokkum, P. G., Labbé, I., et al. 2009, *ApJ*, 700, 221
- Kriek, M., van Dokkum, P. G., Franx, M., et al. 2006, *ApJ*, 645, 44
- Labbé, I., Huang, J., Franx, M., et al. 2005, *ApJL*, 624, L81
- McCracken, H. J., Milvang-Jensen, B., Dunlop, J., et al. 2012, *A&A*, 544, A156
- Modigliani, A., Goldoni, P., Royer, F., et al. 2010, in *Society of Photo-Optical Instrumentation Engineers (SPIE) Conference Series*, Vol. 7737, Society of Photo-Optical Instrumentation Engineers (SPIE) Conference Series, 28
- Muzzin, A., Labbé, I., Franx, M., et al. 2012, *ApJ*, 761, 142
- Muzzin, A., Marchesini, D., Stefanon, M., et al. 2013a, *ApJS*, 206, 8
- . 2013b, *ApJ*, 777, 18
- Newman, A. B., Belli, S., & Ellis, R. S. 2015, *ApJL*, 813, L7
- Newman, A. B., Ellis, R. S., Treu, T., & Bundy, K. 2010, *ApJL*, 717, L103
- Onodera, M., Arimoto, N., Daddi, E., et al. 2010, *ApJ*, 715, 385
- Onodera, M., Renzini, A., Carollo, M., et al. 2012, *ApJ*, 755, 26
- Pahre, M. A., Djorgovski, S. G., & de Carvalho, R. R. 1995, *ApJL*, 453, L17
- Peng, C. Y., Ho, L. C., Impey, C. D., & Rix, H.-W. 2010, *AJ*, 139, 2097
- Robertson, B., Cox, T. J., Hernquist, L., et al. 2006, *ApJ*, 641, 21
- Schreiber, C., Pannella, M., Elbaz, D., et al. 2015, *A&A*, 575, A74
- Sharon, K., Gladders, M. D., Rigby, J. R., et al. 2012, *ApJ*, 746, 161
- Shen, S., Mo, H. J., White, S. D. M., et al. 2003, *MNRAS*, 343, 978
- Smail, I., Swinbank, A. M., Richard, J., et al. 2007, *ApJL*, 654, L33
- Stark, D. P., Auger, M., Belokurov, V., et al. 2013, *MNRAS*, 436, 1040
- Straatman, C. M. S., Labbé, I., Spitler, L. R., et al. 2014, *ApJL*, 783, L14
- Szomoru, D., Franx, M., & van Dokkum, P. G. 2012, *ApJ*, 749, 121
- Toft, S., Gallazzi, A., Zirm, A., et al. 2012, *ApJ*, 754, 3
- Treu, T., Stiavelli, M., Bertin, G., Casertano, S., & Møller, P. 2001, *MNRAS*, 326, 237
- Treu, T., Stiavelli, M., Casertano, S., Møller, P., & Bertin, G. 1999, *MNRAS*, 308, 1037
- Trujillo, I., Förster Schreiber, N. M., Rudnick, G., et al. 2006, *ApJ*, 650, 18
- van de Sande, J., Kriek, M., Franx, M., Bezanson, R., & van Dokkum, P. G. 2014, *ApJL*, 793, L31
- . 2015, *ApJ*, 799, 125
- van de Sande, J., Kriek, M., Franx, M., et al. 2011, *ApJL*, 736, L9
- . 2013, *ApJ*, 771, 85
- van der Wel, A., Franx, M., van Dokkum, P. G., et al. 2005, *ApJ*, 631, 145
- van der Wel, A., van de Ven, G., Maseda, M., et al. 2013, *ApJL*, 777, L17
- van Dokkum, P. G., & Franx, M. 1996, *MNRAS*, 281, 985
- van Dokkum, P. G., Franx, M., Kelson, D. D., & Illingworth, G. D. 1998, *ApJL*, 504, L17
- van Dokkum, P. G., Kriek, M., & Franx, M. 2009, *Nature*, 460, 717
- van Dokkum, P. G., Förster Schreiber, N. M., Franx, M., et al. 2003, *ApJL*, 587, L83
- van Dokkum, P. G., Quadri, R., Marchesini, D., et al. 2006, *ApJL*, 638, L59
- van Dokkum, P. G., Franx, M., Kriek, M., et al. 2008, *ApJL*, 677, L5

REFERENCES

- van Dokkum, P. G., Whitaker, K. E., Brammer, G., et al. 2010, *ApJ*, 709, 1018
Vernet, J., Dekker, H., D'Odorico, S., et al. 2011, *A&A*, 536, A105
Vieira, J. D., Marrone, D. P., Chapman, S. C., et al. 2013, *Nature*, 495, 344
Whitaker, K. E., Labbé, I., van Dokkum, P. G., et al. 2011, *ApJ*, 735, 86
White, S. D. M., & Rees, M. J. 1978, *MNRAS*, 183, 341
Williams, R. J., Quadri, R. F., Franx, M., van Dokkum, P., & Labbé, I. 2009, *ApJ*, 691, 1879
Worthey, G., & Ottaviani, D. L. 1997, *ApJS*, 111, 377
Wuyts, S., van Dokkum, P. G., Kelson, D. D., Franx, M., & Illingworth, G. D. 2004, *ApJ*, 605, 677
Zirm, A. W., van der Wel, A., Franx, M., et al. 2007, *ApJ*, 656, 66

NEDERLANDSE SAMENVATTING

De vraag hoe sterrenstelsels groeien en evolueren houdt astronomen sinds de laatste honderd jaar bezig, nadat was ontdekt dat de nevels die aan de sterrenhemel werden waargenomen niet deel uitmaakten van onze Melkweg, maar sterrenstelsels op zichzelf zijn. Dit, in combinatie met Edwin Hubble's observatie dat het Heelal niet statisch en eindig is, maar groeit en uitdijt, zijn de belangrijkste uitgangspunten voor de studie van de evolutie van sterrenstelsels. Door dit te bestuderen, onderzoeken we in feite de evolutie van het Heelal zelf.

Een paar honderdduizend jaar na de Oerknal werd de kosmische achtergrondstraling uitgezonden die informatie bevat over de dichtheid van het vroege Heelal. Op dit punt was het Heelal erg homogeen, met variaties in de dichtheid van de orde van grootte van 10^{-4} . Echter, als we het heelal 14 miljard jaar na dit punt waarnemen, zien we niet dat het gas en de sterren uniform verdeeld zijn. In plaats daarvan klonteren ze samen in groepen van sterren met gas en stof, met grote leegtes zonder sterren tussen hen in. Een vergelijking van de algemene eigenschappen van deze 'groepen' laat zien dat er grote verschillen zijn. Sterrenstelsels kunnen massa's hebben van verschillende ordes van grootte, en dit geldt ook voor de hoeveelheid gas en de ster formatie die plaatsvindt. Daarnaast varieert de structuur van spiraalstelsels tot elliptische stelsels in de vorm van een rugbybal (Figuur 5.12). Deze diversiteit impliceert dat de evolutie van verschillende sterrenstelsels anders is verlopen.

Omdat de snelheid van het licht in vacuum constant is, functioneert de telescoop in sterrenkunde als een soort van tijdmachine. Hoe verder weg je kijkt, hoe verder terug je in de tijd gaat. Door sterrenstelsels waar te nemen die miljarden lichtjaren van ons verwijderd zijn, kunnen astronomen sterrenstelsels observeren in verschillende fases van hun ontwikkeling, om zo de evolutie vast te stellen. De grootste uitdaging is echter om nauwkeurig de juiste voorouder van een nabijgelegen sterrenstelsel te bepalen. Er is op dit moment geen overeenstemming wat de beste methode is om dit te doen, maar er zijn verschillende technieken. Een manier is om sterrenstelsels te rangschikken op basis van massa, van zwaarste tot lichtste stelsel, en aan te nemen dat deze indeling niet verandert over tijd. Er zijn problemen met deze aanname: sterrenstelsels groeien voornamelijk via twee wegen, namelijk door sterren te vormen van reservoirs van gas en stof, of door

het kannibaliseren van hun burens tijdens botsingen. Afhankelijk van de spreiding van de geschiedenis van de ster formatie kunnen beide groeimechanismen de rangschikking veranderen.

Een manier om rekening te houden met de spreiding in de groeigeschiedenis van deze effecten is om simulaties van donkere materie te gebruiken. De halo's bestaande uit donkere materie kunnen worden gematcht aan de waargenomen sterrenstelsels om zo de halo botsingsstambomen om te zetten in zulke stambomen voor sterrenstelsels. Deze methode staat bekend als 'abundance matching', en kan gebruikt worden om de verandering van het aantal sterrenstelsels van een specifieke massa te bepalen. Gebruikmakend van aantal sterrenstelsels dat is waargenomen per massa kan dit worden omgezet naar de voorgaande massa's van een populatie van sterrenstelsels, welke op hun beurt kunnen worden gebruikt om voorouders te selecteren. Simulaties hebben laten zien dat deze methode in staat is om nauwkeurig de evolutie van massa te achterhalen. We gebruiken deze methode om de voorgangers van nabijgelegen sterrenstelsels te vinden, en hun toekomstige evolutie te bepalen. Op deze manier zijn we in staat om te achterhalen wanneer en waar massa is toegevoegd aan een sterrenstelsel.

Caption Figuur 5.12: Een voorbeeld van twee meestvoorkomende morfologische sterrenstelseltypes: een vroeg-type elliptisch stelsel (links) en een laat-type spiraal stelsel (rechts).

Deze thesis

Deze thesis gebruikt de waardevolle datasets van de UltraVISTA and 3DHST projecten, alsmede spectroscopie van de Very Large Telescope (VLT) in Chili, en combineert waarnemingen vanaf zowel de aarde als vanuit de ruimte om massavereniging te meten.

In Hoofdstuk 2 gebruiken we de eerdergenoemde abundance matching techniek om voorgangers tot een paar miljard jaar na de Oerknal van huidige massieve sterrenstelsels te selecteren. Nadat we de voorgangers geselecteerd hebben, gebruiken we nabij-infrarood (NIR) fotometrie van de UltraVISTA en 3DHST projecten om zogenoemde 'image stacks' (bij elkaar gevoegde beelden van verschillende sterrenstelsels met als doel om de signaal-ruis verhouding te verhogen) te maken van sterrenstelsels op verschillende roodverschuivingen. Van deze image stacks maakten we massa oppervlakedichtheid profielen welke laten zien waar en wanneer massieve sterrenstelsels hun massa opbouwen. Zoals eerdere studies demonstreerden wij dat de meeste groei in de massa in de buitenste regio's van een stelsel gebeuren, maar we vonden ook een significante massagroei in de centrale gebieden voor $z < 2$ wat steeds signifikanter wordt voor hogere roodverschuivingen voor $z > 2$. Onze resultaten zijn consistent met het idee dat massieve sterrenstelsels als ster-vormende schijfvormige stelsels begonnen, en die massa vergaarden via ster-formatie overall in de schijf voordat het stelsel zijn ster-formatie stopte en groeide door botsingen met kleinere satellietstelsels waardoor het een elliptische vorm kreeg.

In Hoofdstuk 3 traceren we de sterrenmassa evolutie van sterrenstelsels met een verscheidenheid aan voorgangersmassa's om de tijdschaal van wanneer een ster-

renstelsel zijn massa verkrijgt te vergelijken met de leeftijd van de sterren in zulke stelsels. Daarnaast laten we zien hoe deze tijdschalen zich vergelijken met simulaties. We gebruikten dezelfde abundance matching techniek als in Hoofdstuk 2 om de massa evolutiegeschiedenis te achterhalen. Uit deze geschiedenissen definiëren we massa-vergaringstijd als de tijd wanneer de helft van de sterrenmassa is verkregen en vinden dat massieve sterrenstelsels hun massa eerder vergaren dan lichtere sterrenstelsels, en dat deze relatie monotoon is. We vergelijke ook deze massa-vergaringstijden met resultaten van semi-analytische modellen en van de EAGLE hydrodynamische simulatie. We laten zien dat de massa-vergaringstijdschalen voor lichtere sterrenstelsels niet overeenkomen met simulaties, omdat simulaties een veel eerdere massa-vergaringstijd voorspellen dan dat wordt waargenomen.

In Hoofdstuk 4 gebruiken we morfologische catalogi die zijn verkregen met de Hubble Space Telescope om de asratio (bijvoorbeeld afvlakking) van sterrenstelsels als een functie van roodverschuiving, ster-formatie snelheid, massa, grootte en de sersic index te bepalen. We vonden dat voor niet-actieve sterrenstelsels de sersic index de beste voorspeller van de afvlakking van een stelsel is, waarbij een lagere sersic index overeenkomt met een hogere afvlakking. We veronderstellen dat dit aannemelijk is omdat het de verhouding tussen de bulge en de totale massa reflecteert. Daarentegen was de afwijking van de massa-grootte relatie de beste voorspeller van afvlakking voor ster-vormende sterrenstelsels. Deze stelsels liggen onder de massa-grootte relatie en zijn rond de stelsels die erboven liggen. Voor massieve stelsels vinden we dat voor $z > 2$ de asratio van ster-vormende en inactieve stelsels identiek is wat suggereert dat hun morfologie hetzelfde is.

In Hoofdstuk 5 gebruikten we nabij-infrarood spectroscopie om de snelheidsdispersie van sterren in een sterk uitvergroot (lensed) inactief sterrenstelsel op significante roodverschuiving ($z = 2.71$) te meten. Door het meten van de snelheidsdispersie kunnen we natuurkunde gebruiken om de massa van dit object zeer nauwkeurig te bepalen, zonder aannamen te hoeven doen over de verhouding tussen de massa en het licht. Dit sterrenstelsels was extreem uitvergroot, door een massief object tussen ons en het stelsel (dit effect word lensing genoemd), en uitgespreid over vier beelden, wat het voor ons mogelijk maakte om precieze lensmodellen te ontwikkelen. Het ontbreken van emissielijnen in het optische spectrum bevestigt dat dit sterrenstelsel niet actief sterren aan het vormen is, and dat sterrenstelsels van gemiddelde massa vroeg kunnen stoppen met het vormen van sterren. Onze uit spectroscopie verkregen roodverschuiving is hoger dan wat voorheen werd verwacht van fotometrische gegevens, wat laat zien dat spectroscopie belangrijk is bij het nauwkeurig meten van de roodverschuiving van sterrenstelsels.

PUBLICATIONS

1. *A Stellar Velocity Dispersion for a Strongly-Lensed, Intermediate-Mass Quiescent Galaxy at $z = 2.8$*
A. R. Hill, A. Muzzin, M. Franx, and J. van de Sande
2016, ApJ, 819, 74.
2. *The Mass, Color, and Structural Evolution of Today's Massive Galaxies Since $z \sim 5$*
A. R. Hill, A. Muzzin, M. Franx, B. Clauwens, C. Schreiber, D. Marchesini, M. Stefanon, I. Labbe, G. Brammer, K. Caputi, J. Fynbo, B. Milvang-Jensen, R. E. Skelton, P. van Dokkum, and K. E. Whitaker
2017, ApJ, 837, 147.
3. *The Mass Growth and Stellar Ages of Galaxies: Observations versus Simulations*
A. R. Hill, A. Muzzin, M. Franx, and Danilo Marchesini
2017, ApJL, 849, L26.
4. *The Evolution of Galaxy Flattening at $z < 4$ in CANDELS*
A. R. Hill, A. Muzzin, M. Franx, et al.
In preparation
5. *Characterizing Quasars in the Mid-Infrared: High Signal-to-Noise Ratio Spectral Templates*
A. R. Hill, S. C. Gallagher, R. P. Deo, E. Peeters, and G. T. Richards
2014, MNRAS, 438, 2317.
6. *The Average Structural Evolution of Massive Galaxies Can Be Reliably Estimated Using Cumulative Galaxy Number Densities*
B. Clauwens, **A. R. Hill**, M. Franx, and J. Schaye
2017, MNRAS, 469, L58

7. *The Merger History, AGN and Dwarf Galaxies of Hickson Compact Group 59*
I. S. Konstantopoulos, S. C. Gallagher, K. Fedotov, P. R. Durrell, P. Tzanavaris, **A. R. Hill**, A. E. Zabludoff, M. L. Maier, D. M. Elmegreen, J. C. Charlton, K. E. Johnson, W. N. Brandt, L. M. Walker, M. Eracleous, A. Maybath, C. Gronwall, J. English, A. E. Hornschemeier, and J. S. Mulchaey
2012, ApJ, 745, 30.

8. *The Evolution in the Stellar Mass of Brightest Cluster Galaxies Over the Past 10 Billion Years*
S. Bellstedt, C. Lidman, A. Muzzin, M. Franx, S. Guatelli, **A. R. Hill**, H. Hoekstra, N. Kurinsky, I. Labbe, D. Marchesini, Z. C. Marsan, M. Safavi-Naeini, C. Sifon, M. Stefanon, J. van de Sande, P. van Dokkum and C. Weigel
2016, MNRAS, 460, 2862.

Proceedings

1. *High Signal-to-Noise Ratio Mid-Infrared Quasar Spectral Templates.*
A. R. Hill, S. C. Gallagher, R. P. Deo, E. Peeters, and G. T. Richards.
2014, IAU Symposium Proceedings, Volume 304, 315-318.

2. *High S/N Mid-IR Quasar Templates.*
A. R. Hill, S. C. Gallagher, R. P. Deo, and E. Peeters
2012, Torus Workshop, 245-250.

3. *Characterizing Quasars in the Mid-IR.*
A. R. Hill, S. C. Gallagher, and R. P. Deo
2012, Astronomical Society of the Pacific Conference Series, Volume 460, 126-127.

CURRICULUM VITAE

I was born on 28 April, 1989 in Mississauga, Ontario, Canada. I grew up in Georgetown, Ontario, a bedroom community of Toronto, where I attended elementary and high school. I became interested in astronomy at age 11 after a broken arm forced me inside during recess periods and I began reading the books in the library by section, alphabetically, and picked up a book on astronomy which I found fascinating (I sometimes still wonder what my life as a ‘zoology’ student would have been had I chosen reverse-alphabetically).

In 2007, I moved to London, Ontario where I attended the University of Western Ontario as an astrophysics major. During my bachelors degree, I participated in summer research (Undergraduate Student Research Award: USRA) under the supervision of Sarah Gallagher. My first project was looking for black hole signatures in X-rays using data from the Chandra X-ray Observatory, as part of the XSINGS survey. I continued working with Sarah Gallagher over the next two summers characterizing the nuclear activity in compact groups of galaxies. I graduated in 2011, with honours, as well as being awarded the Maude-Holt Kingston Gold Medal in Astronomy for obtaining the highest grade average in my program.

In 2011, I remained in London, Ontario to pursue my Masters degree with Sarah Gallagher. There, I studied the dusty torus surrounding quasars in the mid-IR. I presented my Masters thesis at various international conferences from the United States to Armenia, as well as publishing my results in MNRAS.

After I completed my Masters degree in Astronomy, I was offered a PhD position at the Sterrewacht Leiden in the Netherlands, which I began at the end of 2013. My PhD work focused on the evolution of massive galaxies in the first few billion years after the big bang, under the supervision of Marijn Franx and Adam Muzzin. During my PhD, I was able to observe in La Palma, Canary Islands as well as the Las Campanas Observatory in Chile. I also attended several conferences and international meetings in Australia, Germany, and the Netherlands to present my work.

ACKNOWLEDGEMENTS

It was Carl Sagan who said that astronomy is a humbling and character-building experience, and never has that point been better demonstrated for me than during the PhD process. I have stood on the shoulders of many giants, and here embark on the impossible task of expressing my gratitude to each and every one of them.

I was very fortunate to be surrounded by family members that always inspired me to reach new heights. Mom, Dad; I know it wasn't easy for you to say goodbye to a daughter for months, and even a year at a time. Your support, and unwavering confidence has made the move so much easier on me and I am eternally grateful. My four siblings, Crissa, Tanya, Ryan and Katie, generated a lot of chaos at home, which encouraged a transatlantic escape. Tanya, Ryan, Katie thanks for making the financial sacrifice to come and visit me and bring a little piece of home over here, if only for a little while. Crissa, from changing my diapers, and driving me to basketball practices, to encouraging me to 'reach for the stars', you continue to go above and beyond the call of a sibling. Nan and Bub, you were always a soft place to land whenever I needed to fall and I am so fortunate to have you as grandparents.

I spent 6 years at Western, and was lucky to be part of a department which set me up for my successes at Leiden. Els and Jan thanks for pointing me in the direction of the Sterrewacht. Pauline, thanks for stepping in as my undergraduate thesis advisor during a maternity leave, for stopping by the sterrewacht from time to time, and running like a beast (I can't keep up with you on Strava)! Aycha, Tyler, K-fed and Neven - you were a fantastic research group and office mates. And Sarah, I couldn't have asked for a better mentor.

Here at the Sterrewacht, I was fortunate enough to be part of a world-class research group. Jesse, you took me under your wing early and helped me so much getting started. Thank you! Mattia, I couldn't have asked for a better 'academic big-brother'. I miss our coffee breaks and the advice you'd dispense, and was so honored to be your paranymph and am glad you are happy and prospering in NYC. Adam, you said my imposter-syndrome was incurable, but nevertheless you kept trying! I know you put in a lot of time, and I hope seeing me improve throughout the process has been rewarding, and know that you played a large part. Mauro, Corentin, Michael, Ken and Jorrryt - thanks very much for the journal

clubs! Especially you Mauro. You saved me reading quite a few papers. And to my office-mate Mieke; thank you for all of our talks, and for hearing me out on my questionably intelligent extra-galactic questions (in addition to my sounding-board on Dutch culture) and most of all, for translating my Nederlandse Samenvatting.

The department here at the Sterrewacht has no equal on this planet in terms of fostering the research environment, and all the supporting staff that plays a role. Thanks to all the secretaries, and the entire computer group for keeping things running. And to all the PhD students, past and present who volunteered their time to bring us all those borrels! A big shout out to Heather, Emanuele, David, Mason, Yours truly, Christian, Ann-Sofie, Chris, Nico, Pedro, Santi, Eleonora, Kim, Maria Christina, and Francisca for helping everyone unwind every Friday.

To all the people who I've lunched, and caffiene-brokek with throughout the years - Tiff, Marissa, Jesse, Mattia, Monica, Marco, Chris, Lorrie, Eva, Gaby, Nico, Mason, Ann-Sofie, Eleonora, Aayush, Margot, Leah, Marco, Corentin, Christian, Cameron, Matteo, Irene, Henriette, Nienke, Renske, David... the list goes on; thank you for those sanity breaks! And for those who participated in Dutch lunches with me over the years! Special thanks to Marijke, Jeroen, Margot, Ricardo, and Mieke for your patience!

Allie, Gorana, Marissa, Mark, Mason, Mart, Olga, Rene, Rimoldi, Tiff and Tom - my family away from family - I cannot express how necessary you guys have been to these years being some of the best I've had. From birthdays, trips, weddings, sinterklaases, christmases, passovers, thanksgivings and easters we've done a lot together. Go, Rene, and Mart - ze zeggen dat het onmogelijk is om Nederlands vrienden te maken (vooral buiten de Sterrewacht!) - we sure showed them! Mark and Olga, trying to keep up with you guys physically has added probably a decade to my life; thanks for keeping me running and climbing! Allie and Mason - it was difficult to feel homesick with your north-eastern familiarity - not to mention that Mason kept moving in next door.

Tiff and Marissa - you guys were integral in terms of me prospering here. There were points where I thought I couldn't do it, and might have gone home had it not been for your compassion, taking me under your wing and helping me adjust to life here. I am so grateful to you two.

Emma - our friendship has endured different universities, different disciplines, different cities and different continents. Since we were 7 years old, you have been the constant thread throughout all of it. For some reason, you have always put up with me, and I am confident that no matter what differences life throws at us, we will always call each other friend.

And lastly Alex. Thank you for going on this adventure with me. After only a few months together, you, an avowed atheist, took a leap of faith and decided that we would take this journey together. Being able to see the world with you has been a privilege, and your patience and unwavering support with me during this PhD process is something I am undeserving of. Your drive, enthusiasm and your ability to actualize your goals is inspiring. Every day, you make me want to do better, and be better and I cannot wait to find out what the universe has in store for us. Here's to many more years of adventures.